Correlations mediated by Cooper pairs in single-electron devices

Ranni, Antti

2023

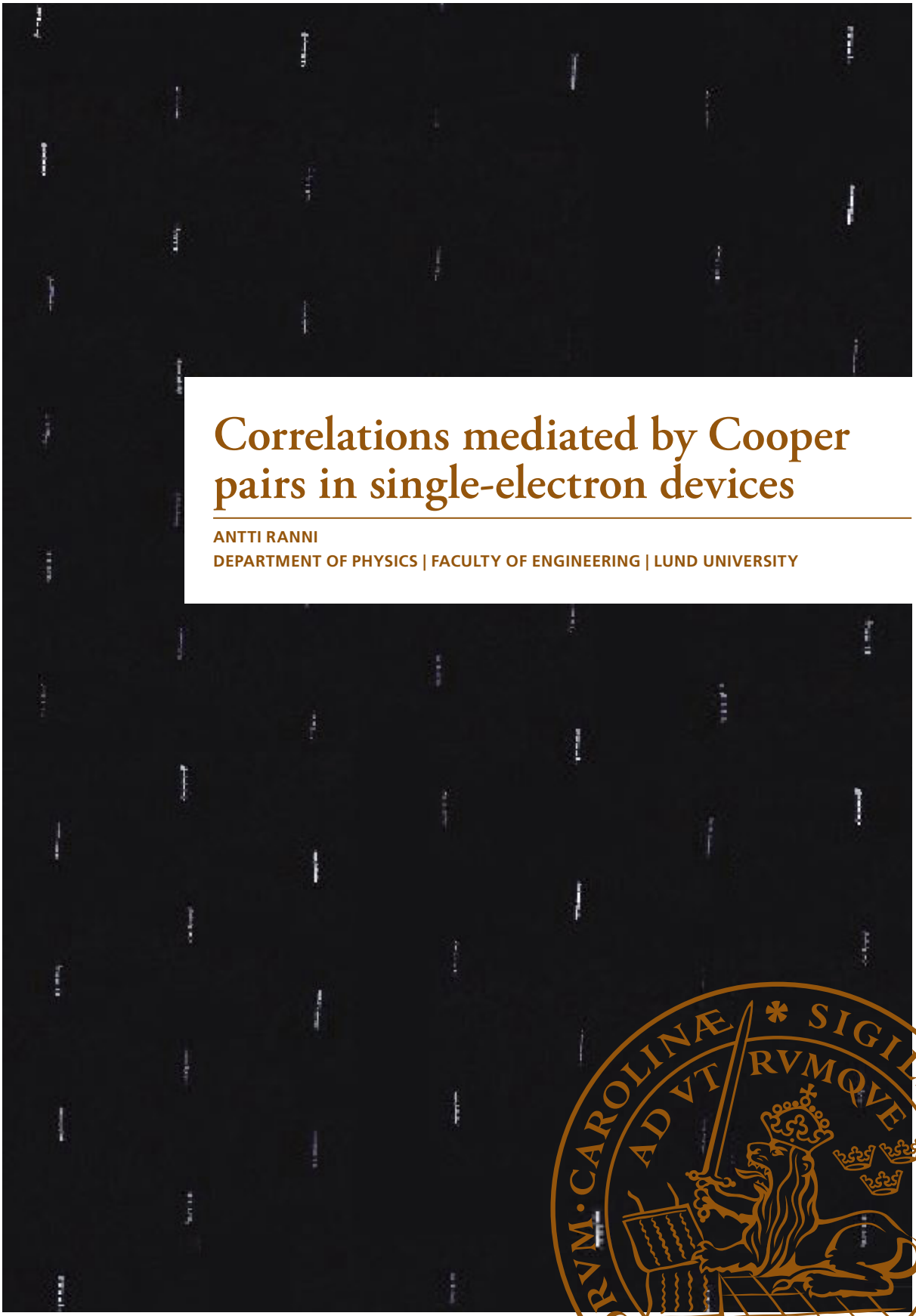

Correlations mediated by Cooper pairs in single-electron devices

ANTTI RANNI
DEPARTMENT OF PHYSICS | FACULTY OF ENGINEERING | LUND UNIVERSITY

Correlations mediated by Cooper pairs in single-electron devices

Correlations mediated by Cooper pairs in single-electron devices

by Antti Ranni

LUND
UNIVERSITY

DOCTORAL THESIS

Thesis advisors:
Associate Professor Ville F. Maisi, Professor Martin Leijnse and Associate Professor Claes Thelander

Faculty opponent:
Associate Professor Szabolcs Csonka
Budapest University of Technology and Economics, Hungary

To be presented, with the permission of the Faculty of Engineering of Lund University, for public criticism in the Rydberg lecture hall at the Department of Physics on Friday, the 8th of December 2023 at 09:15.

Organization
LUND UNIVERSITY

Department of Physics
Box 118
SE–221 00 LUND
Sweden

Document name
DOCTORAL DISSERTATION

Date of disputation
2023-12-08

Sponsoring organization

Author(s)
Antti Ranni

Title and subtitle
Correlations mediated by Cooper pairs in single-electron devices

Abstract
In single-electron devices behaviour of an individual electron results in a measurable effect. Thin potential barriers connecting conductive materials to each other confine electrons into small volumes where Coulomb interactions and quantum confinement significantly affect the energy spectrum. These barriers also give rise to fascinating electron transfer processes as electrons can tunnel through barriers not only sequentially but also two at a time as a Cooper pair if at least one side of a barrier is superconducting.

A Cooper pair splitter is a device harnessing entanglement between particles at separate locations. From a central superconductor a pair of spin-entangled electrons splits and the constituting electrons tunnel into spatially separate arms made out of e.g. normal metal. The splitting process has been experimentally verified but the measured average current signals at the outputs of splitters have constituted of several split pairs and electrons from competing tunneling processes. Paper I provides the first real-time detection of Cooper pair splitting by detecting individual tunneling events with charge counting technique. Cooper pair splitter is versatile device hosting a plethora of electron transfer mechanisms. Paper II focuses on comparing different two-electron tunneling processes against each other.

Strong coupling limit of light-matter interaction has been achieved in multitude of systems including semiconductor double quantum dots addressed with microwaves in recent years. In these systems dipole moment of a double quantum dot couples to the electric field of a resonator giving rise to coherent light-matter interaction. Increasing the impedance of a resonator enhances its coupling to a double quantum dot. Paper III studies high-impedance resonators made out of Josephson junctions. In Paper IV one such resonator is coupled to a double quantum dot embedded in an InAs nanowire achieving the strong coupling limit.

Key words
two-electron tunneling, Cooper pair, charge counting, high-impedance resonator, quantum dot, strong coupling

Classification system and/or index terms (if any)

Supplementary bibliographical information

Language
English

ISSN and key title

ISBN
978-91-8039-871-8 (print)
978-91-8039-870-1 (pdf)

Recipient's notes

Number of pages
123

Price

Security classification

Signature

Date 2023-10-22

Correlations mediated by Cooper pairs in single-electron devices

by Antti Ranni

LUND
UNIVERSITY

Cover illustration front: Charge stability diagram of a double quantum dot obtained by radio-frequency reflectometry. Response shows interdot transition lines.

Cover illustration back: A scan across one interdot transition line. The vertical axis is drive frequency and the horizontal gate voltage.

Faculty of Engineering, Department of Physics
Lund University, Lund, Sweden
ISBN: 978-91-8039-871-8 (print)
ISBN: 978-91-8039-870-1 (pdf)

Printed in Sweden by Media-Tryck, Lund University, Lund 2023

Media-Tryck is a Nordic Swan Ecolabel certified provider of printed material. Read more about our environmental work at www.mediatryck.lu.se

MADE IN SWEDEN

Don't search for all the answers at once.
A path is formed by laying one stone at a time.
— The Giant

Contents

List of publications

This thesis is based on the following publications, referred to by their Roman numerals:

I **Real-time observation of Cooper pair splitting showing strong non-local correlations**
Antti Ranni, Fredrik Brange, Elsa T. Mannila, Christian Flindt, and Ville F. Maisi
Nature Communications, 12, 6358 (2021)

I analyzed the data and wrote the manuscript with input from all co-authors.

II **Local and Nonlocal Two-Electron Tunneling Processes in a Cooper Pair Splitter**
Antti Ranni, Elsa T. Mannila, Axel Eriksson, Dmitry S. Golubev, Jukka P. Pekola, and Ville F. Maisi
Physical Review Letters, 129, 207703 (2022)

I analyzed the data and wrote the manuscript with input from all co-authors. The device is the same as in Paper I.

III **High Impedance Josephson Junction Resonators in the Transmission Line Geometry**
Antti Ranni, Harald Havir, Subhomoy Haldar, and Ville F. Maisi
Applied Physics Letters, 123, 114002 (2023)

I developed the fabrication recipe, fabricated the devices and performed the experiments.

IV **Dephasing in a crystal-phase defined double quantum dot charge qubit strongly coupled to a high-impedance resonator**
Antti Ranni, Subhomoy Haldar, Harald Havir, Sebastian Lehmann, Pasquale Scarlino, Andreas Baumgartner, Christian Schönenberger, Claes Thelander, Kimberly A. Dick, Patrick P. Potts, and Ville F. Maisi
Under revision for npj Quantum Information

I developed the fabrication recipe, fabricated the device from as-grown nanowires, performed the measurements and analyzed the data. I wrote the manuscript with input from all co-authors.

Acknowledgements

I have had a privilege to have Ville as my supervisor. He's truly a master of all crafts. Ville has a great vision what kind of devices to make and always comes up with a multitude of experiments that can be performed with each one of them. As the group is still relatively young and many devices are the first of their kind here, I'm convinced that by adding complexity and combining techniques, even greater experiments will be performed in the future. I thank my co-supervisors Martin and Claes for discussions and many fruitful comments on my results.

When I started to work at FTF several years ago, Waqar had arrived few weeks earlier to do a postdoc in the group. It was a good start for me to learn to use the cleanroom equipment with an experienced fabricator and he is to thank of laying the foundation for resonator devices. As a senior PhD student David B. laid a path for me to follow. The group members who joined later, Harald and Subhomoy, have been indispensable in the resonator project. Harald for modelling couplers and general insight in physics and Subhomoy for his tireless fabrication efforts.

I have had a pleasure to collaborate with several theorists. Fredrik, Christian, Dima, Peter and Patrick extracted simple expressions out of formulas that to me often looked incomprehensible. This not only made fitting an easy procedure but also significantly increased the value of the experimental results. I thank Sebastian for growing nanowires with in-built barriers. I'm especially thankful every time I see a stability diagram for gate-defined quantum dots. Cleanroom and IT staff were highly appreciated for keeping the machines running.

Device meetings provided a platform to gain comments on on-going work as well as to practise talks. I thank Adam, Sven, Markus, Heidi, Rousan, Max, William, Thanos, Ruben and Stephanie for all the discussions during the past years. I have had a pleasure to get to know several PhD students at work and outside including Artis, Asmita, Yue, Pradheebha and Marie. A shoutout to Hossein and Kristi for staying true.

During my five years in the office, I have shared the room with few people. I thank David G., Michael and Simon for creating a calm and open atmosphere. In addition to FTF I found a community at EIT playing floorball and hanging out with Saketh, Karl-Magnus, Anton, Adam and Olli-Pekka.

Populärvetenskaplig sammanfattning

År 1897 uppäckte J. J. Thomson en negativt laddad partikel med tusen gånger mindre massa än vad en väteatom har - denna elementära partikel kallas elektron. Elektroniken avancerade med raska steg från och med början av 1900-talet med många nya komponenter så som transistorer. Transistorer är byggstenar i tillverkning av mikrochip. George Moore påstod år 1965 att antalet transistorer på ett mikrochip fördubblas vartannat år och denna så kallade Moores lag har hållit fram till i dag. Minskandet av storleken på transistorer har gjort detta möjligt. På små skalor, karaktäriserade av nanometer, börjar kvantfysikaliska effekter spela roll, till exempel tunnling. En människa kan inte se mycket tunnare föremål än ett hårstrå, som är hundra tusen gånger större än en nanometer. Tunnling kan beskrivas med följande analogi: Föreställ dig en cyklist en cyklist som vill cykla över en kulle, men har inte tillräckligt med rörelseenergi för att ta sig hela vägen upp. Slutsatsen är att cyklisten inte kan hamna på andra sidan kullen. Denna bild håller inte alltid i partiklarnas värld där en elektron kan dyka upp på andra sidan av en barriär även om elektronen inte har tillräckligt hög energi för att åka över barriären. Det vill säga elektronen tunnlar genom barriären.

Min avhandling undersöker apparater där rörelse av en enskild elektron har en mätbar effekt. I en metall elektrisk ström är ett flöde av elektroner. Resistans är en storhet som karaktäriserar motståndet som ett elektronflöde upplever i en metall. Det är resistansen som gör att strömmen genom metallen ger upphov till värme. Men om vissa metaller, till exempel aluminium, kyls ner nära till närheten av den absoluta nollpunkten -273 °C leder de ström utan resistans. Detta tillstånd kallas supraledande. I en supraledande metall har elektroner bildat par. Låter det inte motsägelsefullt - negativt laddade elektroner repellerar ju varandra? Man kan förstå detta enligt följande resonemang: En metal består av fria elektroner och positivt laddade joner som sitter fast och inte kan röra sig fritt i materialet utan bara vibrerar kring sina jämviktslägen. Däremot kan elektroner röra sig fritt i materialet. Temperatur är en storhet som berättar hur snabbt partiklar rör sig. I låga temperaturer partiklar rör sig långsamt medan de i höga temperaturer rör sig snabbt. När en fri elektron rör sig i en metall attraherar den positiva joner i närheten av sig själv och skapar en ökad densitet av positiv laddning. I höga temperaturer jämnas den här ökade densiteten ut fort på grund av termiska vibrationer, medan den ökade densiteten vid låga temperaturer är tillräckligt långlivad för att attrahera en annan elektron i närheten. På detta sätt kan en elektron med hjälp av joner effektivt sett attrahera en annan elektron.

Elektroner har en inneboende storhet som kallas spinn. Denna fysikaliska storhet kan beskrivas som ett inneboende rörelsemängdsmoment som kan vara antingen $\uparrow$ eller $\downarrow$. Par av elektroner i en supraledare är speciella på ett annat sätt också. Elektronerna av ett par i superledande metal har motsatta spinn men båda elektroner har sitt spinn $\uparrow$ och $\downarrow$ samtidigt. Om man mäter spinnet av en av elektronerna får den andra elektronen omedelbart motsatta spinnet oberoende av avståndet mellan de två elektronerna. Detta kallas kvantsammanflätning. Kvantsammanflätning är till exempel viktig i kvantinformation. I en apparat i mitt arbete, tunnlar elektroner av ett par i supraledande aluminium till separata metallstrukturer. Därmed genererar apparaten kvantsammanflätning mellan separerade elektroner. Splittring av ett sådant par detekterades för första gången i realtid i detta arbete.

Den andra halvan av mitt arbete undersöker ljus-materia interaktion i fasta tillståndet. Ljus består av små energipaket som kallas fotoner. I en apparat jag byggde är fotoner fångade i en struktur som kallas resonator. Resonatorn är en hundra mikrometer lång (tjockleken på ett hårstrå) och en mikrometer bred struktur gjord av superledande material. Du kan föreställa dig att i en sådan struktur är en foton en stående elektromagnetisk våg. Apparaten innehåller också två kvantprickar som är små bitar av halvledarmaterial. Resonatorn är elektriskt kopplad till en av kvantprickorna. När en elektron tunnlar mellan kvantprickorna samverkar den med en foton i resonatorn. Den här samverkan kan användas till exempel att omvandla information från kvantprickarna till en foton.

Chapter 1

Introduction

Tunneling is a purely quantum mechanical phenomenon without any classical counterpart [1]. A particle without enough energy to overcome a potential barrier has a finite probability to permeate the barrier. Tunneling has been explored in multiple systems ranging from artificial constructed nanoscale devices such as single-electron transistors [2] to biological environment [3]. Tunneling provides the basis for many important industrially manufactured technologies such as Esaki diode [4] and scanning tunneling microscopy [5]. In many of the applications single-electron tunneling is the operational principle behind the device functionality and higher-order processes lead to errors [6], e.g. in a single-electron current source. On the other hand, there exists devices where the situation is reversed and the higher-order processes are the desired charge transfer mechanisms whereas the single-electron tunneling is a source of errors [7], e.g. in a Cooper pair splitter.

Hybrid structures of materials with dissimilar charge carriers separated by potential barriers lead to non-trivial transport across the interface. Hence, these structures provide an ideal platform to study tunneling phenomena. An example of such a system is a superconductor tunnel-coupled to a normal-state metal as electrons can tunnel across the junction either one by one (sequential tunneling) or two at the same time. The latter process is known as local Andreev tunneling [8] in which a bound pair of two electrons (Cooper pair) from the superconductor tunnels into the normal-state metal filling two electronic states equidistant above and below the Fermi level. Also the time-reversal of this process in which two electrons tunnel from the normal-state metal into the superconductor is called local Andreev tunneling.

By tunnel-coupling the superconductor to a second normal-state metal structure gives rise to two more two-electron tunneling processes [9]. In the first process two electrons forming a Cooper pair are split into two spatially separate metallic structures. This process and its time-reversal are both known as nonlocal Andreev tunneling. In the second process called elastic cotunneling one electron tunnels directly from one normal-metal structure into the other via a virtual state in the superconductor. This setup is commonly known as a Cooper pair splitter (CPS) and the normal-state metals can be replaced by either ferromagnets [10], semiconductors [11] or carbon nanotubes [12]. The two electrons forming a Cooper pair are spin-entangled in the singlet state [13]. Hence, Cooper pair splitters generate spatially separated entangled spin states by splitting a Cooper pair from a superconductor into two different normal-state structures. Harnessing entangled particles from a superconductor is of fundamental interest to test the foundations of quantum mechanics [14].

Traditionally, splitting of Cooper pairs has been detected indirectly by measuring currents at the outputs of a CPS [10, 15, 16, 11, 17, 12, 18, 19, 20, 21, 22, 23, 24, 25, 26, 27, 28, 29, 30, 31] or their low-frequency cross-correlations [18, 20]. In both of these approaches the measured signals contain contributions from not only Cooper pair splitting but other tunneling processes as well. However, in Paper I for the first time individual Cooper pair splitting events were resolved in time domain by charge counting technique. The paper presents statistics arising from non-local two-electron tunneling in the form of measurements of correlation functions and waiting time distributions. Paper II continues using the same CPS device as Paper I and shows measurements of coupling coefficients for both local Andreev, nonlocal Andreev and elastic cotunneling. Earlier, the experiments focused on studying the energy dependence of the dominant transport mechanism [15, 17, 32, 33, 19, 23, 29]. Comparison between the coupling coefficients of different processes has evaded measurements as distinguishing different charge transfer mechanisms is experimentally difficult. Paper II provides the first comparison between the coefficients enabled by charge counting technique. Comparing the strength of different two-electron processes is not only an intriguing physics question but also important for quantum technologies relying on two-electron transport such as superconducting qubits [34, 35, 36, 37, 38], and CPSs [39, 40, 10, 15, 16, 11, 41, 42]. The coefficients contain information about the geometry and materials involved in transport and help to design structures favouring the targeted process.

Another important technique tapping into single-electron devices is to probe them by radio-frequency measurements. In superconducting coplanar waveguide (CPW) microwave resonators a central superconductor is separated from

a ground plane on both sides by a micrometer scale gap. The resonance frequency depends on the resonator length as well as the inductance and capacitance per unit length. The characteristic impedance of these resonators is set by the two latter quantities. In simplest CPW resonator central conductor is a strip of superconducting metal e.g. aluminium and typically the geometry is designed so that the impedance is $50\,\Omega$ matching the standard value for cicuits the resonators are connected to [43, 44]. These resonators have been used for example as radiation detectors [45, 46, 47] and in quantum information experiments [48, 49, 50].

Strong coupling is an important limit of light-matter interaction where the coupling between the two systems exceeds the losses in the hybrid system [51]. In this limit the two systems coherently exhange energy quanta. Strong coupling has been demonstrated in various quantum optics systems such as alkali atoms [52], Rydberg atoms [53], superconducting qubits [36] and optically probed semiconductor single quantum dots in photoluminescence studies [54, 55]. These systems have attracted interest in the field of quantum information technology as they can be utilized for example, to coherently couple remote qubits [56, 57] and for transferring quantum information from qubits to photons [58, 59].

By increasing the inductance of the central conductor, the impedance increases enhancing the vacuum electric field fluctuations. This can be achieved e.g. by using an array of Josephson junctions with large inductance as the central conductor [60]. Other high-impedance materials for building resonators include arrays of superconducting quantum interference devices (SQUIDs) [61, 60], granular aluminium [62, 63] and NbTiN [64, 65]. The enhanced electric component helps to achieve a strong coupling between microwave photons and semiconductor spin [66, 67, 68, 65] and charge [61] qubits.

Paper III studies two high-impedance resonators made out of Josephson junctions in transmission line geometry. The two resonators are nominally identical apart from their capacitive couplings to input/output lines. The paper shows that in the compact geometries of these resonators, coupling capacitances form a significant portion of the total capacitances. The considerable contribution of the coupling capacitances to the total capacitance is also shown to limit the highest attainable coupling to input/output lines in these devices. After characterization of bare resonator devices in Paper III the next step was to couple a resonator to a semiconducting DQD. Paper IV studies light-matter interaction between a Josephson junction array resonator, which is designed based on the resonators in Paper III, and a DQD formed in a polytype defined InAs nanowire. In this hybrid system the strong coupling limit was reached and it was also shown that in the studied charge qubit coherence was not charge noise limited.

Chapter 2

Cooper pair splitting

In this chapter, two-electron tunneling in a device known as a Cooper pair splitter (CPS) is discussed. Papers I and II use the same CPS device. Section 1 introduces a normal metal - insulator -superconductor junction which is a basic building block of the device. Section 2 (Paper I) focuses on detection of Cooper pair splitting in real time and the correlation statistics arising from this tunneling process. The versatile splitter device also enables measurement of coupling coefficients of three two-electron tunneling processes discussed in Section 3 (Paper II).

1 Normal metal - insulator - superconductor junction

In this section the device used in Papers I and II to study two-electron tunneling processes is theoretically constructed bit by bit. Experiments are introduced later in Sections 2 and 3. Superconductor as a source of paired electrons is an indispensable building block of a system exhibiting two-electron tunneling and thus a natural starting point as Section 1.1. To study tunneling phenomena the superconductor needs to be coupled to a conductive material in a way where the two are separated by a potential barrier. Tunneling is probed across this interface which is known as a tunnel junction. A range of materials suits to be coupled to the superconductor. Here, a normal-state metal is selected since normal metal - insulator - superconductor (NIS) junctions were applied in Papers I and II due to earlier successful charge counting experiments employing NIS junctions [69, 33, 70]. Potential barrier can be made out of e.g. an insulating

oxide layer between the superconductor and the normal-state metal [71].

In order to experimentally detect individual tunneling events, either side of the interface must contains an electron number which is well-defined and experimentally accessible. The normal-state metal is made small and it is tunnel-coupled to the superconductor but isolated galvanically from any other circuitry. Here, such metallic system is referred to as an island. Hence, the electron number on the metallic island is only affected by tunneling across the junction connecting the island to the superconductor. A gate electrode is brought in the near vicinity of the metallic island to form a capacitive coupling between the two. By varying applied voltage to the gate, the electrostatic potential on the island is changed adjusting the energetically preferred electron number on it. A system consisting of a small piece of metal with a tunnel-coupling to a reservoir and a capacitive coupling to a gate electrode is known as a single-electron box (SEB) [72] which was first studied by Lafarge et al. in 1991 [73].

In Section 1.2 the electrostatic energy on a metallic island is derived and this result shows that energetically favourable charge states (electron numbers) can be selected by tuning the gate voltage. This result also shows that a considerable deviation from the energetically lowest-lying charge states is suppressed as adding or subtracting electrons leads to a considerable energy cost. Hence, only a few charge states on the metallic island participate in transport across the junction [74]. This fact is crucial for charge counting which becomes clear in Section 2.

After discussing the key ingredients of NIS, namely a superconductor and charging effects on metallic island, the charge transfer between the two can be addressed. In contrast to sequential tunneling in which a single electron tunnels into or out the metallic island, local Andreev tunneling changes the electron number on a metallic island by two. This mechanism is described in Section 1.3. Tunnel-coupling the superconductor to a second metallic island so that the two junctions are in a close proximity of each other enables non-local tunneling processes to take place. These processes are non-local Andreev tunneling and elastic cotunneling [9] and they are discussed in Section 1.3. Section 2 introduces the CPS device used in Papers I and II and how individual tunneling events are resolved in time domain. Furthermore, Section 2 discusses statistics arising from non-local two-electron tunneling presented in Paper I. Coupling coefficients of the three two-electron tunneling processes, experimentally determined in Paper II, are compared against each other in Section 3.

1.1 Superconducting energy gap

In this section the emergence of the energy gap in the superconducting density of states (DoS) is shown by following the Ref. 75. The superconducting gap sets the relevant energy scale in a superconductor and it is an important parameter later when tunneling involving a superconductor is considered. The DoS is derived in the framework of BCS theory. The superconducting material in Papers I and II is aluminum in which superconductivity is explained by the BCS theory. Second quantization with fermionic creation $\hat{c}^{\dagger}_{\boldsymbol{k},\sigma}$ and annihilation $\hat{c}_{\boldsymbol{k},\sigma}$ operators is applied. The pairing Hamiltonian is given by

$$H_{\text{pairing}} = \sum_{\boldsymbol{k},\sigma} \epsilon_{\boldsymbol{k}} \hat{n}_{\boldsymbol{k},\sigma} + \sum_{\boldsymbol{k},\boldsymbol{l}} V_{\boldsymbol{k},\boldsymbol{l}} \hat{c}^{\dagger}_{\boldsymbol{k},\uparrow} \hat{c}^{\dagger}_{-\boldsymbol{k},\downarrow} \hat{c}_{-\boldsymbol{l},\downarrow} \hat{c}_{\boldsymbol{l},\uparrow}, \tag{2.1}$$

where the first summation stands for the kinetic energy and the second one sets the interaction between electrons of opposite momentum and spin orientation. The first summation is over momentum $\boldsymbol{k}$ and spin $\sigma = \uparrow, \downarrow$. The particle number operator $\hat{n}_{\boldsymbol{k},\sigma} = \hat{c}^{\dagger}_{\boldsymbol{k},\sigma} \hat{c}_{\boldsymbol{k},\sigma}$ yields either 0 and 1 when operated on electronic states due to Pauli exclusion principle. $\epsilon_{\boldsymbol{k}}$ is the kinetic energy of an electron with momentum $\boldsymbol{k}$. The second summation in Equation 2.1 is taken over momenta $\boldsymbol{k}$ and $\boldsymbol{l}$. $V_{\boldsymbol{k},\boldsymbol{l}} = \frac{1}{\Omega} \int V(\boldsymbol{r}) e^{i(\boldsymbol{l}-\boldsymbol{k})\cdot\boldsymbol{r}} d\boldsymbol{r}$ are the matrix elements of the interaction potential, where Ω is the normalization volume and $\boldsymbol{r}$ the distance between electrons.

The goal is to find out the coefficients in Equation (2.1). Operators of the form $\hat{c}_{-\boldsymbol{k},\downarrow} \hat{c}_{\boldsymbol{k},\uparrow}$ in normal state average out to zero in the absence of coherence. The superconducting ground state is a coherent superposition of paired electrons and the expectation value of the product $\hat{c}_{-\boldsymbol{k},\downarrow} \hat{c}_{\boldsymbol{k},\uparrow}$ can be finite. By adding and subtracting the expectation value $x_{\boldsymbol{k}} \equiv \langle \hat{c}_{-\boldsymbol{k},\downarrow} \hat{c}_{\boldsymbol{k},\uparrow} \rangle$, the product can be written as

$$\hat{c}_{-\boldsymbol{k},\downarrow} \hat{c}_{\boldsymbol{k},\uparrow} = x_{\boldsymbol{k}} + (\hat{c}_{-\boldsymbol{k},\downarrow} \hat{c}_{\boldsymbol{k},\uparrow} - x_{\boldsymbol{k}}). \tag{2.2}$$

Adding the term $-\mu \sum_{\boldsymbol{k},\sigma} \hat{n}_{\boldsymbol{k},\sigma}$ to the pairing Hamiltonian allows the particle number to change, μ is the chemical potential. This term can be combined with the kinetic term in Equation (2.1) as $\sum_{\boldsymbol{k},\sigma} \mathcal{E}_{\boldsymbol{k}} \hat{n}_{\boldsymbol{k},\sigma}$, where $\mathcal{E}_{\boldsymbol{k}} \equiv \epsilon_{\boldsymbol{k}} - \mu$ is the single-particle energy.

The term with parentheses around it in Equation (2.2) is a fluctuation around $x_{\boldsymbol{k}}$. This fluctuation can be assumed small in the presence of many particles. In-

serting Equation (2.2) into the pairing Hamiltonian of Equation (2.1), including the chemical potential and dropping terms bilinear in the fluctuation yields

$$\tilde{H}_{\text{pairing}} = \sum_{\boldsymbol{k},\sigma} \mathcal{E}_{\boldsymbol{k}} \hat{n}_{\boldsymbol{k},\sigma} + \sum_{\boldsymbol{k},\boldsymbol{l}} V_{\boldsymbol{k},\boldsymbol{l}} (\hat{c}^{\dagger}_{\boldsymbol{k},\uparrow} \hat{c}^{\dagger}_{-\boldsymbol{k},\downarrow} x_{\boldsymbol{l}} + x^{\dagger}_{\boldsymbol{k}} \hat{c}_{-\boldsymbol{l},\downarrow} \hat{c}_{\boldsymbol{l},\uparrow} - x^{\dagger}_{\boldsymbol{k}} x_{\boldsymbol{l}}). \tag{2.3}$$

By comparing this new Hamiltonian to H_{pairing} one notices that by assuming fluctuations to be small all terms are at most quadratic in creation and annihilation operators in contrast to fourth order earlier. The product of the pairing potential $V_{\boldsymbol{k},\boldsymbol{l}}$ and the expectation value $x_{\boldsymbol{k}}$ can be written as $\Delta_{\boldsymbol{k}} \equiv -\sum_{\boldsymbol{l}} V_{\boldsymbol{k},\boldsymbol{l}} x_{\boldsymbol{l}}$. Rewriting the Hamiltonian, this time the one given by Equation (2.3), gives

$$\tilde{H}_{\text{pairing}} = \sum_{\boldsymbol{k},\sigma} \mathcal{E}_{\boldsymbol{k}} \hat{n}_{\boldsymbol{k},\sigma} - \sum_{\boldsymbol{k}} (\Delta_{\boldsymbol{k}} \hat{c}^{\dagger}_{\boldsymbol{k},\uparrow} \hat{c}^{\dagger}_{-\boldsymbol{k},\downarrow} + \Delta^{\dagger}_{\boldsymbol{k}} \hat{c}_{-\boldsymbol{k},\downarrow} \hat{c}_{\boldsymbol{k},\uparrow} - \Delta_{\boldsymbol{k}} x^{\dagger}_{\boldsymbol{k}}). \tag{2.4}$$

Equation (2.4) is a sum of single-particle energies and energies of pairs of two electrons as in the second sum products of operators with opposite momentum and spin are multiplied by $\Delta_{\boldsymbol{k}}$ which is a characteristic energy of paired electrons. Hamiltonian quadratic in creation and annihilation operators can be diagonalized by Bogoliubov-Valatin transformation [76, 77]

$$\begin{pmatrix} \hat{c}_{-\boldsymbol{k},\downarrow} \\ \hat{c}^{\dagger}_{\boldsymbol{k},\uparrow} \end{pmatrix} = \begin{pmatrix} u^{*}_{\boldsymbol{k}} & -v_{\boldsymbol{k}} \\ v^{*}_{\boldsymbol{k}} & u_{\boldsymbol{k}} \end{pmatrix} \begin{pmatrix} \hat{\gamma}_{-\boldsymbol{k},\downarrow} \\ \hat{\gamma}^{\dagger}_{\boldsymbol{k},\uparrow} \end{pmatrix} \tag{2.5}$$

where $\hat{\gamma}^{\dagger}_{\boldsymbol{k},\uparrow}$ is a fermionic quasiparticle excitation creation operator. The complex coefficients satisfy $|u_{\boldsymbol{k}}|^2 + |v_{\boldsymbol{k}}|^2 = 1$ as the transformation is canonical. By inserting the quasiparticle operators of Equation (2.5) into the Hamiltonian in Equation (2.4) the following expression is obtained

$$\begin{aligned} \tilde{H}_{\text{pairing}} = &\sum_{\boldsymbol{k}} \mathcal{E}_{\boldsymbol{k}} ((|u_{\boldsymbol{k}}|^2 - |v_{\boldsymbol{k}}|^2)(\hat{\gamma}^{\dagger}_{\boldsymbol{k},\uparrow} \hat{\gamma}_{\boldsymbol{k},\uparrow} + \hat{\gamma}^{\dagger}_{-\boldsymbol{k},\downarrow} \hat{\gamma}_{-\boldsymbol{k},\downarrow}) + 2|v_{\boldsymbol{k}}|^2 + 2u^{*}_{\boldsymbol{k}} v^{*}_{\boldsymbol{k}} \hat{\gamma}_{-\boldsymbol{k},\downarrow} \hat{\gamma}_{\boldsymbol{k},\uparrow} \\ &+ 2u_{\boldsymbol{k}} v_{\boldsymbol{k}} \hat{\gamma}^{\dagger}_{\boldsymbol{k},\uparrow} \hat{\gamma}^{\dagger}_{-\boldsymbol{k},\downarrow}) + \sum_{\boldsymbol{k}} ((\Delta_{\boldsymbol{k}} u_{\boldsymbol{k}} v^{*}_{\boldsymbol{k}} + \Delta^{*}_{\boldsymbol{k}} u^{*}_{\boldsymbol{k}} v_{\boldsymbol{k}})(\hat{\gamma}^{\dagger}_{\boldsymbol{k},\uparrow} \hat{\gamma}_{\boldsymbol{k},\uparrow} + \hat{\gamma}^{\dagger}_{-\boldsymbol{k},\downarrow} \hat{\gamma}_{-\boldsymbol{k},\downarrow} - 1) \\ &+ (\Delta_{\boldsymbol{k}} v^{*2}_{\boldsymbol{k}} - \Delta^{*}_{\boldsymbol{k}} u^{*2}_{\boldsymbol{k}}) \hat{\gamma}_{-\boldsymbol{k},\downarrow} \hat{\gamma}_{\boldsymbol{k},\uparrow} + (\Delta^{*}_{\boldsymbol{k}} v^{2}_{\boldsymbol{k}} - \Delta_{\boldsymbol{k}} u^{2}_{\boldsymbol{k}}) \hat{\gamma}^{\dagger}_{\boldsymbol{k},\uparrow} \hat{\gamma}^{\dagger}_{-\boldsymbol{k},\downarrow} + \Delta_{\boldsymbol{k}} x^{\dagger}_{\boldsymbol{k}}). \end{aligned} \tag{2.6}$$

By setting $2\mathcal{E}_{\boldsymbol{k}}u_{\boldsymbol{k}}v_{\boldsymbol{k}} + \Delta^*_{\boldsymbol{k}}v^2_{\boldsymbol{k}} - \Delta_{\boldsymbol{k}}u^2_{\boldsymbol{k}} = 0$ the terms proportional to $\hat{\gamma}^\dagger_{\boldsymbol{k},\uparrow}\hat{\gamma}^\dagger_{-\boldsymbol{k},\downarrow}$ or $\hat{\gamma}_{-\boldsymbol{k},\downarrow}\hat{\gamma}_{\boldsymbol{k},\uparrow}$ vanish leaving only a constant and terms proportional to number operator $\gamma^\dagger_{\boldsymbol{k},\sigma}\gamma_{\boldsymbol{k},\sigma}$. The diagonalized Hamiltonian reads as

$$H_{\mathrm{diag}} = \sum_{\boldsymbol{k}}(\mathcal{E}_{\boldsymbol{k}} - E_{\boldsymbol{k}} + \Delta_{\boldsymbol{k}}x^*_{\boldsymbol{k}}) + \sum_{\boldsymbol{k},\sigma} E_{\boldsymbol{k}}\hat{\gamma}^\dagger_{\boldsymbol{k},\sigma}\hat{\gamma}_{\boldsymbol{k},\sigma}, \tag{2.7}$$

where $E_{\boldsymbol{k}} \equiv \sqrt{\mathcal{E}^2_{\boldsymbol{k}} + |\Delta_{\boldsymbol{k}}|^2}$ is the quasiparticle energy. For such an excitation the minimal required energy is $|\Delta_{\boldsymbol{k}}|$ which is the superconducting gap. To derive the density of states the gap is assumed to be independent of $\boldsymbol{k}$ as $\boldsymbol{k}$ values are close the Fermi wavevector.

The excitations in superconductor correspond to electrons in normal state. Hence the relation $N_{\mathrm{S}}(E)dE = N_{\mathrm{N}}(\mathcal{E})d\mathcal{E}$ holds between the superconducting $N_{\mathrm{S}}(E)$ and $N_{\mathrm{N}}(\mathcal{E})$ normal-state DoS. Electronic temperatures in this thesis remain below 200 mK. The superconducting material used throughout this thesis is aluminium with superconducting gap of $\Delta = 200\,\mu$eV [78] corresponding to the temperature of 2.3 K. Thus the energy range around the Fermi level is small and for the purposes of this thesis the normal-state DoS is constant, e.g. $N_{\mathrm{N}}(\mathcal{E}) = N_{\mathrm{N}}(0)$ if the Fermi level is given the value zero. The superconducting DoS normalized by the normal-state DoS is

$$n_{\mathrm{SC}}(E) = \frac{N_{\mathrm{S}}(E)}{N_{\mathrm{N}}(0)} = \frac{d\mathcal{E}}{dE} = \begin{cases} \frac{|E|}{\sqrt{E^2-\Delta^2}} & , |E| > \Delta \\ 0 & , |E| < \Delta \end{cases}. \tag{2.8}$$

1.2 Charging of a small metallic island

Charging an isolated system by a known number of excess elementary charges was first carried out by R. A. Millikan in 1911 in Millikan's oil drop experiment [79]. Here, charging effects on a small metallic island are considered and electrostatic energy of a metallic island is derived. The following discussion is inspired by Ref. [80]. Starting point is an island completely isolated from the environment. The total charge on the island is zero $Q_{\mathrm{island}} = 0$. By bringing a gate electrode in the near vicinity of the island, a capacitive coupling C_{G} is introduced between the island and the electrode. As voltage V_{G} is applied to the electrode the island is polarized. Positive gate voltage draws mobile electrons on the island to the edge close the electrode creating a local negative net electric

charge and a local positive charge on the opposite edge as the lattice ions stay put.

The process of varying the gate voltage so far only affects the charge distribution on the island and does not alter the total charge as electrons have nowhere to go. Tunnel-coupling the island to a grounded conducting electrode allows the electron number on the island to fluctuate as electrons now can tunnel into or out of the island via the tunnel junction. This grounded electrode acts as an electron reservoir and either emits an electron to the island or absorbs from it. Let n be the excess electron number on the island with the neutral state $Q_{\text{island}} = 0$ as reference. Schematics for this configuration is shown in Fig. 2.1.

Charge $Q_{\text{island}} = -en$ on the island is quantized, e is the elementary charge. In addition to resistance the tunnel junction has capacitance C_{J}. The island can now be considered as a volume containing one plate of each capacitor (gate and junction). The charges on the capacitor plates are $\pm Q_{\text{J}}$ and $\pm Q_{\text{G}}$. Naturally $Q_{\text{island}} = Q_{\text{J}} - Q_{\text{G}}$. Kirchhoff's voltage law gives $V_{\text{G}} - Q_{\text{G}}/C_{\text{G}} - Q_{\text{J}}/C_{\text{J}} = 0$ where the two latter terms on the left hand side are the voltage drops over the capacitors. The two conditions for the charge and the voltage form the basis for electrostatics

$$\begin{cases} Q_{\text{island}} - Q_{\text{J}} + Q_{\text{G}} = 0 \\ V_{\text{G}} - Q_{\text{G}}/C_{\text{G}} - Q_{\text{J}}/C_{\text{J}} = 0 \end{cases} \tag{2.9}$$

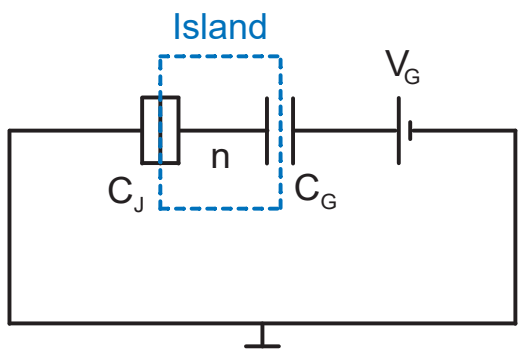

Figure 2.1: Single-electron box circuit diagram. Metallic island is the area enclosed by the blue dashed line containing the charge $-en$. The island is coupled to a gate electrode by the capacitance C_{G} and the electrode is connected to voltage V_{G}. Grounded electrode acts as an electron reservoir which emits electrons to the island or absorbs from it through the tunnel junction which has the capacitance C_{J}.

The total energy stored in the circuit is given by the capacitor energies subtracted by the work provided by the gate voltage,

$$E_{\text{stored}} = \frac{Q_{\text{J}}^2}{2C_{\text{J}}} + \frac{Q_{\text{G}}^2}{2C_{\text{G}}} - V_{\text{G}}Q_{\text{G}}. \tag{2.10}$$

By writing this energy as a function of the excess electron number n one can see the effect of adding or removing electrons from the island. For this purpose, the capacitor charges Q_{J} and Q_{G} in Equation (2.9) need to be written with the help of n. To make the expressions more compact, the capacitances can be grouped as $C_\Sigma \equiv C_{\text{J}} + C_{\text{G}}$ which is the capacitance between the island and its environment. Hence, the charges read as

$$\begin{cases} Q_{\text{J}} = \frac{C_{\text{J}}}{C_\Sigma}\left(C_{\text{G}}V_{\text{G}} - en\right) \\ Q_{\text{G}} = \frac{C_{\text{G}}}{C_\Sigma}\left(C_{\text{J}}V_{\text{G}} + en\right) \end{cases} \tag{2.11}$$

By plugging in the charges from Equation (2.11) to the energy in Equation (2.10),

$$E_{\text{stored}} = \frac{1}{2C_\Sigma}\left(e^2n^2 - 2C_{\text{G}}V_{\text{G}}en - C_{\text{J}}C_{\text{G}}V_{\text{G}}^2\right). \tag{2.12}$$

The energy stored in the circuit is now constructed as a function of n and V_{G} which is an experimentally tunable parameter. $n_{\text{G}} \equiv C_{\text{G}}V_{\text{G}}/e$ is a dimensionless parameter and known as the normalized gate-offset charge. It is a convenient parameter for describing the effect of the gate voltage to the electronic population on the island. By adding $e^2n_{\text{G}}^2/2C_\Sigma$ to and subtracting it from the right hand side of Equation (2.12) yields

$$E_{\text{stored}} = \frac{e^2}{2C_\Sigma}\left((n - n_{\text{G}})^2 - \frac{C_\Sigma}{C_{\text{G}}}n_{\text{G}}^2\right). \tag{2.13}$$

Energetics of electrons tunneling into and out of the island only depend on terms containing n in Equation 2.13. Hence, this energetics is described by

$$E_{\text{island}}(n) = E_{\text{C}}(n - n_{\text{G}})^2, \tag{2.14}$$

where $E_{\text{C}} \equiv e^2/2C_\Sigma$ is commonly known as the charging energy and describes the energy scale of adding one electron to or removing it from the island. Now one is well-prepared to study the energy changes of tunneling. The energy cost

of either adding an electron to (in) or subtracting an electron from (out) an island is given by

$$\delta E_{1e}^{\text{in/out}} = E_{\text{island}}(n) - E_{\text{island}}(n \pm 1) = \mp 2E_C \left(n \pm \frac{1}{2} - n_G \right). \tag{2.15}$$

For the terms with two sign choices, the upper sign is for 'in'. If instead two electrons are either added to or subtracted from an island the cost becomes

$$\delta E_{2e}^{\text{in/out}} = E_{\text{island}}(n) - E_{\text{island}}(n \pm 2) = \mp 4E_C \left(n \pm 1 - n_G \right). \tag{2.16}$$

1.3 Tunneling across normal metal - insulator - superconductor junction

In Figs. 2.2 (a) and (b) local tunneling processes across a NIS junction are displayed. The density of states in a superconductor is given by Equation (2.8) which contains an energy gap of the width 2Δ which is located symmetrically around the Fermi level E_F. Panel (a) shows a sequential tunneling event in which a single electron tunnels from normal metal to superconductor. The superconducting gap is free of single-particle states and therefore sequential tunneling requires energies at least Δ above the Fermi level. The Fermi function f gives the electronic occupation probability and reads at a finite temperature T as $f(T) = (1 + \exp((E - E_F)/k_B T))^{-1}$, where k_B is the Boltzmann constant. The tail of the Fermi function can be approximated by an exponential $\exp(-(E - E_F)/k_B T)$ when $E - E_F \gg k_B T$. At the superconducting gap edge $E - E_F = \Delta$ which for aluminium is $200\,\mu$eV [78]. The electronic base temperature of a dilution refrigerator used in the experiments done in all papers of this thesis is 50 mK [81] which corresponds to a thermal energy of $4\,\mu$eV. Thus our assumption $E - E_F \gg k_B T$ is sound. The sequential tunneling processes across the NIS junction are exponentially suppressed by the superconducting gap and decreasing temperature [82].

Unlike sequential tunneling the local Andreev tunneling in panel (b) takes place at subgap energies. In this phenomenon first discovered by A. F. Andreev in 1964 [8] an electron with the energy between E_F and $E_F + \Delta$ incident to the interface from the normal-state metal can propagate into superconductor as an evanescent wave and eventually condensate as a part of a Cooper pair to the superconducting ground state at the Fermi level [75]. The span inside which the wave decays is given by the superconducting coherence length. The condens-

ation demands another electron which is found in the normal-state metal an equidistant energy below the Fermi level as the incident electron was above [83]. This second electron has an opposite spin compared to the first one as Cooper pairs consist of electrons with opposite spins. Thus a charge $-2e$ is transmitted through the interface.

Local Andreev requires both spin types to be present in the material contacted to superconductor [84] which is fulfilled for materials with spin-rotation symmetry such as a normal-state metal [85]. If the normal-state metal was replaced with e.g. spin-polarized ferromagnet the local Andreev tunneling would become forbidden [86, 87]. The time-reversal of this process where a Cooper pair from the superconductor tunnels into one metallic contact is also called local Andreev tunneling.

The local tunneling processes described above occur across a single NIS junction. Cooper pair has a finite size characterized by the superconducting coherence length. By introducing a second NIS junction to the system so that the separation of the two junctions is comparable to the superconducting coherence length enables an incident electron from one metallic contact to pair with an electron from the same contact as earlier or even in the other metallic contact [88]. The latter non-local tunneling process is shown in panel (c) where two electrons from different spatially separated metallic contacts tunnel into the central superconductor virtually simultaneously forming a Cooper pair. In the time-reversal version a Cooper pair inside the central superconductor splits as the two electrons constituting it tunnel into separate normal metal contacts. These two processes are known as non-local Andreev tunneling.

Another non-local two-electron tunneling process known as an elastic cotunneling is shown in panel (d) where an electron from the left metallic contact tunnels directly into the right one via an intermediate virtual state. Unlike in sequential tunneling the electron now can have its energy inside the gap. The first description of elastic cotunneling was given by D. V. Averin and Yu. V. Nazarov in 1990 [89]. Elastic cotunneling can be conceptually understood by the time-energy uncertainty relation $\Delta t \Delta E \geq \hbar/2$ [90]. According to this inequality an electron from a metallic contact can tunnel to a higher energy virtual state in the superconductor as long as the time spent at this state is short enough.

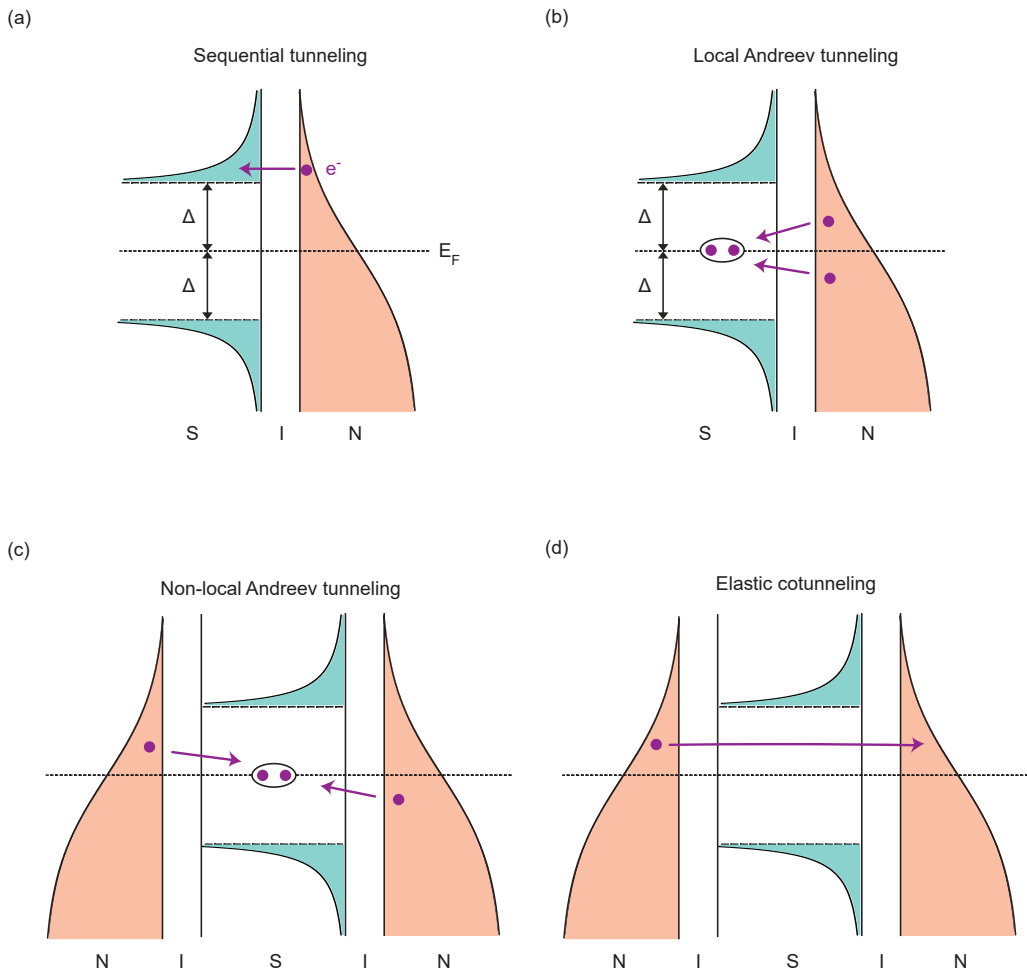

Figure 2.2: One and two-electron tunneling in NISIN structure. Schematics of local (a)-(b) and non-local (c)-(d) tunneling processes by graphs where the vertical direction denotes the energy. Δ is the superconducting gap and E_{F} the Fermi level. (a), A sequential tunneling event where an electron in the normal-state metal tunnels out of the metallic contact to the superconductor. (b), Two electrons from the normal-state metal tunnel into the superconductor forming a Cooper pair. (c), An electron from the left metallic contact pairs with another electron from the right metallic contact to form a Cooper pair in the superconductor. (d), An electron tunneling from the left metallic contact directly to the right one via a virtual state in the superconductor. N = normal-state metal, I = insulator and S = superconductor.

The sequential tunneling rate is derived in Paper II (Supplementary information for details) at zero energy cost to be

$$\Gamma_{1e}(\delta E \to 0, T) = \frac{1}{e^2 R_\mathrm{T}} \sqrt{2\pi \Delta k_\mathrm{B} T} \mathrm{e}^{-\Delta/k_\mathrm{B}T}. \tag{2.17}$$

From Equation (2.17) one instantly sees the exponential suppression due to the gap and decreasing temperature. Equation (2.17) assumes $\delta E, k_\mathrm{B}T \ll \Delta$. The charging energy E_C sets the scale for the energy cost δE. In the device in Papers I and II the charging energies of the metallic islands are around $40\,\mu$eV [81]. The tunneling rate of a process of interest is measured by tuning the initial and final charge states of the process close to degeneracy as will be shown in Section 2. Hence δE is smaller than E_C and $\delta E \ll \Delta$ is justified. The thermal energy $k_\mathrm{B}T$ at the highest temperature of 175 mK in Paper II is $15\,\mu$eV and much smaller than Δ. For the charging energy to govern single-electron transport to and from an island the condition $E_\mathrm{C} \gg k_\mathrm{B}T$ must be met [80] which is the case. For the wave function of an excess electron to be localized on island the junction resistance needs to exceed the resistance quantum $R_\mathrm{K} = h/e^2 \approx 25.8\,\mathrm{k\Omega}$, i.e. $R_\mathrm{T} \gg R_\mathrm{K}$. The junction resistances in the device of Papers I and II are of the order of $10\,\mathrm{M\Omega}$ fulfilling the condition.

Elastic cotunneling, local and non-local Andreev tunneling all acquire the following simple form when $\delta E, k_\mathrm{B}T \ll \Delta$,

$$\Gamma_{2e}(\delta E, T) = \gamma \frac{\delta E/k_\mathrm{B}T}{1 - e^{-\delta E/k_\mathrm{B}T}} k_\mathrm{B}T, \tag{2.18}$$

where the prefactor γ depends on whether the process is local or non-local. The tunneling rates for the local and non-local two-electron tunneling processes were measured in Papers I and II in operation points where the initial and final states of transitions are degenerate in energy. In the limit of zero energy cost $\lim_{\delta E \to 0} \frac{\delta E/k_\mathrm{B}T}{1-\mathrm{e}^{-\delta E/k_\mathrm{B}T}} = 1$, the two-electron rates attain a simple form

$$\Gamma_{2e}(\delta E \to 0, T) = \gamma k_\mathrm{B}T, \tag{2.19}$$

which shows linear temperature dependence. The prefactor γ in Equation (2.19) for the local and non-local rates reads as

$$\begin{aligned}\gamma_{\mathrm{local}} &= \frac{1}{8e^2 R_{T\alpha}^2}\frac{R_{\mathrm{K}}}{\mathcal{N}_\alpha} \\ \gamma_{\mathrm{non-local}} &= \frac{\mathrm{e}^{-l/\xi}}{2e^2 R_{TL} R_{TR}} R_{\mathrm{S}},\end{aligned} \tag{2.20}$$

where $R_{\mathrm{T}\alpha}$ is the junction resistance of the tunnel junction contacting island α and the superconductor, R_{S} is the normal-state resistance of the superconducting electrode measured over coherence length ξ. $R_{\mathrm{K}} \equiv h/e^2$ is the so-called resistance quantum, h is the Planck's constant. $\mathcal{N}_\alpha = A_\alpha / A_{\mathrm{ch},\alpha}$ is the effective number of the conduction channels in junction $\alpha = \mathrm{L}, \mathrm{R}$ with a junction area A_α and effective conduction channel area $A_{\mathrm{ch},\alpha}$ [33]. l is the separation between the two junctions.

2 Real-time detection of Cooper pair splitting (Paper I)

After the theoretical background presented in Section 1, detection of tunneling events in real time is discussed in this section. In section 2.1 the concept of a Cooper pair splitter is introduced as well as the work done in the field paving the way for experiments in Papers I and II. In this section different detection schemes are discussed as charge counting technique was a key component to accomplish the first real-time detection of Cooper pair splitting in Paper I.

Section 2.2 displays the device in Papers I and II consisting of a grounded superconducting electrode coupled to two normal-state metallic islands via tunnel junctions. The junctions are in the close proximity of each other to allow non-local two-electron processes. The small separation l between the junctions makes the exponential term of $\gamma_{\mathrm{non-local}}$ given by Equation (2.20) large thus allowing finite rates as seen in Equation (2.18). Section 2.3 goes into details how the two single-electron transisors (SETs) capacitively coupled to the metallic islands function as sensitive charge detectors reading out the charge state on the islands in real time. Recording current as a function of time through the SETs allows one to tap into time-resolved statistics of the tunneling events. A current measured in time domain is called a time trace. Section 2.4 explains how tunneling rates for different processes are extracted from time traces.

Distinguishing all tunneling processes from each other in time traces allows one to tap into the statistics of tunneling events in Section 2.5. Auto-correlation

function takes into account tunneling events on only one island and cross-correlation function events on both islands. The correlation functions reveal the relevant timescales in the detection and the cross-correlation function exhibits a pronounced peak two orders of magnitude above the background providing solid evidence for the presence of correlated tunneling events involving separate islands.

2.1 Cooper pair splitter

CPS device was first theoretically outlined twenty years ago [39, 40]. Common component to all Cooper pair splitters is a superconducting reservoir providing Cooper pairs. By coupling the superconductor to conducting material Cooper pairs can be extracted out of the reservoir. Superconductor is a natural host for solid-state entanglement as the two electrons of a Cooper pair form a spin-singlet state $(|\uparrow\downarrow\rangle - |\downarrow\uparrow\rangle)/\sqrt{2}$ [91] if the superconductor is s-wave type [75] as is the case for aluminium [13]. Soon after the advent of quantum mechanics it was realized by A. Einstein, B. Podolsky, N. Rosen [92] and E. Schrödinger in the 1930s that the newly discovered physical reality contained a peculiar feature which in essence stated that there exists global states of composite subsystems that are not possible to be formulated as product states of the constituting parts of the total system [93]. This implies e.g. in the case of a spin-singlet state of electrons that whenever the spin of one of the electrons is measured the spin of the other one is immediately known regardless of the distance between the two particles.

These correlations between spatially separate entangled particles, commonly known as EPR pairs, can be utilized to test the foundations of quantum mechanics by verifying if Bell inequality is violated [94, 14]. The first convincing experimental evidence of the violation was provided by A. Aspect et al. in the early 1980s [95, 96]. Generation of solid-state entanglement is straightforward as described above. It is achieved simply by cooling down a piece of metal exhibiting superconducting properties at low temperatures below its critical temperature. Entanglement can be harnessed from a superconductor by splitting a Cooper pair to conductors connected to it and the individual electrons of the pair are now collected in different arms. So far no one has verified entanglement between the electrons from a split pair. The splitting has been demonstrated with various types of arms: ferromagnetic leads [10], normal-state metal leads [15, 17, 18], semiconducting quantum dots [11, 19, 20] or quantum dots in carbon nanotubes [12, 26].

Ferromagnetic leads allow opposite spin-polarization of the arms and Cooper

pair splitting can be detected in a spin-dependent non-local resistance measurement [10]. Normal-state leads host a mixture of different spins and thus set no condition what spin directions electrons coming from the superconductor should possess. In the case of normal-state arms split Cooper pairs are observed by measuring non-local voltage [15], non-local differential resistance oscillations [17] or noise cross-correlation [18]. Non-local differential conductance measurements have been performed in splitting to semiconducting quantum dots [11, 19, 21] or carbon nanotube defined quantum dots [22].

Although all of these measurements have been successful in showing the characteristic sign of split Cooper pairs they rely on detecting an ensemble of many split events. The measured signals contain many split pairs and it is not known to the observer at which exact moments in time a split pair enters the arms. This inability to pinpoint individual splitting events hinders the use of correlated electrons for any device functionality.

A fundamentally different route for detection was taken in Paper I. Instead of two drain leads the split electrons are collected into two small metallic islands and their arrival causes a noticeable change in the electrostatic potentials of the islands which can be detected in real time by SET electrometry. As both of the islands are capacitively coupled to individual electrometers the splitting event is seen as currents through both detectors switch simultaneously. This first real-time detection is an important step towards utilizing the spin-entanglement of split Cooper pairs and the details of the experimental setup and how the split events are extracted from the detector signals are given in this chapter.

2.2 Device architecture

Figure 2.3 displays a scanning electron micrograph of a CPS device in Paper I and II. The grounded superconducting aluminium electrode is coupled to two normal-state copper islands via aluminiumoxide tunnel junctions. The inset inside the main micrograph shows the junction configuration. The distance between the junctions is $l \approx 100\,\mathrm{nm}$ estimated from a scanning electron micrograph and thus around the same as the superconducting coherence length $\xi \approx 100\,\mathrm{nm}$ which is a typical value for the aluminium film used in our system [97]. $l \approx \xi$ is a crucial requirement to observe non-local Andreev tunneling as ξ is a characteristic length scale for the size of a Cooper pair and the non-local tunneling processes are exponentially suppressed as $\exp(-\mathrm{l}/\xi)$ seen in Equations (2.18) and (2.20).

The superconducting electrode not only provides Cooper pairs but also acts as

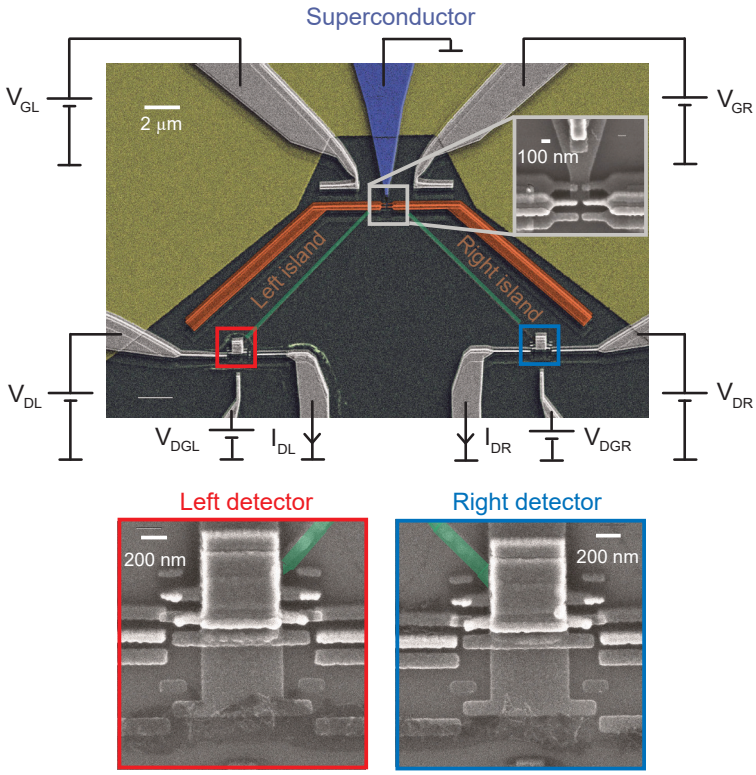

Figure 2.3: Cooper pair splitter. Scanning electron micrograph of the superconducting aluminum electrode tunnel-coupled via insulating aluminumoxide layers to two normal-state copper islands coloured in orange. The inset in the upper right corner shows the tunnel junctions. The thin chromium strips coloured in green capacitively couple the islands to distinct single-electron transistors which act as sensitive electrometers which are zoomed in below the main micrograph. Figure is adapted from Paper I.

a barrier for sequential tunneling as electrons need to be excited over the gap. Hence, the gap introduces an exponential suppression to sequential tunneling rates and subgap transport in the form of two-electron processes becomes an important charge transfer mechanism between the superconductor and the metallic islands.

The electrostatic energies of the islands are given by Equation (2.14) as $E_\alpha(n_\alpha) = E_{C\alpha}(n_\alpha - n_{G\alpha})^2$, where the subscript $\alpha = \mathrm{L}, \mathrm{R}$ denotes either the left or the right island respectively. The normalized gate-offset charge $n_{G\alpha} = C_{G\alpha}V_{G\alpha}/e$ is controlled experimentally by the gate voltages $V_{G\alpha}$ shown in Fig. 2.3. The electrostatic energies of the islands have a parabolic form and therefore a unique minimum at some certain n_α value. By varying the applied gate voltage the electronic populations are controlled. The occupation probabilities of the charge states then determine which tunneling processes are energetically preferable.

In Fig. 2.3 the yellowish part covering roughly half the background is the ground plane. The metallic islands are placed as far away as possible from each other and close to the ground plane in order to minimize the capacitive coupling between the islands. Coulomb interaction between the metallic islands would favour elastic cotunneling as the splitting would require additional energy to overcome the repulsion between the two electrons tunneling into separate islands. Near the tunnel junctions the islands are close to each other but in this region their Coulomb interaction is screened by the superconducting electrode.

The charge states on the metallic islands are monitored by two SETs, one for each island, which are shown in zoom-ins in Fig. 2.3. The islands are capacitively coupled to SET detectors via chromium strips in green. The detectors are biased by voltages $V_{\mathrm{D}\alpha}$, gated by voltages $V_{\mathrm{DG}\alpha}$ and the currents $I_{\mathrm{D}\alpha}$ are simultaneously measured through the detectors.

2.3 Charge detection

Two important electronic occupation distributions on the islands are obtained by setting the normalized gate offset charge $n_{\mathrm{G}\alpha}$ in Equation (2.14) to either integer or half-integer value. The two regimes differ by which electron numbers are degenerate in energy. In the case of $n_{\mathrm{G}\alpha} = 0$ the excess electron numbers $n_\alpha = -1$ and $n_\alpha = 1$ have the same energy as demonstrated in Fig. 2.4 (a). For the operational point $n_{\mathrm{G}\alpha} = 1/2$ the electron numbers $n_\alpha = 0$ and $n_\alpha = 1$ have the same energy as demonstrated in Fig. 2.4 (b).

In Fig. 2.4 (a) the offset on the right island is set to $n_{\mathrm{GR}} = 0$. This makes the charge states $n_{\mathrm{R}} = \pm 1$ degenerate in energy and thus the local Andreev tunneling which changes the electron number by two becomes the energetically preferred charge transfer mechanism as this process occurs at zero energy cost. This tuning is called Coulomb blockade as single-electron tunneling requires a finite energy. In the time trace in Fig. 2.4 (a) the island is seen to reside at the lowest-lying energy state $n_{\mathrm{R}} = 0$ before making occasional transitions to higher-lying states $n_{\mathrm{R}} = \pm 1$. In these sequential tunneling events one electron either tunnels into (out of) the island leaving it in the state $n_{\mathrm{R}} = 1$ ($n_{\mathrm{R}} = -1$). Once the island has entered a higher-lying state tunneling processes either adding or subtracting the charge by amount 2e occur at no energy cost as both the initial and final states lie at the same energy. An avalanche of Andreev events is observed when the charge state alternates between degenerate states $n_{\mathrm{R}} = 1$ and $n_{\mathrm{R}} = -1$ until relaxation back to $n_{\mathrm{R}} = 0$ and the sequence can start all over again.

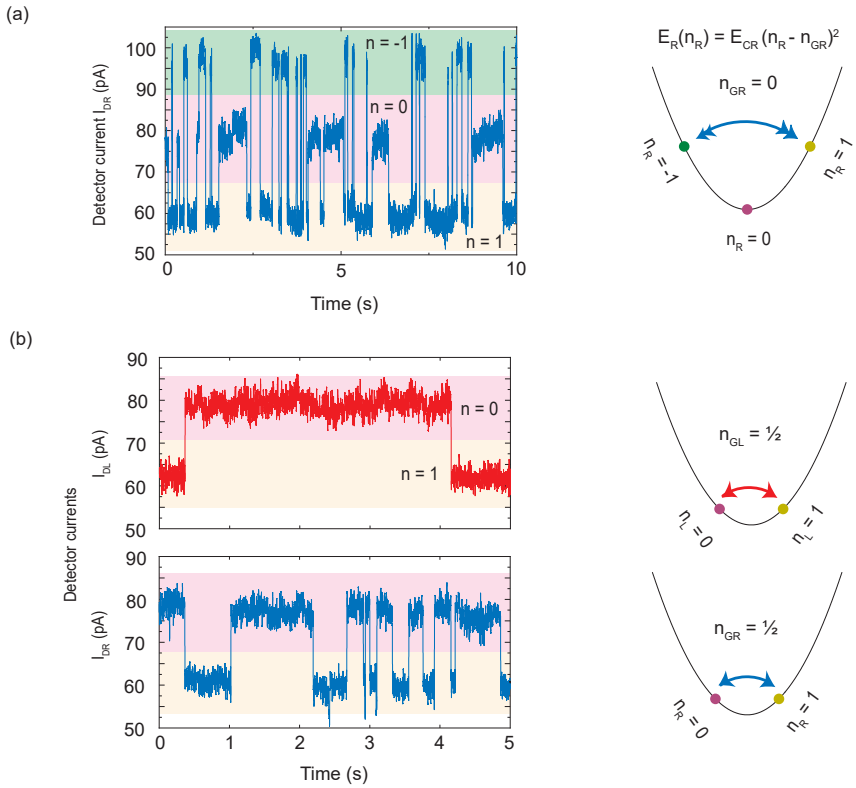

Figure 2.4: Electronic occupations in Coulomb blockade and degeneracy. (a), By tuning the right island into Coulomb blockade $n_{\mathrm{GR}} = 0$ the charge states -1 and 1 end up being degenerate in energy favouring tunneling processes changing the electron number by two on the island. A typical measured time trace and charging energy diagram at this operating point. This operating point is applied to determine tunneling rates for local Andreev tunneling. (b), When both islands are tuned to $n_{\mathrm{G}\alpha} = 1/2$ the adjacent charge states 0 and 1 become degenerate in energy which favours tunneling processes changing the electron number by one on individual islands which is the case for non-local two-electron processes. The red and blue curves are examples of simultaneously measured time traces on the left and right island respectively. Thus the degeneracy point is used to measure tunneling rates for non-local Andreev tunneling and elastic cotunneling.

If the offset is moved from $n_{\mathrm{GR}} = 0$ towards $1/2$ the lowest-lying state $n_{\mathrm{R}} = 0$ is lifted in energy and the state $n_{\mathrm{R}} = 1$ lowered till the two states became degenerate at the offset $n_{\mathrm{GR}} = 1/2$ in Fig. 2.4 (b). This operating point is referred to as degeneracy in literature. At this second operating point the island is occupied by zero and one excess electrons equal amount of time. The tunneling processes in which one electron either enters or leaves the island are the preferred charge transfer mechanisms as these events occur at zero energy cost. Both the non-local two-electron and the sequential tunneling processes keep the islands in their lowest-lying states but the latter one is suppressed as it requires electrons to be excited above the superconducting gap whereas the former takes place at subgap energies.

In the remainder of this section charge detection is described when both islands are tuned to degeneracy where the normalized charge offsets are tuned to 1/2. All the data in Paper I was recorded at this operating point to detect non-local tunneling processes. The detection is performed in a similar fashion for Coulomb blockaded case in Section 3 when comparing the local and non-local two-electron coupling coefficients against each other.

60 s long time traces were simultaneously recorded with a multichannel analog-to-digital converter at a sampling rate of 20 kHz. The detector currents exhibit Coulomb oscillations and the detectors were set to charge sensitive operating points at the steepest part of the current slope. At this point the detector is most sensitive and also the dynamical range is maximized. The detector operating point was slowly drifting in the measurements. This was compensated by applying a feedback-loop. The compensation was achieved by measuring 60 s long time traces and gate voltages were adjusted accordingly in between. The detector signals were digitally filtered through a low-pass filter for which the cut-off frequency was set at 200 Hz. This sets the detector rise time to around 4 ms which describes how quickly the detector responds to tunneling events.

Figure 2.5 shows few seconds long clips of simultaneously measured detector currents monitoring the charge states on the left island (red curve) and on the right island (blue curve). In the beginning of the clips the right island stays around current of 60 pA as no transfer takes place between the island and the superconductor. At the instant ① the left detector current abruptly switches from 60 pA to 80 pA as an electron tunnels out of the island into the superconductor. This sequential tunneling event is illustrated in panel (b) displaying charge transfer across tunnel junctions. Switching of both detector currents is observed seemingly instantaneously to same direction at the instant ②. This is a sign of Cooper pair splitting. At the instant ③ another sequential tunneling event takes place when an electron tunnels this time out the right island.

At the instant ④ both detector currents switch again almost simultaneously, except now to different directions. An electron from the left island tunnels into the right island via a virtual state in the superconductor in this elastic cotunneling event. In panel (a) the charge counting technique clearly tells non-local Andreev tunneling and elastic cotunneling apart by simply observing whether the signals switch to same or opposite directions.

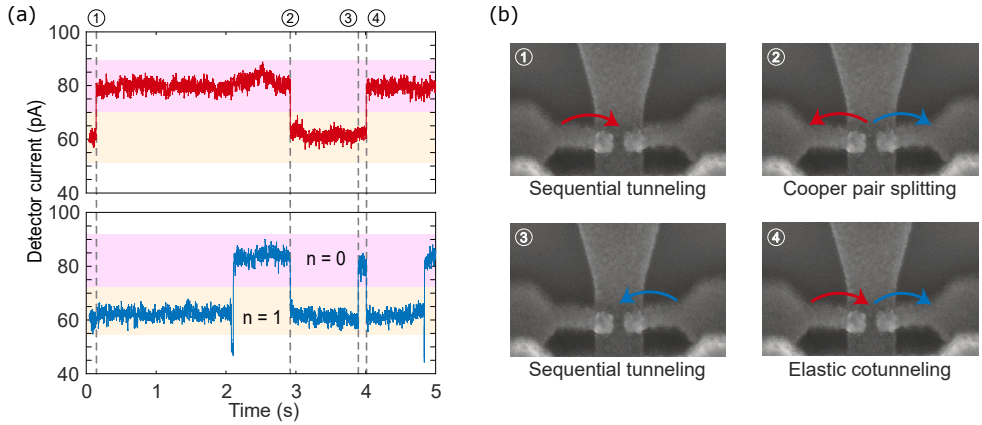

Figure 2.5: Real-time observation of Cooper pair splitting. (a), Simultaneously measured time traces through the left (red) and the right (blue) detector. The currents fluctuate between two distinct levels revealing the excess electron number in real time. (b), The points ① and ③ display sequential tunneling out of the islands. The point ② shows an event where the two electrons forming a Cooper pair tunnel into separate islands at the same time. In an elastic cotunneling event shown by point ④ an electron from the left island tunnels via a virtual state in the superconductor into the right island. Figure is adapted from Paper I.

2.4 Data analysis

Instantaneous charge state

The data shown in this section are measured at half-integer offsets $n_{G\alpha}$. A typical time trace of 60 s is shown in Fig. 2.6 (a). In the Cooper pair splitting measurements in Paper I several traces were recorded at the electronic base temperature of 50 mK in a dilution refrigerator. As described earlier the detector currents switch between distinct levels. Each level corresponds to a certain charge state on the monitored islands and the shifts reveal the transitions between the states when electrons tunnel into or out of the islands. The levels are not completely constant as the detector currents drift and due to the presence of noise. Occasionally there was too much drifting making it ambiguous to distinguish charge states from each other in the detector signal. This leads to a need to dismiss certain time traces from the analysis. Thus rigorous data analysis is needed to extract the instantaneous charge state in the detector signal and further the tunneling rates.

The sampling rate for recording the current was 20 kHz. For 60 s long time traces the step size of 50 μs yield 1.2×10^6 current data points in total. Statistical arguments are applied to determine which data point belongs to which charge state. By dividing all current data points in Fig. 2.6 (a) into 100 equally wide bins the histogram presented in Fig. 2.6 (b) is obtained. The two lowest-lying states appear clearly as the two highest peaks denoted by $I_{0,1}$. These peaks

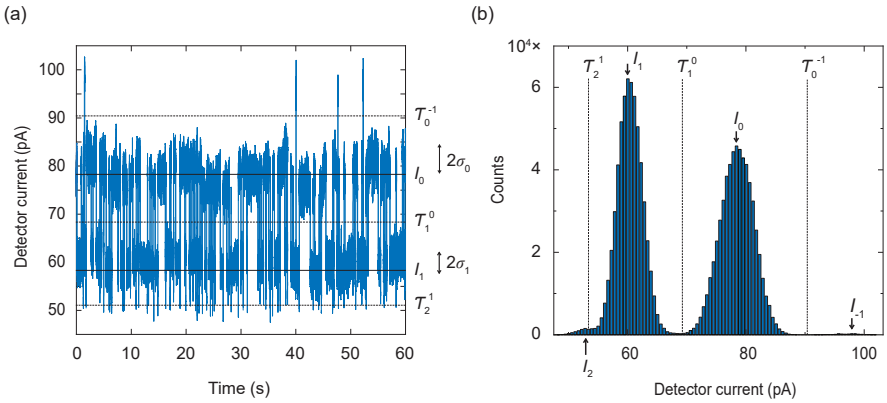

Figure 2.6: Detector current. (a), The thresholds $\mathcal{T}_j^i$ marked by the dashed lines determine how current is partitioned between the charge states. The solid black lines indicate the current levels I_0 and I_1 of the lowest-lying charge states. σ_0 and σ_1 denote the standard deviations of the currents at the charge states. (b) The current from panel (a) allocated in 100 bins. The current levels of the four charge states 2, 1, 0 and -1 are visible in the histogram as the four peaks. The current in the individual levels is given by a Gaussian distribution. Figure is adapted from Paper I.

are found by first locating the highest peak I_h and removing all current around it within $I_\mathrm{h} \pm 2\sigma$, where $\sigma = 2.5\,\mathrm{pA}$ is the average current noise. The highest peak is again located in the remaining data and denoted by I_sh. The current levels at charge states 0 and 1 are determined to be $I_0 = \max(I_\mathrm{h}, I_\mathrm{sh})$ and $I_1 = \min(I_\mathrm{h}, I_\mathrm{sh})$.

If the islands are properly tuned to degeneracy point $n_{\mathrm{G}\alpha} = 1/2$ they spend equal amount of time at charge states 0 and 1. A criterion is set how much the populations are allowed to deviate from the desired 50-50 division. This is accomplished by demanding that the ratio N_0/N_1 stays within certain bounds where N_j is the number of counts in the bin I_j. If the time trace satisfies $1/2 < N_0/N_1 < 2$ it is included in the analysis, otherwise disregarded.

The detector currents do not stay at perfectly constant levels when the electron number on the islands is fixed but drift from their mean value. Due to the drift the current occasionally visits the range between the mean current levels. In this case it is not clear whether those current points belong to the charge state 0 or 1. In Fig. 2.6 the amount of current residing between the levels is visible and can be quantified by the height of the valley N_valley between the peaks $I_{0,1}$. In some time traces the current drifts to a distinct level in the valley and a local maximum N_valley forms. In the other traces mainly the transitions between the states contribute to valley and no local maximum forms and the minimum in the interval $[I_1 + 2\sigma, I_0 - 2\sigma]$ is set as N_valley. If the ratio $N_\mathrm{valley}/\min(N_0, N_1) < 0.05$ the time trace is included in the analysis.

Now the current levels corresponding to the charge states 0 and 1 are identified. The islands are occasionally excited to energetically higher-lying charge states -1 (2) which can be seen in the detector signal in Fig. 2.6 (a) as levels above (below) I_0 (I_1). If there is maximum below $I_1 - 2\sigma$ (above $I_0 + 2\sigma$) it is set as I_2 (I_{-1}). After having determined the mean current levels all current points are allocated to charge states. This is done with the help of thresholds based on the histogram peaks.

To distinguish the charge states 0 and 1 in the signal a threshold $\mathcal{T}_1^0$ is set in the midway between the levels I_0 and I_1. Setting the thresholds between I_0 and I_{-1} (I_1 and I_2) is not as straightforward. In Fig. 2.6 (a) charge state 2 is less pronounced than -1. If the midway was applied between the states 1 and 2 the threshold would cut the noise level of the state 1. Therefore a different strategy must be used for the higher-lying states. If I_{-1} (I_2) exists the threshold is set at the minimum in the interval $[I_0 + 2\sigma, I_{-1},]$ ($[I_2, I_1 - 2\sigma]$). In case I_{-1} (I_2) does not exist all current above (below) $\mathcal{T}_1^0$ is taken to belong the state 0 (1). The instantaneous charge state of the island is now determined and this allows one to study the transitions in the system.

Tunneling rates

After assigning the instantaneous charge state the time trace is digitized, i.e. all current points are mapped to states -1, 0, 1 and 2 allowing one to study the transitions and extract the tunneling rates. The rates are determined as in Ref. [33]. A local tunneling rate from the charge state i to f is computed as $\Gamma_{i\to f} = m_{i\to f}/t_i$ where $m_{i\to f}$ is the number of $i \to f$ events and t_i the total time spent in the initial charge state i. Rates for the non-local processes are computed similarly except now one needs to consider the combined charge state of the two islands. The rate for a non-local process in which a transition $i \to f$ on the left island and $j \to g$ on the right island is computed as $\Gamma_{i\to f}^{j\to g} = m_{i\to f, j\to g}/t_{i,j}$ where $m_{i\to f, j\to g}$ is the number of non-local events and $t_{i,j}$ is the time the left island spends at i and the right island at j simultaneously.

In the following, a method to distinguish local and non-local two-electron tunneling events from sequential tunneling events is described. To distinguish local Andreev events from two closely happening sequential tunneling events, the argument put forward in Ref. [33] is followed. Figure 2.7 (a) shows the lifetime distribution at the charge state 0 on the right island. Most points fall nicely into an exponential arising from a random process except the one at very short time. This point is credited to local Andreev tunneling and two closely happening one electron transitions to same direction are interpreted as an Andreev event.

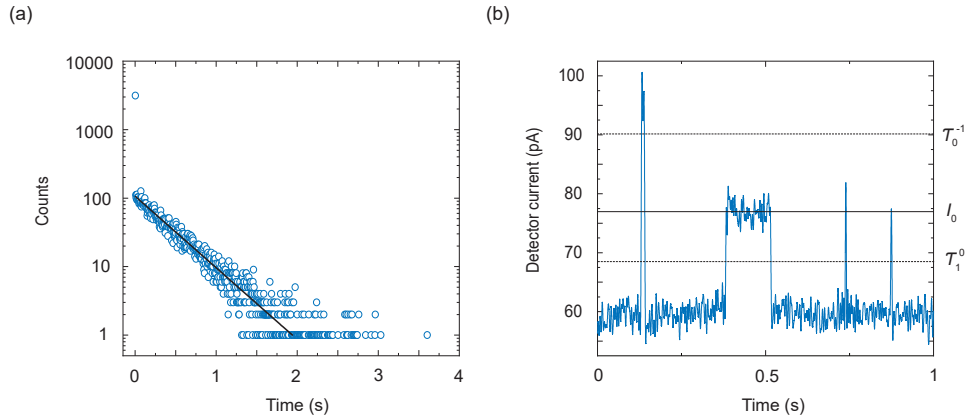

Figure 2.7: Life-time distribution. (a), Time spent in the charge state 0 of the right island recorded between tunneling events into and out of the island. The bin size is 4 ms. The anomalous high short time data point arises from local Andreev tunneling. Apart from the shortest time point the rest of the distribution follows an exponential fall-off. (b), The leftmost peak shows a local Andreev tunneling from $n_R = 1 \rightarrow -1$ and its time reversal process to opposite direction. Duration the detector current spends at $n_R = 0$ is less than the detector rise time of 4 ms. The wide peak in the middle of the graph corresponds to a sequential tunneling $n_R = 1 \rightarrow 0$ and its time reversal process. The two sharp peaks on the right side are local Andreev tunneling events which take the right island $n_R = 1 \rightarrow -1$ and are followed by another local Andreev back to $n_R = 1$ but these events happen in a time shorter than the detector rise time and thus it appears as if there were tunneling sequences $n_R = 1 \rightarrow 0 \rightarrow 1$. Figure is adapted from Paper I.

However, even after doing this sorting the very short time point remains above the exponential fall-off. In Fig. 2.7 (b) it is explained why this is the case with the help of a signal showing events giving rise to this short-time peak. On the left closely happening $1 \rightarrow 0$ and $0 \rightarrow -1$ transitions can be seen and the reverse order back to the state 1. The time spent at the intermediate state 0 is short and yields extensively many counts to the shortest time bin in the lifetime distribution. Two one electron transitions taking place to same direction within 4 ms are interpreted to arise from local Andreev tunneling process as in [33]. Around 0.5 s a typical example of sequential tunneling is seen. A single electron tunnels out of the right island and after some time an electron tunnels back.

The other transition type contributing to the anomalous short time point in Fig. 2.7 (a) is visible in the detector signal in Fig. 2.7 (b) around 0.7 s and 0.9 s. In this case the detector current rises from the initial charge state 1 to 0 and returns quickly back to the initial state. The time spent at the charge state 0 is below 4 ms. Based on the short time point in the lifetime distribution these two peaks do not represent sequential tunneling events $1 \leftrightarrow 0$. Instead, one such peak is interpreted to be caused by two local Andreev tunneling events, namely $1 \rightarrow -1$ followed by $-1 \rightarrow 1$. The reason why these two local Andreev events appear as sequential events in the signal is that the return event $-1 \rightarrow 1$ is fast the detector current does not have time to cross the upper threshold $\mathcal{T}_0^{-1}$. The cases with a fast return event, the time spent at the charge state 0 (or 1) shorter

than 4 ms, are not included in computing the tunneling rates.

This procedure distinguishes all local tunneling processes from each other. While only looking at one side of the system information about which transitions arise from non-local tunneling processes cannot be obtained. To identify the non-local events in the signals one needs to look at the simultaneously measured detector current for the left side. The criterion to label non-local events is given by cross-correlation function which is discussed in detail in Section 2.5. Here, $0 \leftrightarrow 1$ happening within 1.5 ms window are interpreted as non-local events. Now that all tunneling processes are identified in the detector signals the tunneling rates can be computed by the method described earlier.

2.5 Statistical analysis

In non-local two-electron events the charge states of the two islands change virtually instantaneously. The limit for 'almost simultaneity' is set by the time-energy uncertainty and the time separation between transitions on different islands is characterized by $\hbar/\Delta$ which is of the order of picoseconds and much smaller than the timing accuracy of the setup in Papers I and II. The timing accuracy in this setup is essentially characterized by two parameters, detector rise time and noise in detector current. The statistical tools applied are $g^{(2)}$-correlation function and waiting time distribution [98]. This section focuses on how these quantities are determined from the measured signals.

Correlation functions

$g^{(2)}$-function quantifies correlations between two types of transitions α and β and it is defined as

$$g^{(2)}(t, t+\tau) = \frac{\rho_{\beta\alpha}(t+\tau, t)}{\rho_\alpha(t)\rho_\beta(t+\tau)}, \tag{2.21}$$

where $\rho_\alpha(t)$ is the probability density of an event of type α occurring at time t and $\rho_{\beta\alpha}(t+\tau, t)$ is the joint probability density of an event of type α taking place at t and event of type β at $t+\tau$ [98]. In the steady state $g^{(2)}$-function is only a function of the time separation between the events and $g^{(2)}(t, t+\tau) \equiv g^{(2)}(\tau)$.

Auto-correlation function involves local tunneling events taking place between the superconductor and one of the islands whereas cross-correlation function

accounts for events taking place on different islands. Obtaining both of these correlation functions as well as waiting time distributions is an easy task after the identification of the tunneling events earlier.

In the auto-correlation shown in Fig. 2.8 (a) correlations between tunneling events $0 \to 1$ are studied where one electron tunnels into the right island. For each $0 \to 1$ event the number of $0 \to 1$ events is counted after or before a time τ around the time interval $\Delta\tau = 100\,\mathrm{ms}$. By diving the number of counts by the normalization factor $(\dot{N}^{\mathrm{R}}_{0\to1})^2 \times t_{\mathrm{tot}} \times \Delta\tau$ yields the experimental data points in Fig. 2.8 (a). $\dot{N}^{\mathrm{R}}_{0\to1}$ is the number of $0 \to 1$ events per measurement time t_{tot}. The theoretical curve in Paper I is given by

$$g^{(2)}(\tau) = 1 - \mathrm{e}^{-\gamma|\tau|}, \tag{2.22}$$

where $\gamma = 4.5\,\mathrm{s}^{-1}$ is the inverse correlation time. Suppression of the auto-correlation function is seen at a timescale of roughly one second around zero time. This suppression arises from the fact that only one electron can tunnel into the right island at a time due to the strong Coulomb interactions.

For the cross-correlation function in Fig. 2.8 (b) events on separate islands are counted to study the occurrence of non-local tunneling events which involve charge transitions on both islands. In a non-local Andreev tunneling event charge states on both islands switch either $0 \to 1$ (Cooper pair splitting) or $1 \to 0$ (Cooper pair forming) nearly instantaneously. In an elastic cotunneling event one the island switches $1 \to 0$ and the other one $0 \to 1$ shortly afterwards. The number of $0 \leftrightarrow 1$ transitions on the right island is counted around the time interval $\Delta\tau = 150\,\mu\mathrm{s}$ before or after a time τ from $0 \leftrightarrow 1$ transitions on the left island. Number of counts is divided by the normalization factor $\dot{N}^{\mathrm{L}}_{0\leftrightarrow1} \times \dot{N}^{\mathrm{R}}_{0\leftrightarrow1} \times t_{\mathrm{tot}} \times \Delta\tau$, where $\dot{N}^{\alpha}_{0\leftrightarrow1}$ is the number of $0 \to 1$ and $1 \to 0$ events per measurement time t_{tot}. Normalization sets the function value at long times at one. This yields the experimental data points in Fig. 2.8 (b). The theoretical curve in Paper I is given by

$$g^{(2)}_x(\tau) = 1 + \alpha_2 \frac{\mathrm{e}^{-\frac{1}{2}(\tau/\sigma_{\mathrm{D}})^2}}{\sqrt{2\pi}\sigma_{\mathrm{D}}}, \tag{2.23}$$

where $\alpha_2 = 210\,\mathrm{ms}$ is the time-integrated contribution from two-electron processes and $\sigma_{\mathrm{D}} = 460\,\mu\mathrm{s}$ is the broadening due to timing jitter of the detectors. In the cross-correlation function in Fig. 2.8 (b) pronounced bunching is present at very short time in stark contrast to the autocorrelation function. This sharp

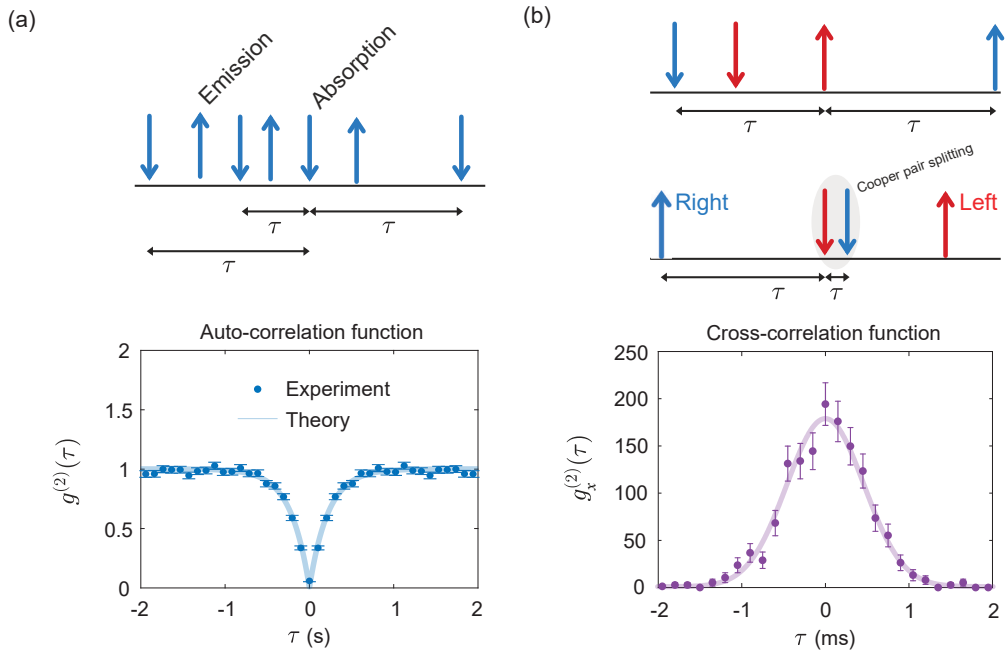

Figure 2.8: Correlation functions. (a), The schematics describes the determination of time differences τ between $0 \rightarrow 1$ events on the right island. Downwards pointing arrow denotes a $0 \rightarrow 1$ event whereas upwards pointing a $1 \rightarrow 0$ event. The plot shows the auto-correlation function for tunneling into the right island. (b), The schematics for determining time differences τ between $0 \leftrightarrow 1$ events on the left island and $0 \leftrightarrow 1$ events on the right island. The red arrows are for the left island and blue arrows for the right island. The plot shows the cross-correlation function for $0 \leftrightarrow 1$ events between the left island and the superconductor at $t = 0$ and $0 \leftrightarrow 1$ events between the superconductor and the right island at time $t = \tau$. The error bars mark 1σ confidence intervals. The plots are adapted from Paper I.

peak with its top two orders of magnitude above the background signal arises from the non-local two-electron tunneling events. The cross-correlation function tells that whenever a $0 \leftrightarrow 1$ event takes place on the left island it is more likely that a $0 \leftrightarrow 1$ event occurs shortly afterwards (or beforehand) on the right island rather than with long time separation. This is a direct manifestation of the non-local tunneling events in the system. The width of the cross-correlation peak is on milli-second timescale and $0 \leftrightarrow 1$ events taking place on different islands within 1.5 ms from each other are interpreted to arise from non-local processes.

Resolution in correlation functions

Here, the timescales entering the auto and cross-correlation measurements are discussed. In Fig. 2.9 (a) an example is presented about how one count is obtained for the auto-correlation function. τ represents the time difference between two consecutive $0 \rightarrow 1$ events to demonstrate what causes the anti-bunching seen

in Fig. 2.8 (a). t_{rise} is the detector rise time around 4 ms set by the digital filtering of the signal. Ultimately τ is limited by t_{rise} as the detector current needs to cross the threshold level between the charge states in order to register events. It is obvious from Fig. 2.8 (a) that additional timescale playes a role as t_{rise} cannot explain roughly one second wide dip. Anti-bunching at short times arises from strong Coulomb repulsion on the metallic island as after an electron tunnels into the island from the superconductor, the island needs to emit an electron before it can absorb again.

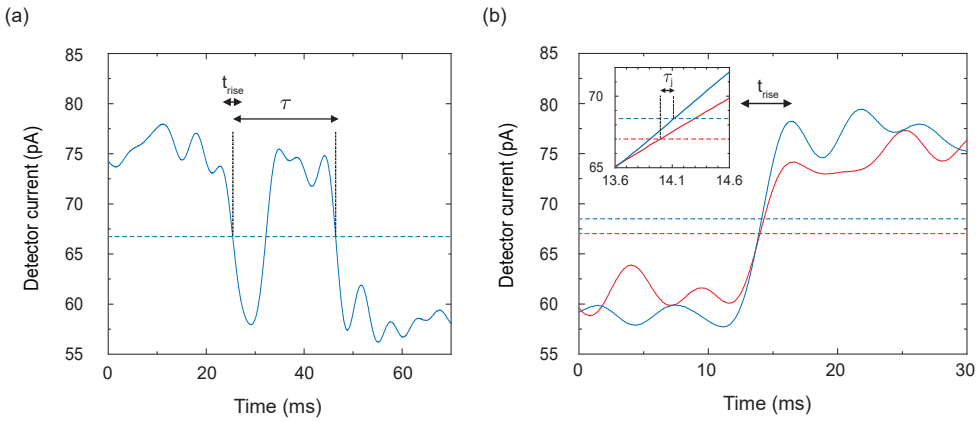

Figure 2.9: Time scales for detecting the tunneling events. (a), A typical time trace of the right detector yielding one count to the auto-correlation measurement. The solid line is the measured detector signal and the horizontal dashed line indicates the threshold between charge states 0 (above the line) and 1 (below). The time τ is the separation between two $0 \rightarrow 1$ transitions. t_{rise} is the detector rise time. (b), A typical time trace yielding one count to the cross-correlation measurement. Detector currents for the left and the right islands are shown in red and blue curves respectively. The detectors switch almost simultaneously from the charge state 1 to 0. The observed time separation $\tau_{\mathrm{j}} \ll t_{\mathrm{rise}}$ between the $1 \rightarrow 0$ events on the two distinct islands is indicated in the zoom-in of the inset. Figure is adapted from Paper I.

A different picture emerges when events on separate islands are monitored by two distinct detectors. The millisecond timescale seen in Fig. 2.8 (b) is explained by Fig. 2.9 (b). As the two event types going into the cross-correlation function are read out from different signals the restriction set by the detector rise time is lifted. Instead the timing accuracy is limited by the detector jitter τ_{j} arising from detector current noise. As τ_{j} in the measurements was much smaller than t_{rise} the time resolution in Fig. 2.8 (b) is better than one would expect by simply considering rise times of individual detectors.

Waiting time distributions

The waiting time distribution between two tunneling processes α and β is defined as

$$\mathcal{W}(\tau|t) = \tilde{\rho}_{\beta\alpha}(t+\tau|t), \tag{2.24}$$

where $\tilde{\rho}_{\beta\alpha}(t+\tau|t)$ is the probability density of an event of type β occurring at time $t+\tau$ with the condition that an event of type α took place at time t [98]. Waiting time distribution is exclusive in a sense that it requires that no event of type β happened between t and $t+\tau$. For a steady state $\mathcal{W}(\tau|t) \equiv \mathcal{W}(\tau)$.

The experimental data points in the auto-waiting time distribution in Fig. 2.10 (a) are obtained as following. Subsequent tunneling out of the right island is considered. The time differences τ are counted between consecutive $1 \rightarrow 0$ transitions around a time interval $\Delta\tau$. The number of counts per time interval $\Delta\tau$ is divided by the normalization factor $N_{\text{tot}} \times \Delta\tau$, where N_{tot} is the total number of counts in all intervals, to yield the experimental points in Fig. 2.10 (a). In Fig. 2.10 (a) the auto-correlation function is suppressed for short times as only one electron at a time can tunnel out of the metallic island due to strong Coulomb interactions. The distribution falls off after reaching its maximum as long waiting times are exponentially unlike.

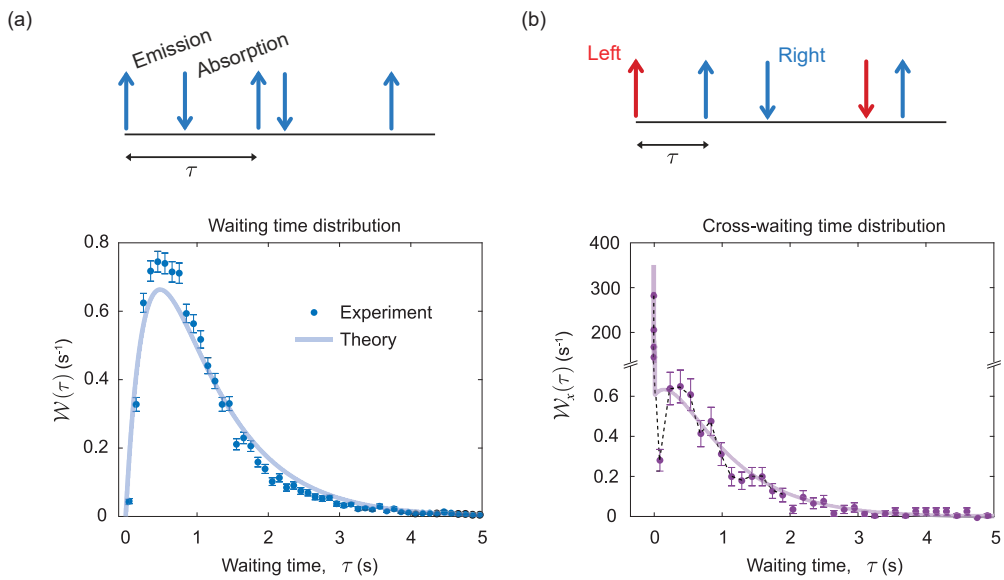

Figure 2.10: Waiting time distributions. (a), The schematics describes the determination of time differences τ between consecutive $1 \rightarrow 0$ transitions on the right island. Downwards pointing arrow denotes a $0 \rightarrow 1$ transition whereas upwards pointing a $1 \rightarrow 0$ transition. The plot shows the auto-waiting time distribution. (b), The schematics for determining time differences τ between $1 \rightarrow 0$ transitions on the left island and $1 \rightarrow 0$ transitions on the right island. The red arrows are for the left island and blue arrows for the right island. The plot shows the cross-waiting time distribution for $1 \rightarrow 0$ transitions between the left island and the superconductor at $t = 0$ and $1 \rightarrow 0$ transitions between the superconductor and the right island at time $t = \tau$. The error bars mark 1σ confidence intervals. The plots are adapted from Paper I.

A very different picture emerges by cross-waiting time distribution. Figure. 2.10 (b) demonstrates the waiting time measured between an electron tunneling out of the left island and a time τ afterwards an electron tunneling out of the right island. Thus $1 \rightarrow 0$ transitions are still considered except now they take place on separate islands. The cross-waiting time distribution is computed the same way as the auto one. For long times the distribution falls off as it is exponentially unlikely that it takes a long time between electron tunneling out of the left and right islands. For short times, instead of suppression, a sharp peak is obtained arising from electrons tunneling within millisecond timescale from separate islands into the superconductor to form a Cooper pair. Alongside the cross-correlation function the cross-waiting time distribution provides strong evidence for non-local tunneling processes in the experiment of Paper I.

3 Coupling coefficients for two-electron tunneling (Paper II)

In this section coupling coefficients for local and non-local two-electron processes are compared against each other. The determination of these coefficients is the main result of Paper II. Comparison between these coefficients is important as they set the tunneling timescales. The two-electron rates are measured at zero energy cost between the initial and final states of the tunneling processes as the rates are predicted to be linear in temperature at zero energy cost in Equation (2.19).

If there is no energy cost between two charge states then the two tunneling processes taking the system back and forth between these states occur at the same rate. Here, the two tunneling directions for Andreev tunneling, local or non-local, are called in and out tunneling depending on whether electrons tunnel into or out of the metallic islands respectively. The natural naming for the elastic cotunneling processes is to call them left to right ($\mathrm{L} \rightarrow \mathrm{R}$) or vice versa depending on to which direction the electron transfer happens. If the aforementioned two states are not degenerate, the in and out rates given by Equation (2.18) can differ considerably from Equation (2.19). In the next section it is shown how the rate at zero energy cost is obtained from the two-electron in and out rates.

3.1 Logarithmic mean

Here, an expression for a tunneling rate at zero energy cost is obtained as a logarithmic mean of a pair of time-reversal processes. If the initial and the final state of a two-electron process are degenerate, the energy difference between the states is zero and the two directions of the process take place at the same rate $\Gamma_{2e}^{in} = \Gamma_{2e}^{out}$. In experiments there is a finite energy difference between the states and the rates of the two directions are not the same. Then for example, Γ_{2e}^{in} has a finite energy energy gain δE and hence Γ_{2e}^{in} acquires an energy cost $-\delta E$. Two-electron rate is given by Equation (2.18) and for Γ_{2e}^{in} and Γ_{2e}^{out} it reads

$$\begin{cases} \Gamma_{2e}^{in} \equiv \Gamma_{2e}(\delta E, T) = \gamma \frac{\delta E/k_B T}{1-e^{-\delta E/k_B T}} k_B T \\ \Gamma_{2e}^{out} \equiv \Gamma_{2e}(-\delta E, T) = \gamma \frac{-\delta E/k_B T}{1-e^{\delta E/k_B T}} k_B T \end{cases} . \tag{2.25}$$

The result in Equation (2.19) together with defining $\delta\mathcal{E} \equiv \delta E/k_B T$ gives

$$\begin{cases} \Gamma_{2e}^{in} = \Gamma_{2e}(0,T) \frac{\delta\mathcal{E}}{1-e^{-\delta\mathcal{E}}} \\ \Gamma_{2e}^{out} = \Gamma_{2e}(0,T) \frac{-\delta\mathcal{E}}{1-e^{\delta\mathcal{E}}} \end{cases} \tag{2.26}$$

The difference between the two rates in Equation (2.26) is

$$\Gamma_{2e}^{in} - \Gamma_{2e}^{out} = \Gamma_{2e}(0,T)\delta\mathcal{E} \underbrace{\left(\frac{1}{1-e^{-\delta\mathcal{E}}} + \frac{1}{1-e^{\delta\mathcal{E}}} \right)}_{=1} \Rightarrow \Gamma_{2e}(0,T) = \frac{\Gamma_{2e}^{in} - \Gamma_{2e}^{out}}{\delta\mathcal{E}}. \tag{2.27}$$

The detailed balance gives $\Gamma_{2e}^{in}/\Gamma_{2e}^{out} = e^{\delta\mathcal{E}}$ and thus $\delta\mathcal{E} = \ln(\Gamma_{2e}^{in}/\Gamma_{2e}^{out})$. This form for $\delta\mathcal{E}$ and Equation (2.27) give the two-electron rate at zero energy cost as

$$\Gamma_{2e}(0,T) = \frac{\Gamma_{2e}^{in} - \Gamma_{2e}^{out}}{\ln(\Gamma_{2e}^{in}) - \ln(\Gamma_{2e}^{out})}. \tag{2.28}$$

3.2 Coupling coefficients

Figure 2.11 displays tunneling rates for local and non-local two-electron tunneling as well as sequential tunneling. The rates for local Andreev tunneling

in panels (a) and (b) were determined in experiments by tuning the electronic occupations on islands to Coulomb blockade as demonstrated in Fig. 2.4 (a). To obtain the non-local two-electron and sequential rates (panels (c)-(f)) the islands were tuned to degeneracy (see Fig. 2.4 (b)) and these processes take place between the charge states 0 and 1. 'CAR' in panel (c) refers to non-local Andreev tunneling. For all two-electron processes rates at zero energy cost are computed by Equation (2.28) and plotted as purple diamonds in Fig. 2.11.

The plots for the two-electron tunneling rates reveal the electronic temperature saturation in the cryostat. In panels (a)-(d) the three lowest temperature data points are saturated and a linear fit is made to points above 50 mK. In the insets of Fig. 2.11 (e) and (f) the solid black lines are the theoretical sequential rates from Equation (2.17).

From the linear fits in Figs. 2.11 (a)-(d) the coupling coefficients γ are extracted by Equation (2.19). This yields $\gamma_{\mathrm{AR,L}} = 7.5 \pm 0.8$µeVs, $\gamma_{\mathrm{AR,R}} = 1.3 \pm 0.1$µeVs, $\gamma_{\mathrm{CAR}} = 9 \pm 1 \times 10^{-3}$ µeVs and $\gamma_{\mathrm{EC}} = 8 \pm 1 \times 10^{-3}$ µeVs. The uncertainties are determined from the linear fits. The results show that $\gamma_{\mathrm{CAR}} = \gamma_{\mathrm{EC}}$ within the experimental accuracy and local Andreev is more than two orders of magnitude stronger than non-local processes.

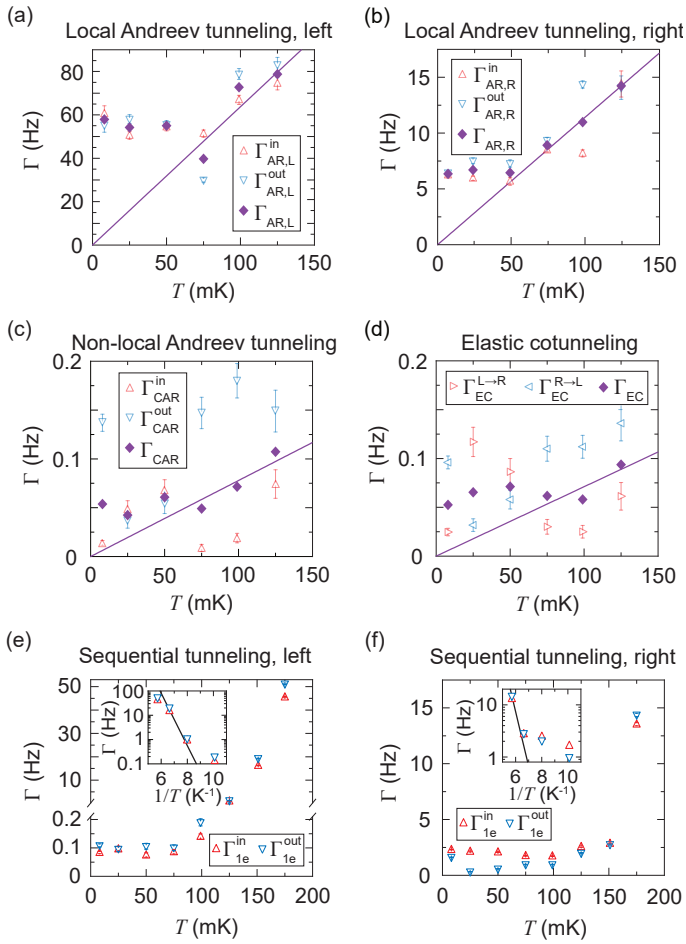

Figure 2.11: 1e and 2e tunneling rates. Panels (a) and (b) show the local Andreev rates in both junctions measured at Coulomb blockade. Panels (c)-(f) show the non-local Andreev, elastic cotunneling and sequential tunneling rates measured at degeneracy. Open symbols denote individual processes. In panels (a)-(c), (e) and (f) the red triangles denote processes where the electron number on the islands increases. The blue triangles stand for processes decreasing the electron number on the islands. In panel (d) the red triangles denote the elastic cotunneling process transferring an electron from the left island to the right island and the blue triangles the opposite direction. The solid purple diamonds in panels (a)-(d) denote the rates at zero energy cost obtained by the logarithmic mean of the in and out rates (or $\mathrm{L} \to \mathrm{R}$ and $\mathrm{R} \to \mathrm{L}$ rates in case of elastic cotunneling). The solid purple lines are linear fits to the zero energy cost rates above $50\,\mathrm{mK}$. The insets in panels (e) and (f) show the four highest temperature rates plotted against inverse temperature. The solid black lines are the theory predictions for sequential rates. Figure is adapted from Paper II.

Chapter 3

Resonator - double quantum dot hybrid system

This chapter provides an introduction to Papers III and IV. Paper III explores two high-impedance resonator devices made out of Josephson junctions. In Paper IV one such resonator is coupled to a semiconductor double quantum dot to probe light-matter interaction between these two systems. Hence, Josephson junction array resonators and semiconductor double quantum dots are key concepts in understanding the results in these two papers. The chapter begins by describing a transmission line for which characteristic impedance is derived. Then, basic properties of a Josephson junction are described and how to form a resonator with increased impedance out of these junctions. Further, a semiconductor double quantum dot is introduced. The device fabrication is described followed by a summary of Paper III. Finally, light-matter interaction is discussed and Paper IV summarized.

1 Transmission line

In this section, charateristic impedance of a transmission line is derived by following Ref. 99. In Fig 3.1 (a) a transmission line is presented as two parallel conducting lines. The electrical properties of this system are evenly spread along the line instead of the system having definite components. $\mathcal{L}$ and $\mathcal{R}$ are the inductance and resistance per unit length respectively. $\mathcal{G}$ and $\mathcal{C}$ are the shunt conductance and capacitance per unit length respectively. However, this distributed-element system can be represented by defining lumped components

each of which gives rise to a certain electrical quantity of the system. An equivalent lumped-element circuit for a δx long piece of a transmission line is shown in Fig. 3.1 (b).

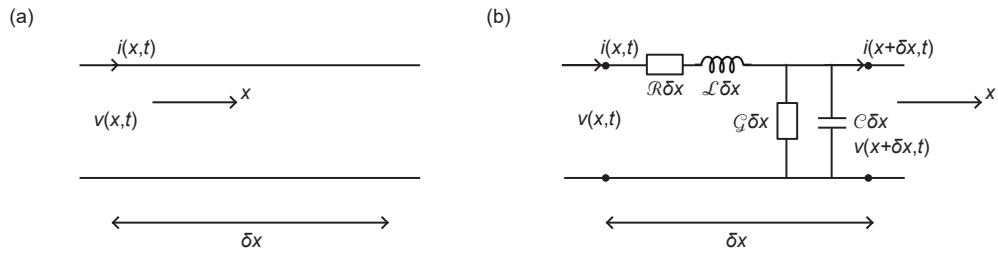

Figure 3.1: (a), A schematic drawing of a transmission line where the current in upper conductor is $i(x,t)$ at point x and time t. $v(x,t)$ stands for the voltage between the lines at position x. (b), An equivalent lumped-element model of panel (a).

Kirchoff's voltage law for the lumped-element circuit in Fig 3.1 (b) reads as

$$v(x,t) - \mathcal{R}\delta x i(x,t) - \mathcal{L}\delta x \frac{\partial i(x,t)}{\partial t} - v(x+\delta x,t) = 0 \tag{3.1}$$

and Kirchoff's current law for the same circuit as

$$i(x,t) - \mathcal{G}\delta x v(x+\delta x,t) - \mathcal{C}\delta x \frac{\partial v(x+\delta x,t)}{\partial t} - i(x+\delta x,t) = 0. \tag{3.2}$$

Time derivatives of the voltage and the current are obtained by dividing the Kirchoff's laws (3.1) and (3.2) by δx and taking $\delta x \to 0$

$$\begin{aligned} \frac{\partial v(x,t)}{\partial x} &= -\mathcal{R} i(x,t) - \mathcal{L}\frac{\partial i(x,t)}{\partial t} \\ \frac{\partial i(x,t)}{\partial x} &= -\mathcal{G} v(x,t) - \mathcal{C}\frac{\partial v(x,t)}{\partial t}, \end{aligned} \tag{3.3}$$

Equations (3.3) describe voltage and current in a tranmission line in time domain. Sinusoidal forms for voltage $v(x,t) = V(x)e^{i\omega t}$ and current $i(x,t) = I(x)e^{i\omega t}$ yield simple differential equations

$$\begin{aligned} \frac{dV(x)}{dx} &= -(\mathcal{R} + i\omega\mathcal{L})I(x) \\ \frac{dI(x)}{dx} &= -(\mathcal{G} + i\omega\mathcal{C})V(x). \end{aligned} \tag{3.4}$$

By defining a complex number $\gamma = \sqrt{(\mathcal{R} + i\omega\mathcal{L})(\mathcal{G} + i\omega\mathcal{C})}$, the coupled differential equations (3.4) separate into wave equations for voltage and current

$$\begin{aligned} \frac{d^2V(x)}{dx^2} - \gamma^2 V(x) &= 0 \\ \frac{d^2I(x)}{dx^2} - \gamma^2 I(x) &= 0. \end{aligned} \tag{3.5}$$

The solutions for the wave equations are

$$\begin{aligned} V(x) &= V_0^+ e^{-\gamma x} + V_0^- e^{\gamma x} \\ I(x) &= I_0^+ e^{-\gamma x} + I_0^- e^{\gamma x}. \end{aligned} \tag{3.6}$$

Plugging the voltage in Equation (3.6) into the spatial derivative of voltage in Equation (3.4) yields for the current

$$I(x) = \frac{\gamma}{\mathcal{R} + i\omega\mathcal{L}}(V_0^+ e^{-\gamma x} - V_0^- e^{\gamma x}) \tag{3.7}$$

Characteristic impedance is

$$Z_\mathrm{r} = \frac{\mathcal{R} + i\omega\mathcal{L}}{\gamma} = \sqrt{\frac{\mathcal{R} + i\omega\mathcal{L}}{\mathcal{G} + i\omega\mathcal{C}}} = \sqrt{\frac{\mathcal{L}}{\mathcal{C}}}, \tag{3.8}$$

where in the last equality $\mathcal{R}$ and $\mathcal{G}$ are set to zero. $\mathcal{R}$ is the resistance per unit length for the transmission line and $\mathcal{G}$ the shunt conductance. These two quantities cause losses in the line. By setting them to zero the transmission line is assumed to be lossless. For example in Ref. 100, for a superconducting Al coplanar waveguide resonator $\mathcal{L} = 453\,\mathrm{nH/m}$ and $\mathcal{C} = 127\,\mathrm{pF/m}$ yield $Z_\mathrm{r} = 60\,\Omega$.

2 Josephson junction

Brian Josephson predicted in 1962 [101] that a supercurrent at zero voltage through a thin insulator sandwiched between two superconductors takes the form

$$I = I_{\mathrm{C}} \sin(\varphi), \tag{3.9}$$

where the critical current I_{C} is the highest supercurrent that can be carried across the junction and φ is the phase across the junction. Josephson also stated that in the presence of a voltage V across the junction the phase evolves as

$$\frac{\partial \varphi}{\partial t} = \frac{2\pi}{\Phi_0} V. \tag{3.10}$$

The constant $\Phi_0 = h/2e$ is known as the magnetic flux quantum where h is the Planck's constant and e the elementary charge. Equations (3.9) and (3.10) are called Josephson relations. Inductance L is defined as

$$V = L \frac{\partial I}{\partial t}. \tag{3.11}$$

From the Josephson relations of Equations (3.9) and (3.10), $\partial I/\partial t$ obtains the form

$$\frac{\partial I}{\partial t} = \frac{2\pi I_{\mathrm{C}} \cos(\varphi)}{\Phi_0} V, \tag{3.12}$$

which together with the definition of inductance of Equation (3.11) sets the inductance of a Josephson junction to be

$$L = \frac{\Phi_0}{2\pi I_{\mathrm{C}} \cos(\varphi)}. \tag{3.13}$$

One year after Josephson relations were published, Ambegaokar and Baratoff derived a relation connecting the critical current I_{C} to the normal state resistance R_{T} of a Josephson junction [102]. This Ambegaokar-Baratoff relation reads as

$$I_{\mathrm{C}} R_{\mathrm{T}} = \frac{\pi\Delta}{2e} \tanh\left(\frac{\Delta}{2k_{\mathrm{B}}T}\right). \tag{3.14}$$

Δ is the superconducting gap, k_{B} the Boltzmann constant and T the temperature. The superconducting gap for a 20 nm thin aluminum film is $\Delta \approx 200\,\mu$eV [33, 78, 103]. The superconducting resonators in Papers III and IV were formed of aluminum and the measurements were performed at electronic temperature of $T = 50$ mK in a dilution refrigerator. These numerical values for Δ and T approximate the hyperbolic tangent in Equation (3.14) as $\tanh(\Delta/(2k_{\mathrm{B}}T)) = 1$. With this simplification, the critical current acquires the following form

$$I_{\mathrm{C}} = \frac{\pi\Delta}{2eR_{\mathrm{T}}}. \tag{3.15}$$

Zero current bias across the junction $I = 0$ fixes the phase across the junction to be $\varphi = 0$. Further $\cos(\varphi) = 1$, and together with Equation (3.15) the inductance of a Josephson junction becomes

$$L_{\mathrm{J}} = \frac{hR_{\mathrm{T}}}{2\pi^2\Delta}. \tag{3.16}$$

For a superconductor the junction inductance is solely set by the normal state resistance of the junction. Hence, designing the inductance of a Josephson junction is straightforward: the oxide thickness of a junction and the junction area are parameters that are easy to control in fabrication. $R_{\mathrm{T}} = 500\,\Omega$ and $\Delta = 200\,\mu$eV yields the junction inductance $L_{\mathrm{J}} = 0.5$ nH for Al-AlOx-Al junctions in Papers III and IV. By connecting multiple junctions in series with a spacing of $a = 1\,\mu$m, the inductance per unit length increases to $\mathcal{L} = L_{\mathrm{J}}/a = 0.5$ mH/m from the three orders of magnitude lower value for superconducting Al coplanar waveguide resonator in Section 1.

3 Double quantum dot

In this section, basics of a series-coupled semiconductor double quantum dot (DQD) is described. A DQD forms the other half of the microwave resonator-DQD device in Paper IV and is thus of importance to be discussed. In a DQD, two small nanoscale volumes called quantum dots are tunnel-coupled to each

other by a potential barrier and each dot is further coupled to its own electron reservoir by a tunnel coupling. These potential barriers allow electron transport by tunneling [104]. The dots are small in the sense that Coulomb interactions play an important role setting the relevant energy scale in transport. Due to the Coulomb repulsion between electrons there is an energy cost to add an electron to a dot. The other effect contributing to the energy spectrum of a dot is quantum confinement as the three tunnel barriers confine electrons to two small volumes. Both Coulomb effect and quantum confinement are introduced in this section and the discussion follows Ref. 105.

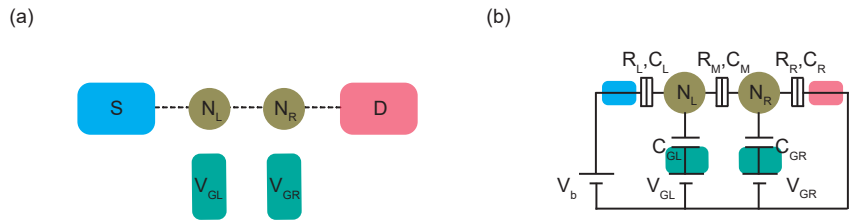

Figure 3.2: (a), A schematic drawing of a DQD. Source (S) and drain (D) are tunnel-coupled to two quantum dots with electron numbers $N_{\rm L}$ and $N_{\rm R}$. These electron numbers are controlled by gate voltages $V_{\rm GL}$ and $V_{\rm GR}$. (b), An equivalent circuit of the DQD in panel (b). A tunnel barrier is modelled by parallel resistance and capacitance, for example $R_{\rm L}$ and $C_{\rm L}$ for the barrier between the source and the left dot. The gate voltages are coupled to the dots via the capacitances $C_{\rm GL}$ and $C_{\rm GR}$. The bias voltage $V_{\rm b}$ sets a difference in chemical potentials between the source and the drain.

Each quantum dot contains a well-defined number of electrons, $N_{\rm L(R)}$ in the left (right) dot. The left dot is connected to the source lead (S) and the right dot to the drain lead (D). This is illustrated by a schematic drawing in Fig. 3.2 (a) where electrons are allowed to enter the dots along the dashed black lines. The electron numbers are controlled by the left and the right gate voltages $V_{\rm GL}$ and $V_{\rm GR}$, respectively, which change the chemical potentials of the dots but no transport takes place via the gate lines. Figure 3.2 (b) shows an equivalent circuit of the DQD. The tunnel barrier between the source and the left dot is modelled by parallel resistance $R_{\rm L}$ and capacitance $C_{\rm L}$. The other two tunnel barriers are modelled in the same way. The resistances $R_{\rm L}$, $R_{\rm M}$ and $R_{\rm R}$ all need to be larger than the resistance quantum $R_{\rm K} \equiv h/e^2$ in order to have localized electron wave functions on the quantum dots [106]. $V_{\rm b}$ is the bias voltage applied to the source contact while keeping the drain grounded setting a preferred direction for electron transport between the leads.

Here, the bias is kept at $V_{\rm b} \approx 0$ and thus the DQD is studied in linear transport regime. We neglect cross capacitances i.e. capacitance between the left (right) gate and the right (left) dot. Then the electrostatic energy of the DQD can be written as

$$
\begin{aligned}
U(N_{\mathrm{L}}, N_{\mathrm{R}}) &= \frac{1}{2}N_{\mathrm{L}}^2 E_{\mathrm{CL}} + \frac{1}{2}N_{\mathrm{R}}^2 E_{\mathrm{CR}} + N_{\mathrm{L}}N_{\mathrm{R}}E_{\mathrm{CM}} + f(V_{\mathrm{GL}}, V_{\mathrm{GR}}) \\
f(V_{\mathrm{GL}}, V_{\mathrm{GR}}) &= \frac{1}{-e}[C_{\mathrm{GL}}V_{\mathrm{GL}}(N_{\mathrm{L}}E_{\mathrm{CL}} + N_{\mathrm{R}}E_{\mathrm{CM}}) + C_{\mathrm{GR}}V_{\mathrm{GR}}(N_{\mathrm{L}}E_{\mathrm{CM}} + N_{\mathrm{R}}E_{\mathrm{CR}})] \\
&\quad + \frac{1}{e^2}\left(\frac{1}{2}C_{\mathrm{GL}}^2 V_{\mathrm{GL}}^2 E_{\mathrm{CL}} + \frac{1}{2}C_{\mathrm{GR}}^2 V_{\mathrm{GR}}^2 E_{\mathrm{CR}} + C_{\mathrm{GL}}V_{\mathrm{GL}}C_{\mathrm{GR}}V_{\mathrm{GR}}E_{\mathrm{CM}}\right),
\end{aligned}
\tag{3.17}
$$

where $E_{\mathrm{CL(R)}}$ is the charging energy of the left (right) dot, E_{CM} is the coupling energy and e is the elementary charge. E_{CM} is the energy change of one dot when the other dot receives an electron. The charging energies and the coupling energy read as

$$
\begin{aligned}
E_{\mathrm{CL(R)}} &= \frac{e^2}{C_{\mathrm{QDL(R)}}}\left(\frac{1}{1 - \frac{C_{\mathrm{M}}^2}{C_{\mathrm{QDL}}C_{\mathrm{QDR}}}}\right) \\
E_{\mathrm{CM}} &= \frac{e^2}{C_{\mathrm{M}}}\left(\frac{1}{\frac{C_{\mathrm{QDL}}C_{\mathrm{QDR}}}{C_{\mathrm{M}}^2} - 1}\right),
\end{aligned}
\tag{3.18}
$$

where $C_{\mathrm{QDL}} = C_{\mathrm{L}} + C_{\mathrm{GL}} + C_{\mathrm{M}}$ is the sum of capacitances to the left dot. C_{QDR} for the right dot is calculated in the same way. The chemical potential $\mu_{\mathrm{L(R)}}$ of the left (right) dot is defined as the energy required to add the $N_{\mathrm{L(R)}}$th electron, while the right (left) dot hosts $N_{\mathrm{R(L)}}$ electrons. The electrostatic energy in Equation (3.17) yield the chemical potentials as

$$
\begin{aligned}
\mu_{\mathrm{L}}(N_{\mathrm{L}}, N_{\mathrm{R}}) &= U(N_{\mathrm{L}}, N_{\mathrm{R}}) - U(N_{\mathrm{L}} - 1, N_{\mathrm{R}}) \\
&= \left(N_{\mathrm{L}} - \frac{1}{2}\right)E_{\mathrm{CL}} + N_{\mathrm{R}}E_{\mathrm{CM}} - \frac{1}{e}(C_{\mathrm{GL}}V_{\mathrm{GL}}E_{\mathrm{CL}} + C_{\mathrm{GR}}V_{\mathrm{GR}}E_{\mathrm{CM}}) \\
\mu_{\mathrm{R}}(N_{\mathrm{L}}, N_{\mathrm{R}}) &= U(N_{\mathrm{L}}, N_{\mathrm{R}}) - U(N_{\mathrm{L}}, N_{\mathrm{R}} - 1) \\
&= \left(N_{\mathrm{R}} - \frac{1}{2}\right)E_{\mathrm{CR}} + N_{\mathrm{L}}E_{\mathrm{CM}} - \frac{1}{e}(C_{\mathrm{GL}}V_{\mathrm{GL}}E_{\mathrm{CM}} + C_{\mathrm{GR}}V_{\mathrm{GR}}E_{\mathrm{CR}}).
\end{aligned}
\tag{3.19}
$$

The chemical potential of the left dot changes by $\mu_{\mathrm{L}}(N_{\mathrm{L}}+1, N_{\mathrm{R}})-\mu_{\mathrm{L}}(N_{\mathrm{L}}, N_{\mathrm{R}}) = E_{\mathrm{CL}}$ when an electron is added to the dot. This change in energy is equal to the charging energy of the left dot and called addition energy of the left dot.

The quantum dot energy spectrum presented so far has been based on Coulomb interaction. Electrons in the dots are confined by the potential barriers leading to quantized energy states. The quantum confinement can be incorporated in the chemical potential. Here, the constant interaction model [107] is assumed meaning that the single-particle energies ϵ_i can be summed with the chemical potentials in Equation (3.19) to give for the left dot $\mu_{\mathrm{L},i} = \mu_{\mathrm{L}} + \epsilon_i$. Thus, the addition energy becomes

$$E_{\mathrm{add,L}} = \mu_{\mathrm{L},i}(N_{\mathrm{L}}+1, N_{\mathrm{R}}) - \mu_{\mathrm{L},j}(N_{\mathrm{L}}, N_{\mathrm{R}}) = E_{\mathrm{CL}} + (\epsilon_i - \epsilon_j), \tag{3.20}$$

and similarly for the right dot.

The chemical potentials of the quantum dots define stable regions of the quantum dot electrons numbers in (V_{GL}, V_{GR})-graph illustrated in Fig. 3.3. These plots are known as charge stability diagrams. The regions with constant electron numbers take different shapes depending on the interdot capacitance C_{M}. In panel (a) $C_{\mathrm{M}} = 0$ and change in one gate voltage while keeping the other gate voltage fixed only affects the electron number on one of the dots. In this regime, the two dots are completely decoupled. The other extreme is presented in panel (b) where $C_{\mathrm{M}}/C_{\mathrm{QDL(R)}} = 1$ and charge states are separated by diagonal lines. In this limit, C_{M} is the dominant capacitance and the two quantum dots behave as a combined single quantum dot with electron number $N_{\mathrm{L}} + N_{\mathrm{R}}$.

Panel (c) shows the intermediate case where the tunnel barrier between the two dots is sufficiently transparent to enable transport between the dots but opaque enough to keep the two dots as separate entities both having a well-defined electron number. An example of an interdot transition line is pointed out in panel (c) by label (g). The two other types of transition lines are marked by (e) and (f). The panels (e)-(g) illustrate the chemical potentials in the leads and the dots at the three transition lines marked in panel (c). In panels (e) and (f) an electron is shuttled between one of the dots and lead whereas in (g) an electron tunnels between the two dots. Panel (d) is an example of a measurement for a DQD charge stability diagram corresponding to the case (c).

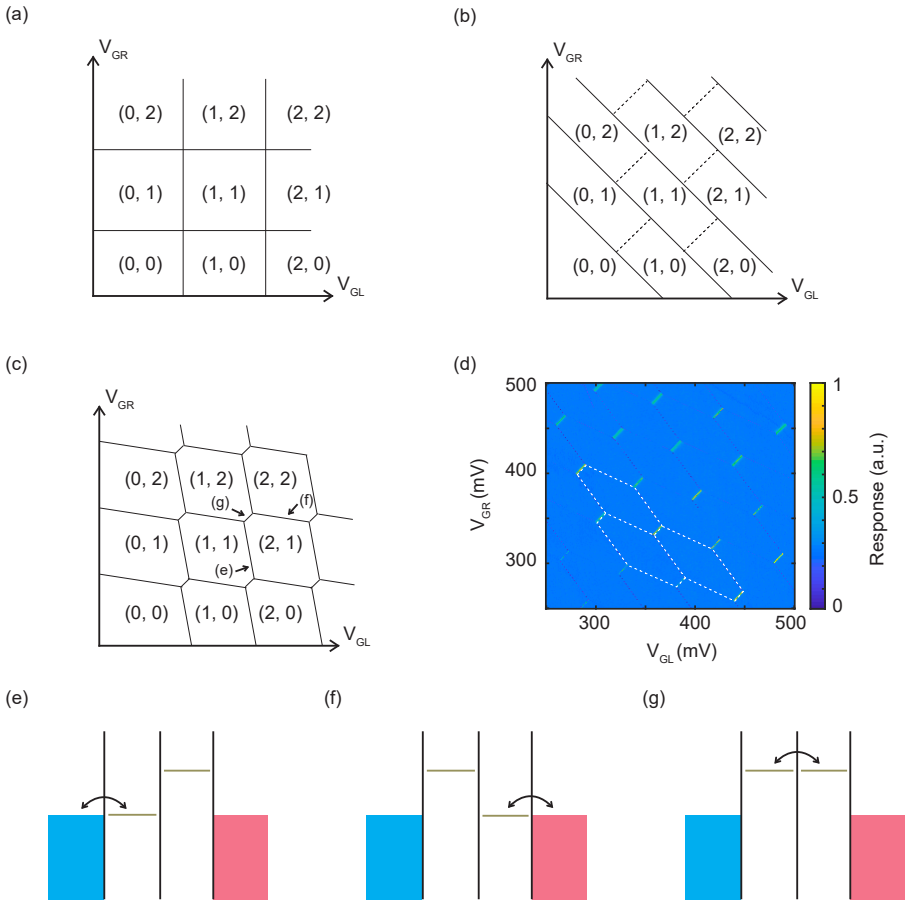

Figure 3.3: (a), Charge stability diagram of a DQD at zero interdot coupling $C_{\mathrm{M}} = 0$. (b), The oher extreme where C_{M} is the dominant capacitance and the two quantum dots behave as a single dot. (c) The intermediate regime between (a) and (b). The charge transitions across the lines are illustrated in panels (e)-(g). (d) Experimentally determined stability diagram corresponding (c). (e) Transition between the left lead and the left dot. (f) Between the right lead and the right dot. (g) Between the two dots.

4 Device fabrication

In this section, a detailed description for fabrication of the Josephson junction array resonator - semiconductor double quantum dot device in Paper IV is given. The Josephson junction array resonators in Paper III were fabricated in the same manner with the exception that no nanowires were incorporated. To electrically characterize the hybrid system in Paper IV, electrical contacts to the system need to be placed on a wafer. By electron-beam lithography (EBL) [108] and metal evaporation [109], Ti/Au markers and pads were defined

on the wafer. Markers establish local coordinate systems on the wafer surface and are used to place structures in later fabrication steps. Pads provide a galvanic interface to connect Nb and Al lines. Patterns for the electrical lines and the surrounding ground plane were exposed by optical lithography [110] and the structures were formed by sputtered Nb [109]. Then the DC lines were covered by atomic layer deposition grown aluminium oxide and evaporated Al. This increases the capacitance of the lines to reduce photon losses from the resonator in the measurements. Nanowires were mechanically deposited by a micromanipulator on designated areas marked by Ti/Au crosses defined in the first fabrication round. The electrostatic gates and the source and drain contacts for a nanowire were implemented by EBL and metal evaporation. As the last step, two-angle shadow-evaporation technique with an intermediate in-situ oxidation was employed to construct the Josephson junction array resonator.

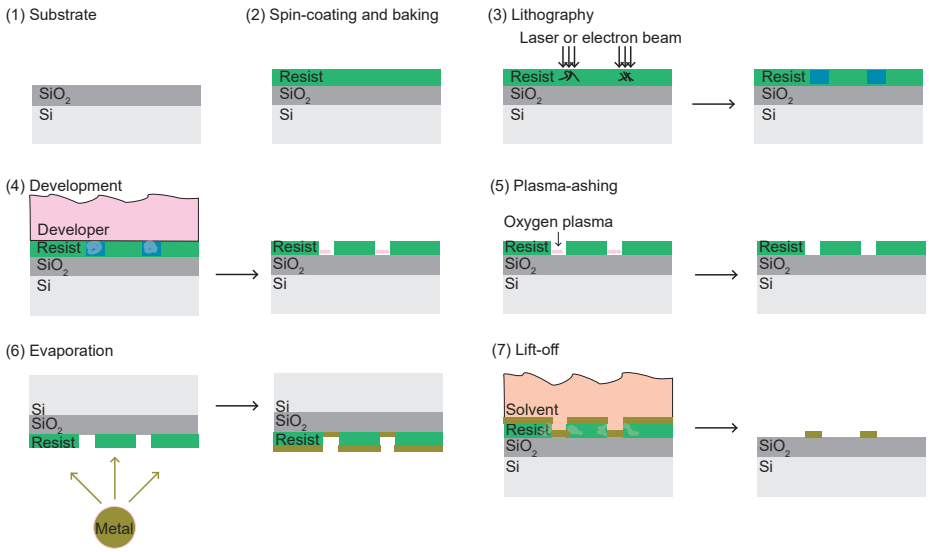

Figure 3.4: A process flow showing steps to fabricate metallic structures on a wafer by lithography and metal evaporation.

4.1 Electrical lines and ground planes

The device is fabricated on a 2" high-resistivity intrinsic silicon wafer coated by 200 nm thick thermally grown SiO_2. The insulating oxide layer enables transport measurements for the DQD as no transport can take place via the substrate. The wafer is cleaned in acetone and isopropanol (IPA). In the first lithography round Ti/Au markers, see Fig. 3.5 (b), are defined to place structures in later fabrication steps. Figure 3.4 presents a process flow containing Steps (1)-(7)

on how metal structures are created on the wafer by lithographic and metal evaporation methods.

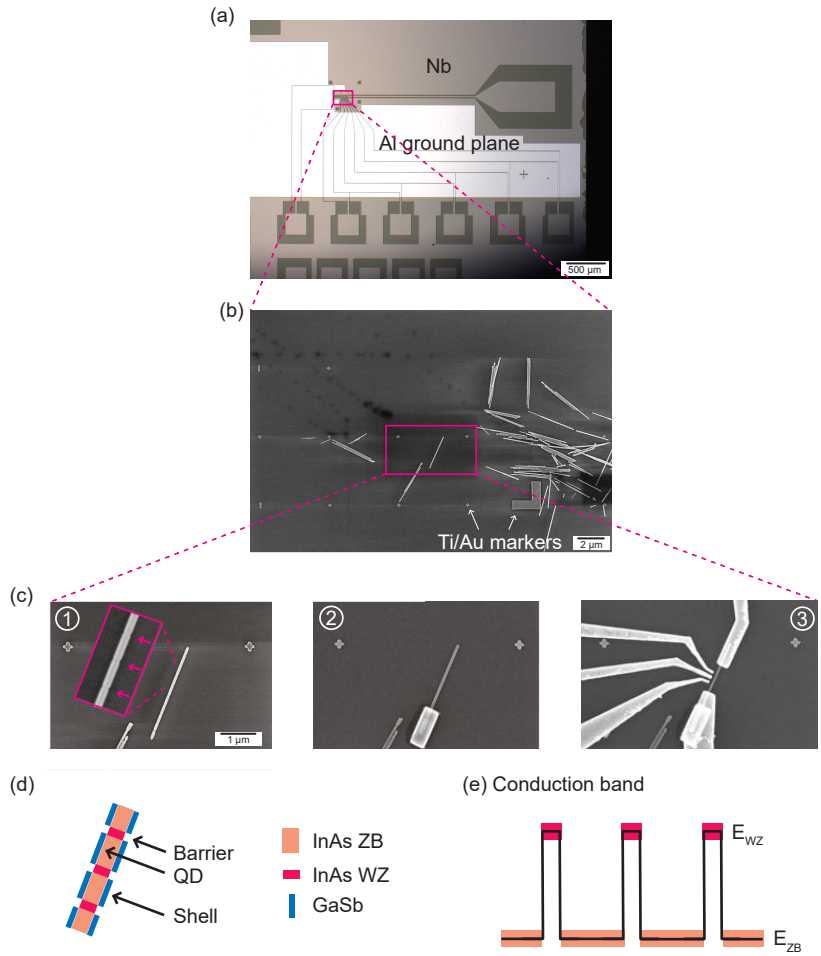

Figure 3.5: (a), An optical image showing the electrical lines and the surrounding ground plane made of sputtered Nb. An additional ground plane made of Al on top of the DC lines. (b), Nanowires deposited on a chip area where Ti/Au markers define a local coordinate system. (c), Three panels showing fabrication steps in making gate electrodes and source-drain contacts. (d), Schematics of polytype InAs nanowire where wurzite barriers confine electrons on zincblende quantum dots. GaSb shell is selectively grown on zincblende dots. (e), Nanowire conduction band where wurzite segments form barriers due to conduction band offset between the two crystal phases.

First, the Ti/Au markers and pads are defined on the wafer. The wafer is spin-coated by polymethyl methacrylate (PMMA) and baked on a hotplate to form a solid resist layer in Step (2). In EBL Step (3), selected areas of this resist are exposed by electrons accelerated to 50 kV. When electrons collide with PMMA molecules they modify the chemical composition of the resist making the exposed resist to dissolve in MIBK:IPA 1:3 solution in Step (4) known as development.

After the development some resist residues still remain on the wafer surface. These remains are cleaned off by oxygen plasma turning the residues into ash in Step (5). Then 5 nm thick Ti layer is electron-beam evaporated on the wafer in Step (6) followed by evaporation of 45 nm thick Au layer. The thin Ti film ensures good adhesion of Au as Au does not stick well directly on SiO_2. At this point, the evaporated metal film covers the wafer completely. The unexposed resist and metal layers on top of the resist are removed by acetone solvent in Step (7). The metal structures defined by the EBL pattern remain on the wafer surface.

The smallest structures defined in the first lithography round are 100 nm wide and require the resolution of EBL. Next, patterns for electrical lines and a ground plane are exposed by direct-write laser optical lithography. These structures are of micrometer-scale and hence suitable for laser writer which is faster than EBL but provides poorer resolution. The optical lithography follows the same process flow as EBL. The only differences are the chemicals used: the resist is S1813, the developer MF319 and the solvent Remover 1165. Furthermore, in Step (3) the resist is exposed by 405 nm wavelength laser and Nb is sputtered on the wafer instead of metal evaporation in Step (6).

A large ground plane pattern is exposed by optical lithography on a resist stack consisting of an LOR3A layer at bottom and a S1813 layer on top. An undercut forms in the bottom LOR3A layer on the resist stack when developed. After plasma-ashing 30 nm of aluminum oxide is grown by atomic layer deposition followed by 50 nm of electron-beam evaporated Al. The undercut provided by LOR3A makes it easier to do a lift-off for an oxide coated wafer. The Nb structures and Al ground plane above Nb lines are visible in Fig. 3.5 (a).

4.2 Nanowire contacts

With the electrical lines and ground planes formed, it remains to deposit nanowires, fabricate nanowire contacts and resonators. The wafer is diced into smaller chips in order not to waste the entire wafer in case of an issue in the remaining processing steps. Nanowires are mechanically deposited by a micromanipulator on a chip area which has a local coordinate system defined by Ti/Au markers processed in the first lithography step. The micromanipulator has a sharp In needle. The needle is manually moved to collect nanowires from a growth chip containing a wealth of nanowires. By then placing the needle above the area with a local coordinate system and sweeping the needle on the chip surface deposits nanowires. The chip is then rinsed in IPA to remove mobile nanowires. Nanowires still attached to the chip surface after the rinsing are seen in Fig. 3.5

(b).

One of the nanowires is chosen to be processed further and a zoom-in of it is shown in Fig. 3.5 (c) panel ①. In the crystal-phase defined InAs nanowire short wurzite segments confine electrons in zincblende parts due to conduction band offset between the crystal phases [111, 112, 113]. A GaSb shell is selectively grown on zincblende. The inset in panel ① shows a zoom-in where the wurzite barriers are indicated by the arrows and the GaSb shell on the zincblende parts are clearly visible. With the help of the Ti/Au markers, coordinates for three wurzite barriers defining two quantum dots are found. Schematics of the nanowire is shown in Fig. 3.5 (d) and the conduction band of the nanowire in (e).

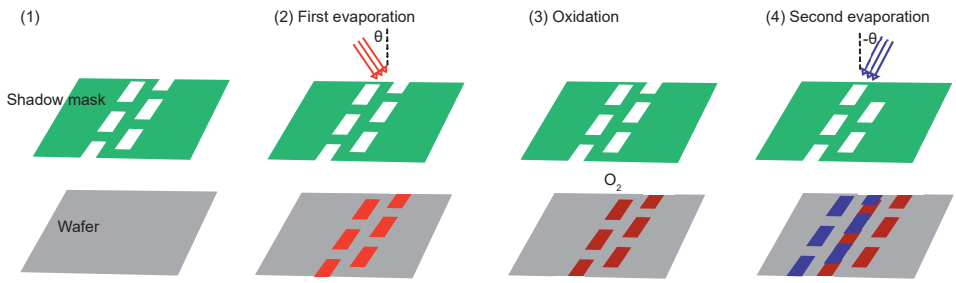

Figure 3.6: Schematics of two-angle shadow-evaporation. (1), Shadow mask. (2), First Al evaporation at an angle θ. (3), In-situ oxidation of Al evaporated in (2). (4), Second Al evaporation at an angle $-\theta$.

The Ni/Au patch in Fig. 3.5 (c) panel ② is formed by EBL and metal evaporation to clamp the nanowire to its position keeping it immobile during wet-etching of the GaSb shell. To etch the shell first the chip is spin-coated with one layer of PMMA, baked and a rectangle enclosing the nanowire is exposed by EBL, developed and plasma-ashed with oxygen. Now the nanowire is not covered by the resist and by submerging the chip in MF319 the GaSb shell is removed. The chip is then cleaned with deionized water followed by IPA and second PMMA layer is spin-coated and baked. Now PMMA covers the nanowire again and pattern for gate lines and source-drain contacts is exposed, developed and plasma-ashed. Native oxide on the nanowire is removed by buffered oxide etch (BOE) to ensure Ohmic source and drain contacts. Electron-beam evaporated 30 nm of Ni followed by 140 nm of Au form the source and drain contacts and the three gate lines in Fig. 3.5 (c) panel ③.

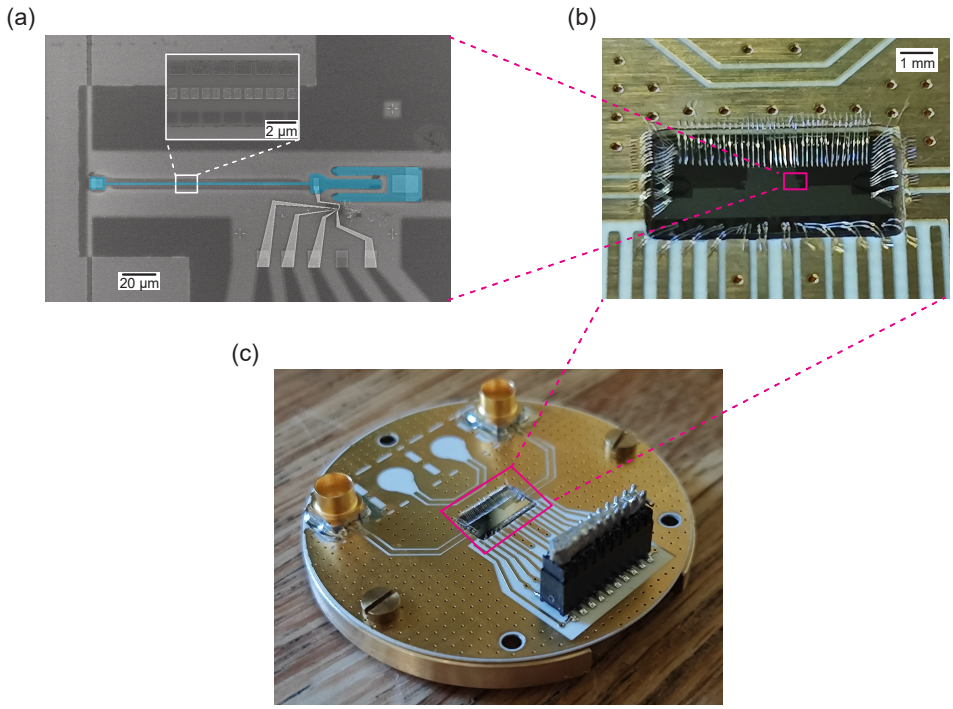

Figure 3.7: (a), A scanning electron micrograph of the shadow-evaporated Al structures highlighted in blue. The inset shows a zoom-in of the Josephson junction array. (b), The chip containing the device in (a) wire-bonded to a PCB. (c), The chip and the PCB connected to a brass piece.

4.3 Josephson junction array

The Josephson junction array and coupler fabrication follow the process flow in Fig. 3.4. To form junctions a two-angle shadow-evaporation technique is employed instead of evaporating at the right angle to the chip surface as done in earlier evaporations. The chip is coated by three layers of MMA (EL9) MAA copolymer with the total thickness of $\sim 1\,\mu$m and one layer of 300 nm thick PMMA. MMA provides undercut and PMMA functions as an overhanging bridge providing a shadow mask in Fig. 3.6 Step (1). This shadow mask pattern is exposed by EBL with 20 kV acceleration voltage which is lower than 50 kV used in the EBL exposures earlier. The lowered acceleration voltage provides more undercut which is important for shadow-evaporation. First, a 30 nm thick Al layer is evaporated at $\theta = 40\,^\circ$ resulting in disconnected Al pieces in Step (2). Then, in Step (3) oxygen is let inside the sample space of the evaporator. In 2 min the pressure is ramped up to 0.36 mbar from the evaporator vacuum level of 10^{-6}mbar and then kept constant for 4.5 min. During this time a thin few nanometers thick insulating aluminum oxide layer forms on the Al film. Oxygen

is then pumped out of the sample space. By evaporating at $\theta = -40\,^\circ$ a 70 nm thick Al film is formed contacting the already existing Al pieces and forming a continuous array of junctions where the junctions are located at the interfaces between the two Al layers separated by aluminum oxide. Capacitive coupler to an RF line and a galvanic contact to a DC line are formed alongside the junction array. The shadow-evaporated Al structures are highlighted by blue in a scanning electron micrograph in Fig. 3.7 (a). The inset shows a zoom-in of the junction array.

Finally, the chip is diced into smaller chips each of which contains two complete devices. One of these chips is then glued by vacuum grease to a brass piece and wire-bonded to a printed circuit board (PCB) in Fig. 3.7 (b). Figure 3.7 (c) shows the PCB connected to the brass piece which is then mounted to a bottom-loader of a dilution refrigerator to measure the device.

5 Josephson junction array resonator (Paper III)

Paper III studies experimentally two Josephson junction array resonators probed in a transmission line geometry. As shown in Section 2, Josephson junctions increase the inductance of the line. This yields a characteristic impedance $Z_\mathrm{r} \sim 1\,\mathrm{k}\Omega$ more than an order of magnitude larger than a standard $50\,\Omega$ coplanar microwave resonator [114, 45, 44]. The two resonators were fabricated in the same processing round and the Josephson junction arrays are nominally equal with the same total length, junction resistance and spacing. However, the two resonators differ by their coupling strength to the RF input/output lines as the coupler geometries are dissimilar. The paper shows that increasing the coupling capacitance from one resonator to the other considerably shifts the resonance frequency towards lower frequencies. Also, a maximum value limiting these couplings is derived by means of a circuit analysis.

The resonators in Paper III were fabricated following the process flow described in Section 4. First, Ti/Au markers and pads were defined by EBL and e-beam evaporated on a high-resistivity intrinsic silicon wafer with a 200 nm thick thermal silicon oxide coating. Second, a 100 nm thick Nb film was sputtered to form the RF input/output lines and the surrounding ground plane. Finally, the Josephson junction arrays were fabricated by a standard two-angle shadow-evaporation technique. 30 nm thick Al layer was e-beam evaporated at $\theta = 20\,^\circ$ to the normal of the substrate followed by an in-situ oxidation and evaporation of 60 nm thick Al layer at $\theta = -20\,^\circ$ to form a continuous array of junctions. Optical micrographs in Fig. 3.8 present the devices. In Fig. 3.8 (a) a thin

Josephson junction array is located between the RF input/output lines and the ground plane lies above and below these structures in the figure. The inset shows a scanning electron micrograph of the array. Figure 3.8 (a) shows the device with low input/output couplings. Panel (c) shows the high output coupling of the second device. For each device the input coupler is identical with the output coupler.

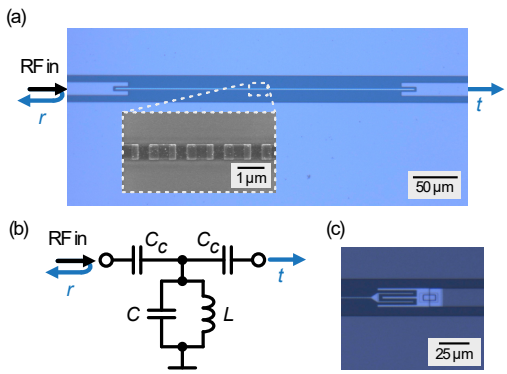

Figure 3.8: (a), An optical micrograph of a two-port Josephson junction array resonator with low input/output couplings. The RF input/output lines and the ground plane above and below them are sputtered Nb. The thin line between the input/output lines is an array of Josephson junctions formed of aluminum oxide sandwiched between two Al layers. r is the reflected amplitude of a RF signal sent in from the left port and t is the transmitted amplitude to the right port. The inset shows a zoom-in of the array. (b), An equivalent LC-circuit presentation of the resonator in (a). C_c is the capacitive coupling between the resonator and the input (output) port. The resonator has lumped-element inductance L and capacitance C. (c), An optical micrograph of the output coupler of the device with high input/output couplings. Figure is adapted from Paper III.

Both resonators consist of 231 junctions with the spacing $a = 1\,\mu$m and each junction has an inductance $L_\mathrm{J} = hR_\mathrm{T}/2\pi^2\Delta$ as derived in Section 2. The normal state resistance of a junction $R_\mathrm{T} = 500\,\Omega$ was measured at room temperature for test junctions fabricated in the same processing round and on the same chip as the resonators. These test junctions are nominally identical to the ones forming the resonators in Fig. 3.8. R_T, a and the superconducting gap $\Delta = 200\,\mu$eV for thin film Al [33, 78, 103] used as the resonator material yield the resonator inductance per unit length $\mathcal{L} = L_\mathrm{J}/a = 0.5\,$mH/m. $\mathcal{L}$, the capacitance per unit length $\mathcal{C}$ and the resonator length $l = 231\,\mu$m set the lumped-element inductance $L = 2\mathcal{L}l/\pi^2$ and capacitance $C = \mathcal{C}l/2$ of the fundamental resonance mode in the equivalent LC-circuit in Fig. 3.8 (b).

The transmission coefficient $|t|^2$ and reflection $|r|^2$ response, as a function of the drive frequency ω, of the resonator with low coupling strength to $Z_0 = 50\,\Omega$ input/output lines is shown in Fig 3.9 (a). The fundamental half-wavelength resonance mode with voltage antinodes at the resonator endpoints and a voltage node in the middle has a resonance frequency of $\omega_\mathrm{r}/2\pi = 8.735\,$GHz. The Lorentzian fits denoted by the solid lines in Fig 3.9 (a) read as

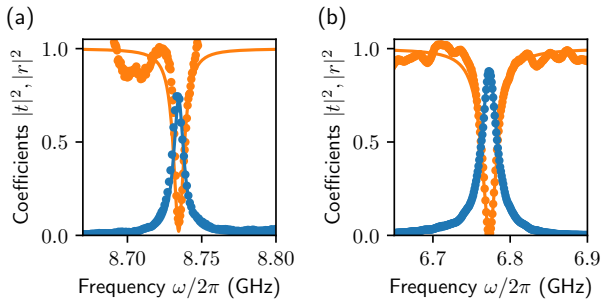

Figure 3.9: (a), The measured transmission $|t|^2$ and reflection $|r|^2$ coefficients as functions of the drive frequency ω for the device with low input coupling. The solid lines are Lorentzian fits based on Equation 3.21. (b), The same measurements as in (a) repeated for the device with high input coupling. The ingoing microwave power at the left port is $-115\,\mathrm{dBm}$. Figure adapted from Paper III.

$$\begin{cases} |t|^2 = \frac{\kappa_c^2}{(\kappa_c+\kappa_{int}/2)^2+(\omega-\omega_r)^2} \\ |r|^2 = \frac{(\kappa_{int}/2)^2+(\omega-\omega_r)^2}{(\kappa_c+\kappa_{int}/2)^2+(\omega-\omega_r)^2}, \end{cases} \tag{3.21}$$

where $\kappa_c/2\pi = 3.5\,\mathrm{MHz}$ is the input coupling and $\kappa_{int}/2\pi = 1.2\,\mathrm{MHz}$ is the internal losses of the resonator [44]. The circuit elements in Fig. 3.8 (b) depend on ω_r and κ_c as $\omega_r = 1/\sqrt{LC_\Sigma}$ and

$$\kappa_c = \frac{\omega_r^2 C_c^2 Z_0}{C_\Sigma}, \tag{3.22}$$

where $C_\Sigma = C + 2C_c$ is the total capacitance of the resonator [100, 115]. These relations yield the capacitance values $C_\Sigma = 14\,\mathrm{fF}$ and $C_c = 1.4\,\mathrm{fF}$ and further $\mathcal{C} = 2C/l = 80\,\mathrm{pF/m}$ in line with similar transmission line geometry on a thermally oxidized silicon substrate [100]. The characteristic impedance of the junction array is $Z_{JJ} = \sqrt{\mathcal{L}/\mathcal{C}} = 2.4\,\mathrm{k\Omega}$ by the Equation (3.8) derived in Section 1. The characteristic impedance of the resonator at the voltage antinode points where the resonator is coupled to input/output lines is $Z_r = \sqrt{L/C_\Sigma} = 1.4\,\mathrm{k\Omega}$.

These measurements were repeated for the second resonator device with high input coupling in Fig. 3.9 (b) yielding $\omega_r/2\pi = 6.773\,\mathrm{GHz}$, $\kappa_c/2\pi = 11\,\mathrm{MHz}$, $\kappa_{int}/2\pi = 1.3\,\mathrm{MHz}$, $C_\Sigma = 23\,\mathrm{fF}$, $C_c = 4.1\,\mathrm{fF}$ and $Z_r = 1.0\,\mathrm{k\Omega}$. By increasing the coupling from $\kappa_c/2\pi = 3.5\,\mathrm{MHz}$ to $11\,\mathrm{MHz}$ shifts the resonance frequency by $2\,\mathrm{GHz}$ towards lower frequencies. This shift is due to increased coupling capacitances as $2C_c$ stands for one third of the total capacitance of the device with high input coupling. The first of the two main conclusions of Paper III

is that small changes in coupler geometry can shift the resonance frequency considerably as the coupler capacitances constitute a significant proportion of the total device capacitance. This imposes restrictions on the coupler design to keep the resonance frequency of a Josephson junction array resonator in the measurement window.

The second main conclusion of Paper III states that the large ratio C_c/C_Σ limits the coupling strength to a maximum value $\kappa_{c,max}$ attainable in these devices. The maximum value is obtained by taking the limit $C_\Sigma = 2C_c$ in Equation (3.22) and using the relation $\omega_r Z_r = 1/C_\Sigma$ (from $\omega_r = 1/\sqrt{LC_\Sigma}$ and $Z_r = \sqrt{L/C_\Sigma}$) as

$$\kappa_{c,max} = \frac{Z_0}{4Z_r}\omega_r. \tag{3.23}$$

Typical parameter values for high-impedance resonators $Z_r = 1\,\mathrm{k\Omega}$ and $\omega_r/2\pi = 7\,\mathrm{GHz}$ [61, 60] yield $\kappa_{c,max}/2\pi = 90\,\mathrm{MHz}$.

6 Light-matter interaction

Study of light-matter interaction explores the interplay between electromagnetic radiation, commonly referred to as light, and particles that compose matter. This interaction is at the core of multitude of applications, ranging from the operation of lasers [116] to the development of cutting-edge technologies such as quantum computing [56, 57].

Probing the interaction between light and matter reveals fundamental properties of these two systems itself. For example in 1905 Einstein proposed that light must consist of tiny packets of energy (photons) in order to explain the photoelectric effect in which electrons are removed from material surface under illumination [117].

Photoelectric effect is an example of one of the most fundamental processes in light-matter interaction known as absorption. When a photon with energy matching the energy difference between two electron energy states is incident upon matter, it can be absorbed, causing an electron to transition from a lower energy level to a higher one.

In the time-reversal process of absorption where an electron relaxes from a higher energy state to a lower one, a photon equipped with energy equal to the energy difference of the states is emitted. This emission process is the basis for numerous technologies, including quantum dots used in displays [118].

This interaction can be probed in solid state for example by coupling semiconductor quantum dots, sometimes referred to as artificial atoms, with superconducting microwave resonators. These hybrid systems are in focus in Paper IV. Photons in superconducting microwave resonator can be coupled to electric dipole moment of a DQD. The quantity g describes the strength of this interaction. In Ref. 119 this coupling is derived to be

$$g = \omega_{\mathrm{r}} \nu \sqrt{\frac{2Z_{\mathrm{r}}}{R_{\mathrm{K}}}} \frac{t}{E_{\mathrm{DQD}}}, \tag{3.24}$$

where ω_{r} is the resonator resonance frequency, ν is dimensionless capacitive coupling factor between DQD and resonator, t is the interdot tunnel coupling, $E_{\mathrm{DQD}} = \sqrt{\delta^2 + (2t)^2}$ is the DQD energy gap and δ the detuning. In the strong coupling limit g exceeds the resonator losses κ and the DQD dephasing rate Γ.

Before resonator-DQD hybrid systems strong coupling was demonstrated in multitude of quantum optics systems such as alkali atoms [52], Rydberg atoms [53], superconducting qubits [36] and optically probed semiconductor single quantum dots in photoluminescence studies [54, 55]. These systems have attracted interest in the field of quantum information technology as they provide a mechanism for example, to coherently couple remote qubits [56, 57] and for transferring quantum information from qubits to photons [58, 59].

In recent years the list of systems reaching the strong coupling limit has been extended to include semiconductor DQDs addressed with microwaves [61, 43, 30, 60, 120]. In 2022 another important limit of light-matter interaction, known as ultra-strong coupling, was reached with a resonator-DQD hybrid system. Ultra-strong is not a stronger form of strong coupling but a separate quantity. In ultra-strong limit the coupling between resonator and DQD becomes a significant factor of the bare energies of the system characterized by the ratio g/ω_{r}. Traditionally, system is said to be ultra-strongly coupled if this ratio exceeds 0.1.

7 Resonator - double quantum dot coupling (Paper IV)

Paper IV continues high-impedance resonator studies started in Paper III by coupling a high-impedance resonator to a semiconductor DQD to probe light-matter interaction discussed in Section 6. Paper IV is built on two main results.

First, strong coupling limit was reached between a semiconductor DQD charge qubit and a high-impedance resonator. Second, it was shown that the dephasing of the charge qubit was not dominated by charge noise. The resonator design in Paper IV is inspired by Paper III and the resonator consists of a Josephson junction array with the same junction geometry, spacing and junction resistance as the two devices in Paper III discussed in Section 5. However, the resonator in Paper IV has a quarter-wavelength ($\lambda/4$) fundamental resonance mode instead of half-wavelength as in Paper III. This enables connecting the $\lambda/4$ resonator end point with voltage node to a DC line in order to apply bias voltage across the DQD. Fabrication of the device in Paper IV is described in detail in Section 4.

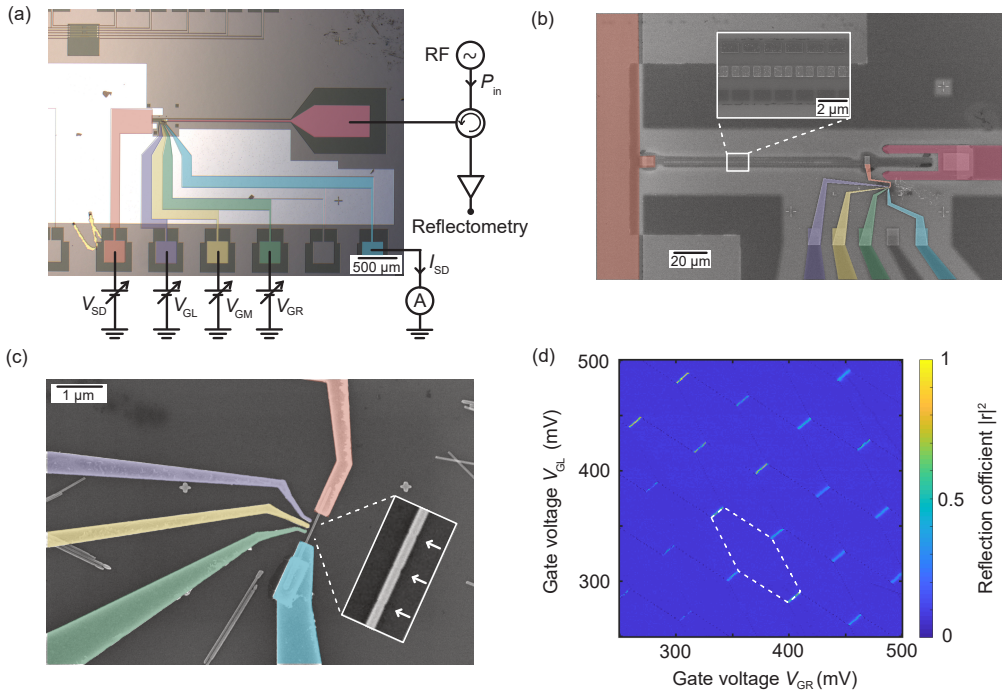

Figure 3.10: (a), An optical micrograph of the resonator-DQD device. The DC lines and the RF line probing the hybrid system are coloured. The lines and the in-plane ground plane are made out of sputtered Nb. An additional bright grey Al ground plane on top of the DC lines increases the line capacitance. The voltages V_{GL}, V_{GM} and V_{GR} tune the interdot barrier transparency and move the chemical potentials of the quantum dots. (b), A scanning electron micrograph of the area in (a) where the coloured lines meet. A quarter-wavelength Josephson junction array resonator is capacitively coupled to a microwave feedline line (in red) at a voltage antinode point and galvanically connected to a DC line (large orange contact) at a voltage node point. The inset shows a zoom-in of a few junctions. (c), A scanning electron micrograph of the nanowire DQD contacts. The inset shows a zoom-in the DQD before any contact processing steps and the three barriers are indicated by the white arrows. (d), The measured reflection coefficient $|r|^2$ response of the hybrid system as a function of the DQD gate voltages V_{GL} and V_{GR}. One DQD charge state is enclosed by the white dashed lines. Figure is adapted from Paper IV.

Figure 3.10 presents the device. The gate voltages V_{GL} and V_{GR} in Fig. 3.10 (a) control the electron numbers of the quantum dots, whereas V_{GM} tunes the

interdot tunnel barrier transparency. The DQD is galvanically coupled to a one-port resonator at the voltage antinode on the right side of Fig. 3.10 (b) via the thin orange strip. At same antinode point the one-port resonator is capacitively coupled to a microwave feedline (in red) to probe the hybrid system by RF reflectometry. The nanowire is shown in Fig. 3.10 (c). The DQD is defined in a polytype InAs nanowire by zincblende dots formed between wurzite barriers. The inset displays a zoom-in of the DQD before contact fabrication and the three barriers defining the DQD are pointed out by the white arrows. The resonator has a Lorentzian response around resonance frequency $\omega_c/2\pi = 6.7\,\mathrm{GHz}$ and a linewidth $\kappa/2\pi = 30\,\mathrm{MHz}$. The linewidth is set by $\kappa = \kappa_c + \kappa_{int}$, where the coupling between the resonator and the input line $\kappa_c/2\pi = 19\,\mathrm{MHz}$ and the resonator internal losses $\kappa_{int}/2\pi = 11\,\mathrm{MHz}$.

The measured reflection coefficient $|r|^2$ of the hybrid system as a function of the DQD gate voltages V_{GL} and V_{GR} is shown in Fig. 3.10 (d). Here, $V_{GM} = 250\,\mathrm{mV}$ was kept constant. The white dashed hexagon indicates a boundary of a fixed DQD charge state. The bright diagonal lines are so-called interdot transition lines. When crossing one these lines an electron is shuttled from one dot to the other. The electric field of the resonator couples to the dipole moment of the DQD which becomes large at the DQD charge degeneracy points, where an electron can tunnel between the left and the right quantum dot. The reflection coefficient reaches almost total reflection $|r|^2 = 1$ at these lines as the resonator frequency is shifted by much more than κ by the interaction with the DQD. The coupling strength g between the resonator and the DQD is not the same for all interdot lines but depends on the charge configuration of the DQD in a non-trivial way as the many-electron wavefunction affects the interdot tunnel coupling t.

The strong coupling limit was investigated at two different operation points. The cavity and qubit frequencies were either matched at zero (sweet spot) or finite DQD detuning δ. δ is the difference between the left and the right quantum dot energy levels. Together δ and t set the excitation energy of the DQD, $E_{DQD} = \sqrt{\delta^2 + (2t)^2}$. The qubit frequency reads as $\omega_q = E_{DQD}/\hbar$. In the measurements several maps like the one in Fig. 3.10 (d) were recorded at varying V_{GM}. Few of the brightest lines in the maps were studied to find transitions with maximum coupling between the resonator and the DQD.

Measurements at the first operation point are shown in Fig. 3.11. Fig. 3.11 (a) shows an interdot line recorded as in Fig. 3.10 (d) at $V_{GM} = 150\,\mathrm{mV}$. Figure 3.11 (b) shows a scan across the interdot line where the drive frequency ω was varied and the gate voltages V_{GL} and V_{GR} were swept along the δ axis indicated in panel (a). In the far-detuned case only the resonance of the bare cavity is visible as

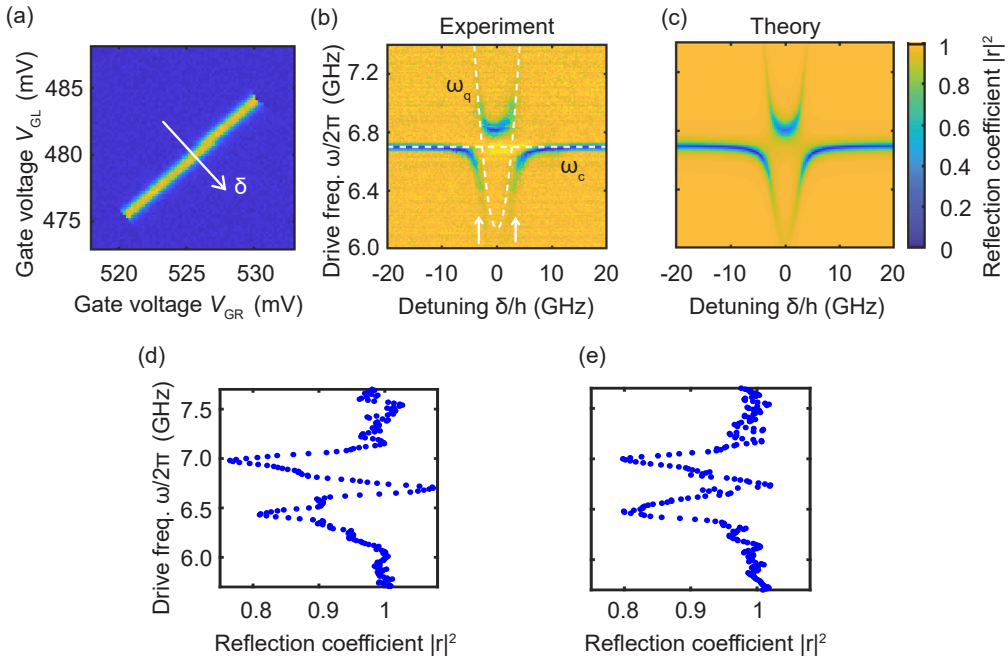

Figure 3.11: (a), An interdot transition line recorded at $V_{\mathrm{GM}} = 150\,\mathrm{mV}$. The white arrow shows the detuning δ axis. (b), $|r|^2$ measured as a function of the drive frequency ω and the detuning δ. The white dashed lines indicate the qubit ω_{q} and the cavity ω_{c} frequencies. The white arrows denote the two resonant points $\omega_{\mathrm{q}} = \omega_{\mathrm{c}}$ at finite $|\delta|$. (c), The theoretical model in Equations (3.26) and (3.25) fitted to the measurement data in (b). (d) and (e), Vertical linecuts at the left and the right resonant point denoted by white arrows in (b). Figure adapted from Paper IV.

ω_{q} greatly exceeds ω_{c} and the two systems do not interact. Towards smaller $|\delta|$ the ω_{q} becomes comparable to ω_{c} and the interaction between the resonator and the DQD results in the photonic and electronic states to hybridize. At the two finite detuning points marked by the white arrows $\omega_{\mathrm{q}} = \omega_{\mathrm{c}}$, avoiding crossings emerge around the points. Figures 3.11 (d) and (e) show vertical linecuts at these two points where the two hybridized states are particularly pronounced. The reflection coefficient response is modelled by input-output theory combined with Jaynes-Cummings Hamiltonian of the resonator-DQD system [44] under the assumption of small drive power analytically as

$$|r(\omega)|^2 = |1 - \kappa_{\mathrm{c}} A(\omega)|^2, \tag{3.25}$$

with

$$A(\omega) = \frac{\Gamma/2 - i(\omega - \omega_{\mathrm{q}})}{(\kappa/2 - i(\omega - \omega_{\mathrm{c}}))(\Gamma/2 - i(\omega - \omega_{\mathrm{q}})) + g^2}, \tag{3.26}$$

where Γ is the total dephasing rate of the DQD. The theory fit in Fig. 3.11 (c) to the experimental data in (d) yields $g/2\pi = 270\,\mathrm{MHz}$, $\Gamma/2\pi = 290\,\mathrm{MHz}$, $t/h = 3.1\,\mathrm{GHz}$ and the right gate lever arm $\alpha = 120\,\mathrm{MHz/GHz}$ as well as the resonant detuning points $\delta_\mathrm{r}/h = \pm 2.7\,\mathrm{GHz}$ with ω_c, κ_c and κ_int fixed to the above values. These values bring the hybrid system into the strong coupling regime as $2g/(\Gamma + \kappa/2) = 1.8 > 1$ [121]. In Figs. 3.11 (b) and (c) the right gate voltage change ΔV_GR is converted to detuning as $\delta = e\alpha\Delta V_\mathrm{GR}$.

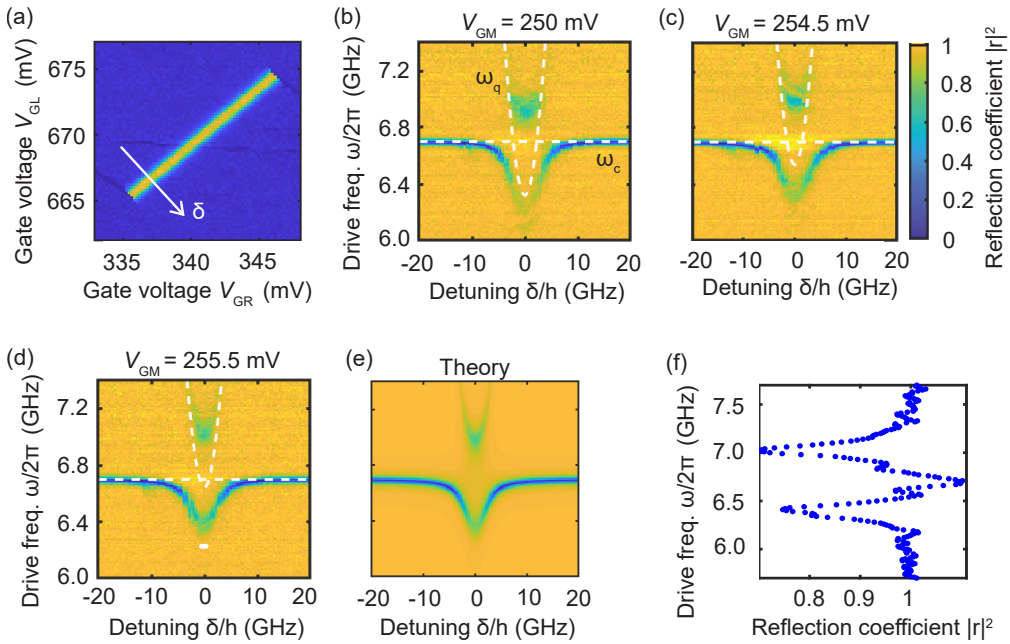

Figure 3.12: (a), An interdot transition line recorded at $V_\mathrm{GM} = 250\,\mathrm{mV}$. The white arrow shows the detuning δ axis. (b, c, d), $|r|^2$ measured as a function of the drive frequency ω and the detuning δ at $V_\mathrm{GM} = (250, 254.5, 255.5)$ mV. The white dashed lines indicate the qubit ω_q and the cavity ω_c frequencies. The white line in (d) shows the linewidth in δ direction. (e), The theoretical model in Equations (3.26) and (3.25) fitted to the measurement data in (d). (f), Vertical linecut at $\delta = 0$ in panel (d). Figure is adapted from Paper IV.

By repeating these measurements at the second operation point, results in Fig. 3.12 were obtained. In Fig. 3.12 (b) a scan was made across the interdot transition line in (a) along the δ axis. Here, $V_\mathrm{GM} = 250\,\mathrm{mV}$ which increases t and brings the DQD closer to the sweet spot. However, Fig. 3.12 (b) is still slightly off the sweet spot as the two hybridized states are located at non-equal distances from ω_c. Configurations successively closer and closer to the sweet spot are reached in Figs. 3.12 (c) and (d) by increasing V_GM. Again, a vertical linecut in Fig. 3.12 (f) recorded at $\delta = 0$ in Fig. 3.12 (d) shows two well-resolved states at equal distances from $\omega_\mathrm{c}/2\pi$. Figure 3.12 (e) shows the theory fit to

the experimental data in (d). The fit yields $g/2\pi = 320\,\mathrm{MHz}$, $\Gamma/2\pi = 260\,\mathrm{MHz}$, $t/h = 3.4\,\mathrm{GHz}$ and the right gate lever arm $\alpha = 130\,\mathrm{MHz/GHz}$.

The total dephasing rate Γ at the two operation points differ only by 10 %. This result is rather remarkable as the DQD is first-order robust against charge noise at sweet spot (Fig. 3.12) whereas the DQD was operated at a charge sensitive point in Fig. 3.11. To quantify how sensitive DQD is for detuning charge noise a quantity $s = dE_{\mathrm{DQD}}/d\delta = 1/\sqrt{1+(2t/\delta)^2}$ was defined. At the resonant finite detuning points in Fig. 3.11 (b) $s = 0.39$. At the sweet spot the fluctuations in detuning are estimated to be $\Delta\delta_{\pm}/h = \pm 0.5\,\mathrm{GHz}$ or smaller based on the linewidth in δ direction denoted by the white line in Fig. 3.12 (d). This estimate together with the fitted t yield an upper limit for the sensitivity $s = 0.08$ at the sweet spot. The sensitivity of the DQD to detuning charge noise at the sweet spot is at least five times smaller than at the investigated finite detuning values. Hence, charge noise cannot be the dominating contribution in dephasing. Figure 3.13 summarizes the measurements in Paper IV. Dephasing Γ (in red) remains constant within 10% for all investigated detuning values. The s data points at resonance (in blue) were obtained by extracting t values from the fits and then calculating δ_{r} from the resonance condition $\omega_{\mathrm{q}} = \omega_{\mathrm{c}}$. The calculated sensitivity increases towards larger δ_{r}. This in stark contrast how Γ as behaves as a function of δ_{r}. The solid blue line is $s = \delta_{\mathrm{r}}/(\hbar\omega_{\mathrm{c}})$ obtained by inserting $\omega_{\mathrm{q}} = \omega_{\mathrm{c}}$ into $s = 1/\sqrt{1+(2t/\delta_{\mathrm{r}})^2}$.

The results in Paper IV exclude charge noise as the main source of dephasing for the studied nanowire qubit. As dephasing of a charge qubit is usually credited to charge noise in the environment, work in Paper IV motivates further studies on dephasing in charge qubits e.g. how to reduce the electron-phonon coupling which in the paper is estimated to be the dominant dephasing mechanism.

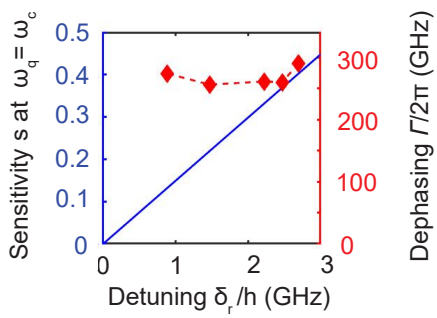

Figure 3.13: The total dephasing rate Γ and calculated sensitivity s as functions of detuning δ_{r}. The diamonds are measured data points. The solid blue line is $s = \delta_{\mathrm{r}}/(\hbar\omega_{\mathrm{c}})$ and the dashed red line is a guide to the eye. Figure is adapted from Paper IV.

Chapter 4

Summary and outlook

In Paper I splitting of Cooper pairs were identified in real time. Real-time detection is a key ingredient towards probing entanglement of electrons. To verify entanglement between electrons of a split pair the spin states of the electrons need to be probed. This can be done by energy splitting of the spin states or spin-blockade [122, 123]. Alternatively, ferromagnetic leads can be used [124, 125]. In Paper I the electrons are detected in millisecond timescale. The detection needs to be made faster than the spin lifetime and coherence time of semiconductor quantum dots. This can be achieved by available single-electron detectors in a radio-frequency circuit [126, 127]. Spin selectivity together with fast detection may enable detecting spin entanglement of split Cooper pairs.

The resonator-DQD hybrid device in Paper IV was successful in achieving the strong coupling limit of light-matter interaction. This kind of device has a potential to achieve also the ultra-strong coupling limit where the coupling g between a resonator and a DQD is a significant proportion of the bare energies of the system, namely the photon energy ω_c. Typically, this limit is considered to be achieved when $g/\omega_c \geq 0.1$. There are two obvious ways to increase g [119, 60]. One is to increase the impedance of the resonator by increasing the junction resistance. The other one is to increase the lever arm between the resonator and the DQD. In Paper IV the resonator was coupled to the source contact of the DQD. The lever arm can be increased by coupling the resonator to the one of the dots of the DQD via a so-called top gate. These top gates can be evaporated on the sacrificial GaSb shells on the dots and then wet-etch the shells. This method leaves on overhang bridge gates above the dots with a distance of around 20 nm.

References

[1] K. Shukla, P.-S. Chen, J.-R. Chen, Y.-H. Chang, and Y.-W. Liu. Macroscopic matter wave quantum tunnelling. *Communications Physics*, 3(1):101, 2020.

[2] J. P. Pekola, J. J. Vartiainen, M. Möttönen, O.-P. Saira, M. Meschke, and D. V. Averin. Hybrid single-electron transistor as a source of quantized electric current. *Nature Physics*, 4(2):120–124, 2008.

[3] H. Xin, W. J. Sim, B. Namgung, Y. Choi, B. Li, and L. P. Lee. Quantum biological tunnel junction for electron transfer imaging in live cells. *Nature Communications*, 10(1):3245, 2019.

[4] L. Esaki. New Phenomenon in Narrow Germanium $p-n$ Junctions. *Phys. Rev.*, 109(2):603–604, 1958.

[5] G. Binnig and H. Rohrer. Scanning Tunneling Microscopy. *IBM J. Res. Dev.*, 44(1–2):279–293, 2000.

[6] J. P. Pekola, O.-P. Saira, V. F. Maisi, A. Kemppinen, M. Möttönen, Y. A. Pashkin, and D. V. Averin. Single-electron current sources: Toward a refined definition of the ampere. *Rev. Mod. Phys.*, 85(4):1421–1472, 2013.

[7] J. F. Schneiderman, P. Delsing, G. Johansson, M. D. Shaw, H. M. Bozler, and P. M. Echternach. Quasiparticle poisoning in a single cooper-pair box. *AIP Conference Proceedings*, 850(1):931–932, 2006.

[8] A. F. Andreev. The thermal conductivity of the intermediate state in superconductors. *Sov. Phys. JETP*, 19(4):1228, 1964.

[9] G. Falci, D. Feinberg, and F. W. J. Hekking. Correlated tunneling into a superconductor in a multiprobe hybrid structure. *Europhysics Letters (EPL)*, 54(2):255–261, 2001.

[10] D. Beckmann, H. B. Weber, and H. V. Löhneysen. Evidence for Crossed Andreev Reflection in Superconductor-Ferromagnet Hybrid Structures. *Phys. Rev. Lett.*, 93(19):197003, 2004.

[11] L. Hofstetter, S. Csonka, J. Nygård, and C. Schönenberger. Cooper pair splitter realized in a two-quantum-dot Y-junction. *Nature*, 461(7266):960–963, 2009.

[12] L. G. Herrmann, F. Portier, P. Roche, A. Levy Yeyati, T. Kontos, and C. Strunk. Carbon Nanotubes as Cooper-Pair beam splitters. *Phys. Rev. Lett.*, 104(2):026801, 2010.

[13] J. Bardeen, L. N. Cooper, and J. R. Schrieffer. Theory of Superconductivity. *Phys. Rev.*, 108(5):1175–1204, 1957.

[14] N. Brunner, D. Cavalcanti, S. Pironio, V. Scarani, and S. Wehner. Bell nonlocality. *Rev. Mod. Phys.*, 86(2):419–478, 2014.

[15] S. Russo, M. Kroug, T. M. Klapwijk, and A. F. Morpurgo. Experimental Observation of Bias-Dependent Nonlocal Andreev Reflection. *Phys. Rev. Lett.*, 95(2):027002, 2005.

[16] A. Levy Yeyati, F. S. Bergeret, A. Martín-Rodero, and T. M. Klapwijk. Entangled Andreev pairs and collective excitations in nanoscale superconductors. *Nature Physics*, 3(7):455–459, 2007.

[17] P. Cadden-Zimansky, J. Wei, and V. Chandrasekhar. Cooper-pair-mediated coherence between two normal metals. *Nature Physics*, 5(6):393–397, 2009.

[18] J. Wei and V. Chandrasekhar. Positive noise cross-correlation in hybrid superconducting and normal-metal three-terminal devices. *Nature Physics*, 6(7):494–498, 2010.

[19] L. Hofstetter, S. Csonka, A. Baumgartner, G. Fülöp, S. d'Hollosy, J. Nygård, and C. Schönenberger. Finite-Bias Cooper Pair Splitting. *Phys. Rev. Lett.*, 107(13):136801, 2011.

[20] A. Das, Y. Ronen, M. Heiblum, D. Mahalu, A. V. Kretinin, and H. Shtrikman. High-efficiency cooper pair splitting demonstrated by two-particle conductance resonance and positive noise cross-correlation. *Nature Communications*, 3(1):1165, 2012.

[21] G. Fülöp, S. d'Hollosy, A. Baumgartner, P. Makk, V. A. Guzenko, M. H. Madsen, J. Nygård, C. Schönenberger, and S. Csonka. Local electrical

tuning of the nonlocal signals in a Cooper pair splitter. *Phys. Rev. B*, 90(23):235412, 2014.

[22] J. Schindele, A. Baumgartner, R. Maurand, M. Weiss, and C. Schönenberger. Nonlocal spectroscopy of Andreev bound states. *Phys. Rev. B*, 89(4):045422, 2014.

[23] Z. B. Tan, D. Cox, T. Nieminen, P. Lahteenmaki, D. Golubev, G. B. Lesovik, and P. J. Hakonen. Cooper Pair Splitting by Means of Graphene Quantum Dots. *Phys. Rev. Lett.*, 114(9):096602, 2015.

[24] G. Fülöp, F. Domínguez, S. d'Hollosy, A. Baumgartner, P. Makk, M. H. Madsen, V. A. Guzenko, J. Nygård, C. Schönenberger, A. Levy Yeyati, and S. Csonka. Magnetic Field Tuning and Quantum Interference in a Cooper Pair Splitter. *Phys. Rev. Lett.*, 115:227003, 2015.

[25] I. V. Borzenets, Y. Shimazaki, G. F. Jones, M. F. Craciun, S. Russo, M. Yamamoto, and S. Tarucha. High Efficiency CVD Graphene-lead (Pb) Cooper Pair Splitter. *Sci. Rep.*, 6(1):23051, 2016.

[26] J. Schindele, A. Baumgartner, and C. Schönenberger. Near-Unity Cooper Pair Splitting Efficiency. *Phys. Rev. Lett.*, 109:157002, 2012.

[27] R. S. Deacon, A. Oiwa, J. Sailer, S. Baba, Y. Kanai, K. Shibata, K. Hirakawa, and S. Tarucha. Cooper pair splitting in parallel quantum dot Josephson junctions. *Nature Commun.*, 6(1):7446, 2015.

[28] K. Ueda, S. Matsuo, H. Kamata, S. Baba, Y. Sato, Y. Takeshige, K. Li, S. Jeppesen, L. Samuelson, H. Xu, and S. Tarucha. Dominant nonlocal superconducting proximity effect due to electron-electron interaction in a ballistic double nanowire. *Science Adv.*, 5(10):eaaw2194, 2019.

[29] Z. B. Tan, A. Laitinen, N. S. Kirsanov, A. Galda, V. M. Vinokur, M. Haque, A. Savin, D. S. Golubev, G. B. Lesovik, and P. J. Hakonen. Thermoelectric current in a graphene Cooper pair splitter. *Nature Commun.*, 12:138, 2021.

[30] L. E. Bruhat, T. Cubaynes, J. J. Viennot, M. C. Dartiailh, M. M. Desjardins, A. Cottet, and T. Kontos. Circuit QED with a quantum-dot charge qubit dressed by Cooper pairs. *Phys. Rev. B*, 98:155313, 2018.

[31] P. Pandey, R. Danneau, and D. Beckmann. Ballistic Graphene Cooper Pair Splitter. *Phys. Rev. Lett.*, 126:147701, 2021.

[32] Tine Greibe, Markku P. V. Stenberg, C. M. Wilson, Thilo Bauch, Vitaly S. Shumeiko, and Per Delsing. Are "Pinholes" the Cause of Excess Current in Superconducting Tunnel Junctions? A Study of Andreev Current in Highly Resistive Junctions. *Phys. Rev. Lett.*, 106:097001, 2011.

[33] V. F. Maisi, O.-P. Saira, Yu. A. Pashkin, J. S. Tsai, D. V. Averin, and J. P. Pekola. Real-time observation of discrete andreev tunneling events. *Phys. Rev. Lett.*, 106:217003, 2011.

[34] Y. Makhlin, G. Scöhn, and A. Shnirman. Josephson-junction qubits with controlled couplings. *Nature*, 398(6725):305–307, 1999.

[35] Y. Nakamura, Yu. A. Pashkin, and J. S. Tsai. Coherent control of macroscopic quantum states in a single-Cooper-pair box. *Nature*, 398(6730):786–788, 1999.

[36] A. Wallraff, D. I. Schuster, A. Blais, L. Frunzio, R.-S. Huang, J. Majer, S. Kumar, S. M. Girvin, and R. J. Schoelkopf. Strong coupling of a single photon to a superconducting qubit using circuit quantum electrodynamics. *Nature*, 431(7005):162–167, 2004.

[37] G. Andersson, B. Suri, L. Guo, T. Aref, and P. Delsing. Non-exponential decay of a giant artificial atom. *Nature Physics*, 15(11):1123–1127, 2019.

[38] F. Arute, K. Arya, R. Babbush, D. Bacon, J. C. Bardin, R. Barends, R. Biswas, S. Boixo, F. G. S. L. Brandao, D. A. Buell, B. Burkett, Y. Chen, Z. Chen, B. Chiaro, R. Collins, W. Courtney, A. Dunsworth, E. Farhi, B. Foxen, A. Fowler, C. Gidney, M. Giustina, R. Graff, K. Guerin, S. Habegger, M. P. Harrigan, M. J. Hartmann, A. Ho, M. Hoffmann, T. Huang, T. S. Humble, S. V. Isakov, E. Jeffrey, Z. Jiang, D. Kafri, K. Kechedzhi, J. Kelly, P. V. Klimov, S. Knysh, A. Korotkov, F. Kostritsa, D. Landhuis, M. Lindmark, E. Lucero, D. Lyakh, S. Mandrà, J. R. McClean, M. McEwen, A. Megrant, X. Mi, K. Michielsen, M. Mohseni, J. Mutus, O. Naaman, M. Neeley, C. Neill, M. Y. Niu, E. Ostby, A. Petukhov, J. C. Platt, C. Quintana, E. G. Rieffel, P. Roushan, N. C. Rubin, D. Sank, K. J. Satzinger, V. Smelyanskiy, K. J. Sung, M. D. Trevithick, A. Vainsencher, B. Villalonga, T. White, Z. J. Yao, P. Yeh, A. Zalcman, H. Neven, and J. M. Martinis. Quantum supremacy using a programmable superconducting processor. *Nature*, 574(7779):505–510, 2019.

[39] P. Recher, E. V. Sukhorukov, and D. Loss. Andreev tunneling, Coulomb blockade, and resonant transport of nonlocal spin-entangled electrons. *Phys. Rev. B*, 63(16):165314, 2001.

[40] G. B. Lesovik, T. Martin, and G. Blatter. Electronic entanglement in the vicinity of a superconductor. *The European Physical Journal B - Condensed Matter and Complex Systems*, 24(3):287–290, 2001.

[41] P. Cadden-Zimansky, J. Wei, and V. Chandrasekhar. Cooper-pair-mediated coherence between two normal metals. *Nature Phys.*, 5:393, 2009.

[42] L. G. Herrmann, F. Portier, P. Roche, A. Levy Yeyati, T. Kontos, and C. Strunk. Carbon Nanotubes as Cooper-Pair Beam Splitters. *Phys. Rev. Lett.*, 104:026801, 2010.

[43] X. Mi, J. V. Cady, D. M. Zajac, P. W. Deelman, and J. R. Petta. Strong coupling of a single electron in silicon to a microwave photon. *Science*, 355(6321):156–158, 2017.

[44] Waqar Khan, Patrick P. Potts, Sebastian Lehmann, Claes Thelander, Kimberly A. Dick, Peter Samuelsson, and Ville F. Maisi. Efficient and continuous microwave photoconversion in hybrid cavity-semiconductor nanowire double quantum dot diodes. *Nature Communications*, 12:5130, 2021.

[45] P. K. Day, H. G. LeDuc, B. A. Mazin, A. Vayonakis, and J. Zmuidzinas. A broadband superconducting detector suitable for use in large arrays. *Nature*, 425(6960):817–821, 2003.

[46] B. A. Mazin, M. E. Eckart, B. Bumble, S. Golwala, P. K. Day, J. Gao, and J. Zmuidzinas. Optical/uv and x-ray microwave kinetic inductance strip detectors. *Journal of Low Temperature Physics*, 151(1):537–543, Apr 2008.

[47] G Vardulakis, S Withington, D J Goldie, and D M Glowacka. Superconducting kinetic inductance detectors for astrophysics. *Measurement Science and Technology*, 19(1):015509, 2007.

[48] A. Wallraff, D. I. Schuster, A. Blais, L. Frunzio, J. Majer, M. H. Devoret, S. M. Girvin, and R. J. Schoelkopf. Approaching unit visibility for control of a superconducting qubit with dispersive readout. *Phys. Rev. Lett.*, 95:060501, 2005.

[49] D. I. Schuster, A. Wallraff, A. Blais, L. Frunzio, R.-S. Huang, J. Majer, S. M. Girvin, and R. J. Schoelkopf. ac stark shift and dephasing of a superconducting qubit strongly coupled to a cavity field. *Phys. Rev. Lett.*, 94:123602, 2005.

[50] A. Wallraff, D. I. Schuster, A. Blais, J. M. Gambetta, J. Schreier, L. Frunzio, M. H. Devoret, S. M. Girvin, and R. J. Schoelkopf. Sideband transitions and two-tone spectroscopy of a superconducting qubit strongly coupled to an on-chip cavity. *Phys. Rev. Lett.*, 99:050501, 2007.

[51] A. Frisk Kockum, A. Miranowicz, S. De Liberato, S. Savasta, and F. Nori. Ultrastrong coupling between light and matter. *Nature Reviews Physics*, 1(1):19–40, 2019.

[52] R. J. Thompson, G. Rempe, and H. J. Kimble. Observation of normal-mode splitting for an atom in an optical cavity. *Phys. Rev. Lett.*, 68:1132–1135, 1992.

[53] M. Brune, F. Schmidt-Kaler, A. Maali, J. Dreyer, E. Hagley, J. M. Raimond, and S. Haroche. Quantum Rabi Oscillation: A Direct Test of Field Quantization in a Cavity. *Phys. Rev. Lett.*, 76:1800–1803, 1996.

[54] J. P. Reithmaier, G. Sek, A. Löffler, C. Hofmann, S. Kuhn, S. Reitzenstein, L. V. Keldysh, V. D. Kulakovskii, T. L. Reinecke, and A. Forchel. Strong coupling in a single quantum dot–semiconductor microcavity system. *Nature*, 432(7014):197–200, 2004.

[55] T. Yoshie, A. Scherer, J. Hendrickson, G. Khitrova, H. M. Gibbs, G. Rupper, C. Ell, O. B. Shchekin, and D. G. Deppe. Vacuum Rabi splitting with a single quantum dot in a photonic crystal nanocavity. *Nature*, 432(7014):200–203, 2004.

[56] J. Majer, J. M. Chow, J. M. Gambetta, J. Koch, B. R. Johnson, J. A. Schreier, L. Frunzio, D. I. Schuster, A. A. Houck, A. Wallraff, A. Blais, M. H. Devoret, S. M. Girvin, and R. J. Schoelkopf. Coupling superconducting qubits via a cavity bus. *Nature*, 449(7161):443–447, 2007.

[57] M. A. Sillanpää, J. I. Park, and R. W. Simmonds. Coherent quantum state storage and transfer between two phase qubits via a resonant cavity. *Nature*, 449(7161):438–442, 2007.

[58] A. A. Houck, D. I. Schuster, J. M. Gambetta, J. A. Schreier, B. R. Johnson, J. M. Chow, L. Frunzio, J. Majer, M. H. Devoret, S. M. Girvin, and R. J. Schoelkopf. Generating single microwave photons in a circuit. *Nature*, 449(7160):328–331, 2007.

[59] C. Eichler, C. Lang, J. M. Fink, J. Govenius, S. Filipp, and A. Wallraff. Observation of Entanglement between Itinerant Microwave Photons and a Superconducting Qubit. *Phys. Rev. Lett.*, 109:240501, 2012.

[60] P. Scarlino, J. H. Ungerer, D. J. van Woerkom, M. Mancini, P. Stano, C. Müller, A. J. Landig, J. V. Koski, C. Reichl, W. Wegscheider, T. Ihn, K. Ensslin, and A. Wallraff. In situ tuning of the electric-dipole strength of a double-dot charge qubit: Charge-noise protection and ultrastrong coupling. *Phys. Rev. X*, 12:031004, 2022.

[61] A. Stockklauser, P. Scarlino, J. V. Koski, S. Gasparinetti, C. K. Andersen, C. Reichl, W. Wegscheider, T. Ihn, K. Ensslin, and A. Wallraff. Strong coupling cavity qed with gate-defined double quantum dots enabled by a high impedance resonator. *Phys. Rev. X*, 7:011030, 2017.

[62] N. Maleeva, L. Grünhaupt, T. Klein, F. Levy-Bertrand, O. Dupre, M. Calvo, F. Valenti, P. Winkel, F. Friedrich, W. Wernsdorfer, A. V. Ustinov, H. Rotzinger, A. Monfardini, M. V. Fistul, and I. M. Pop. Circuit quantum electrodynamics of granular aluminum resonators. *Nature Communications*, 9(1):3889, 2018.

[63] L. Grünhaupt, M. Spiecker, D. Gusenkova, N. Maleeva, S. T. Skacel, I. Takmakov, F. Valenti, P. Winkel, H. Rotzinger, W. Wernsdorfer, A. V. Ustinov, and I. M. Pop. Granular aluminium as a superconducting material for high-impedance quantum circuits. *Nature Materials*, 18(8):816–819, 2019.

[64] N. Samkharadze, G. Zheng, N. Kalhor, D. Brousse, A. Sammak, U. C. Mendes, A. Blais, G. Scappucci, and L. M. K. Vandersypen. Strong spin-photon coupling in silicon. *Science*, 359(6380):1123–1127, 2018.

[65] J. H. Ungerer, A. Pally, A. Kononov, S. Lehmann, J. Ridderbos, C. Thelander, K. A. Dick, V. F. Maisi, P. Scarlino, A. Baumgartner, and C. Schönenberger. Strong coupling between a microwave photon and a singlet-triplet qubit. *arXiv:2303.16825*, 2023.

[66] A. J. Landig, J. V. Koski, P. Scarlino, U. C. Mendes, A. Blais, C. Reichl, W. Wegscheider, A. Wallraff, K. Ensslin, and T. Ihn. Coherent spin–photon coupling using a resonant exchange qubit. *Nature*, 560(7717):179–184, 2018.

[67] X. Mi, M. Benito, S. Putz, D. M. Zajac, J. M. Taylor, Guido Burkard, and J. R. Petta. A coherent spin–photon interface in silicon. *Nature*, 555(7698):599–603, 2018.

[68] N. Samkharadze, A. Bruno, P. Scarlino, G. Zheng, D. P. DiVincenzo, L. DiCarlo, and L. M. K. Vandersypen. High-kinetic-inductance superconducting nanowire resonators for circuit QED in a magnetic field. *Phys. Rev. Appl.*, 5:044004, 2016.

[69] O.-P. Saira, M. Möttönen, V. F. Maisi, and J. P. Pekola. Environmentally activated tunneling events in a hybrid single-electron box. *Phys. Rev. B*, 82(15):155443, 2010.

[70] V. F. Maisi, D. Kambly, C. Flindt, and J. P. Pekola. Full Counting Statistics of Andreev Tunneling. *Phys. Rev. Lett.*, 112(3):036801, 2014.

[71] I. M. W. Räisänen, Z. Geng, K. M. Kinnunen, and I. J. Maasilta. Normal metal - insulator - superconductor thermometers and coolers with titanium-gold bilayer as the normal metal. *Journal of Physics: Conference Series*, 969:012090, 2018.

[72] D. Dragoman and M. Dragoman. Instruments/Devices. Tunneling Devices. In *Reference Module in Materials Science and Materials Engineering*. Elsevier, 2016.

[73] P. Lafarge, H. Pothier, E. R. Williams, D. Esteve, C. Urbina, and M. H. Devoret. Direct observation of macroscopic charge quantization. *Zeitschrift für Physik B Condensed Matter*, 85(3):327–332, 1991.

[74] D. K. Ferry and S. M. Goodnick. *Transport in nanostructures.* Cambridge studies in semiconductor physics and microelectronic engineering: 6. Cambridge University Press, 1999.

[75] M. Tinkham. *Introduction to superconductivity.* International series in pure and applied physics. McGraw Hill, 1996.

[76] N. N. Bogoljubov. On a new method in the theory of superconductivity. *Il Nuovo Cimento (1955-1965)*, 7(6):794–805, 1958.

[77] J. G. Valatin. Comments on the theory of superconductivity. *Il Nuovo Cimento (1955-1965)*, 7(6):843–857, 1958.

[78] T. Aref, A. Averin, S. van Dijken, A. Ferring, M. Koberidze, V. F. Maisi, H. Q. Nguyend, R. M. Nieminen, J. P. Pekola, and L. D. Yao. Characterization of aluminum oxide tunnel barriers by combining transport measurements and transmission electron microscopy imaging. *Journal of Applied Physics*, 116(7):073702, 2014.

[79] R. A. Millikan. The Isolation of an Ion, a Precision Measurement of its Charge, and the Correction of Stokes's Law. *Phys. Rev. (Series I)*, 32:349–397, 1911.

[80] H. Grabert and M. H. Devoret. *Single charge tunneling : Coulomb blockade phenomena in nanostructures.* New York : Plenum in cooperation with NATO Scientific Affairs Division, 1992.

[81] A. Ranni, F. Brange, E. T. Mannila, C. Flindt, and V. F. Maisi. Real-time observation of cooper pair splitting showing strong non-local correlations. *Nature Communications*, 12(1):6358, 2021.

[82] F. W. J. Hekking, L. I. Glazman, K. A. Matveev, and R. I. Shekhter. Coulomb blockade of two-electron tunneling. *Phys. Rev. Lett.*, 70(26):4138–4141, 1993.

[83] G. E. Blonder, M. Tinkham, and T. M. Klapwijk. Transition from metallic to tunneling regimes in superconducting microconstrictions: Excess current, charge imbalance, and supercurrent conversion. *Phys. Rev. B*, 25(7):4515–4532, 1982.

[84] G. Deutscher. Crossed Andreev Reflections. *Journal of Superconductivity*, 15(1):43–47, 2002.

[85] M. J. M. de Jong and C. W. J. Beenakker. Andreev Reflection in Ferromagnet-Superconductor Junctions. *Phys. Rev. Lett.*, 74(9):1657–1660, 1995.

[86] R. J. Soulen, J. M. Byers, M. S. Osofsky, B. Nadgorny, T. Ambrose, S. F. Cheng, P. R. Broussard, C. T. Tanaka, J. Nowak, J. S. Moodera, A. Barry, and J. M. D. Coey. Measuring the Spin Polarization of a Metal with a Superconducting Point Contact. *Science*, 282(5386):85–88, 1998.

[87] I. I. Mazin, A. A. Golubov, and B. Nadgorny. Probing spin polarization with Andreev reflection: A theoretical basis. *Journal of Applied Physics*, 89(11):7576–7578, 2001.

[88] J. M. Byers and M. E. Flatté. Probing Spatial Correlations with Nanoscale Two-Contact Tunneling. *Phys. Rev. Lett.*, 74(2):306–309, 1995.

[89] D. V. Averin and Y. V. Nazarov. Virtual electron diffusion during quantum tunneling of the electric charge. *Phys. Rev. Lett.*, 65(19):2446–2449, 1990.

[90] S. L. Rudge and D. S. Kosov. Distribution of waiting times between electron cotunneling events. *Phys. Rev. B*, 98(24):245402, 2018.

[91] L. N. Cooper. Bound Electron Pairs in a Degenerate Fermi Gas. *Phys. Rev.*, 104(4):1189–1190, 1956.

[92] A. Einstein, B. Podolsky, and N. Rosen. Can Quantum-Mechanical Description of Physical Reality Be Considered Complete? *Phys. Rev.*, 47(10):777–780, 1935.

[93] R. Horodecki, P. Horodecki, M. Horodecki, and K. Horodecki. Quantum entanglement. *Rev. Mod. Phys.*, 81(2):865–942, 2009.

[94] J. S. Bell. On the Einstein Podolsky Rosen paradox. *Physics Physique Fizika*, 1(3):195–200, 1964.

[95] A. Aspect, P. Grangier, and G. Roger. Experimental Tests of Realistic Local Theories via Bell's Theorem. *Phys. Rev. Lett.*, 47(7):460–463, 1981.

[96] A. Aspect, J. Dalibard, and G. Roger. Experimental Test of Bell's Inequalities Using Time-Varying Analyzers. *Phys. Rev. Lett.*, 49(25):1804–1807, 1982.

[97] J. V. Koski, J. T. Peltonen, M. Meschke, and J. P. Pekola. Laterally proximized aluminum tunnel junctions. *Applied Physics Letters*, 98(20):203501, 2011.

[98] H. J. Carmichael, S. Singh, R. Vyas, and P. R. Rice. Photoelectron waiting times and atomic state reduction in resonance fluorescence. *Phys. Rev. A*, 39(3):1200–1218, 1989.

[99] D. M. Pozar. *Microwave engineering.* Addison-Wesley series in electrical and computer engineering. Addison-Wesley, 1990.

[100] M. Göppl, A. Fragner, M. Baur, R. Bianchetti, S. Filipp, J. M. Fink, P. J. Leek, G. Puebla, L. Steffen, and A. Wallraff. Coplanar waveguide resonators for circuit quantum electrodynamics. *Journal of Applied Physics*, 104(11):113904, 2008.

[101] B.D. Josephson. Possible new effects in superconductive tunnelling. *Physics Letters*, 1(7):251–253, 1962.

[102] V. Ambegaokar and A. Baratoff. Tunneling between superconductors. *Phys. Rev. Lett.*, 10:486–489, 1963.

[103] E. T. Mannila, V. F. Maisi, H. Q. Nguyen, C. M. Marcus, and J. P. Pekola. Detecting parity effect in a superconducting device in the presence of parity switches. *Phys. Rev. B*, 100:020502, 2019.

[104] T. A. Fulton and G. J. Dolan. Observation of single-electron charging effects in small tunnel junctions. *Phys. Rev. Lett.*, 59:109–112, 1987.

[105] W. G. van der Wiel, S. De Franceschi, J. M. Elzerman, T. Fujisawa, S. Tarucha, and L. P. Kouwenhoven. Electron transport through double quantum dots. *Rev. Mod. Phys.*, 75:1–22, 2002.

[106] Thomas Ihn. *Semiconductor nanostructures: Quantum states and electronic transport.* Oxford University Press, 2010.

[107] LP Kouwenhoven, CM Marcus, PL McEuen, S Tarucha, RM Westervelt, and NS Wingreen. Electron transport in quantum dots. In LP Kouwenhoven and GB Schon, editors, *NATO-ASI Workshop on Mesoscopic Electron Transport*, pages 105–214, 1997.

[108] M. Stepanova and S. Dew. *Nanofabrication. Techniques and Principles.* Springer, 2012.

[109] R. C. Jaeger. *Introduction to microelectronic fabrication.* Modular series on solid state devices (Upper Saddle River, N.J.) v. 5. Prentice Hall, Upper Saddle River, 2nd ed. edition, 2002.

[110] Z. Cui. *Nanofabrication. Principles, Capabilities and Limits.* Springer International Publishing, 2017.

[111] K. A. Dick, C. Thelander, L. Samuelson, and P. Caroff. Crystal phase engineering in single inas nanowires. *Nano Letters*, 10(9):3494–3499, 2010.

[112] Malin Nilsson, Luna Namazi, Sebastian Lehmann, Martin Leijnse, Kimberly A. Dick, and Claes Thelander. Single-electron transport in inas nanowire quantum dots formed by crystal phase engineering. *Phys. Rev. B*, 93:195422, 2016.

[113] D. Barker, S. Lehmann, L. Namazi, M. Nilsson, C. Thelander, K. A. Dick, and V. F. Maisi. Individually addressable double quantum dots formed with nanowire polytypes and identified by epitaxial markers. *Applied Physics Letters*, 114(18):183502, 2019.

[114] B. A. Mazin, P. K. Day, H. G. LeDuc, A. Vayonakis, and J. Zmuidzinas. Superconducting kinetic inductance photon detectors. In Howard A. MacEwen, editor, *Highly Innovative Space Telescope Concepts*, volume 4849, pages 283 – 293. International Society for Optics and Photonics, SPIE, 2002.

[115] H. Havir, S. Haldar, W. Khan, S. Lehmann, K. A. Dick, C. Thelander, P. Samuelsson, and V. F. Maisi. Quantum dot source-drain transport response at microwave frequencies, arxiv:2303.13048, 2023.

[116] Hans Joachim Eichler. *Lasers. Basics, Advances and Applications.* Springer Series in Optical Sciences: 220. Springer International Publishing, 2018.

[117] A. Einstein. Über einen die erzeugung und verwandlung des lichtes betreffenden heuristischen gesichtspunkt. *Annalen der Physik*, 322(6):132–148, 1905.

[118] E. Jang and H. Jang. Review: Quantum dot light-emitting diodes. *Chemical Reviews*, 123(8):4663–4692, 2023.

[119] L. Childress, A. S. Sørensen, and M. D. Lukin. Mesoscopic cavity quantum electrodynamics with quantum dots. *Phys. Rev. A*, 69:042302, 2004.

[120] C. X. Yu, S. Zihlmann, J. C. Abadillo-Uriel, V. P. Michal, N. Rambal, H. Niebojewski, T. Bedecarrats, M. Vinet, É. Dumur, M. Filippone, B. Bertrand, S. De Franceschi, Y.-M. Niquet, and R. Maurand. Strong coupling between a photon and a hole spin in silicon. *Nature Nanotechnology*, 18(7):741–746, 2023.

[121] A. Blais, A. L. Grimsmo, S. M. Girvin, and A. Wallraff. Circuit quantum electrodynamics. *Rev. Mod. Phys.*, 93:025005, 2021.

[122] R. Hanson, L. P. Kouwenhoven, J. R. Petta, S. Tarucha, and L. M. K. Vandersypen. Spins in few-electron quantum dots. *Rev. Mod. Phys.*, 79(4):1217–1265, 2007.

[123] F. A. Zwanenburg, A. S. Dzurak, A. Morello, M. Y. Simmons, L. C. L. Hollenberg, G. Klimeck, S. Rogge, S. N. Coppersmith, and M. A. Eriksson. Silicon quantum electronics. *Rev. Mod. Phys.*, 85(3):961–1019, 2013.

[124] A. Cottet, W. Belzig, and C. Bruder. Positive Cross Correlations in a Three-Terminal Quantum Dot with Ferromagnetic Contacts. *Phys. Rev. Lett.*, 92:206801, 2004.

[125] A. Cottet, W. Belzig, and C. Bruder. Positive cross-correlations due to dynamical channel blockade in a three-terminal quantum dot. *Phys. Rev. B*, 70:115315, 2004.

[126] R. J. Schoelkopf, P. Wahlgren, A. A. Kozhevnikov, P. Delsing, and D. E. Prober. The Radio-Frequency Single-Electron Transistor (RF-SET): A fast and ultrasensitive electrometer. *Science*, 280(5367):1238–1242, 1998.

[127] C. Bäuerle, D. C. Glattli, T. Meunier, F. Portier, P. Roche, P. Roulleau, S. Takada, and X. Waintal. Coherent control of single electrons: a review of current progress. *Rep. Prog. Phys.*, 81(5):056503, 2018.

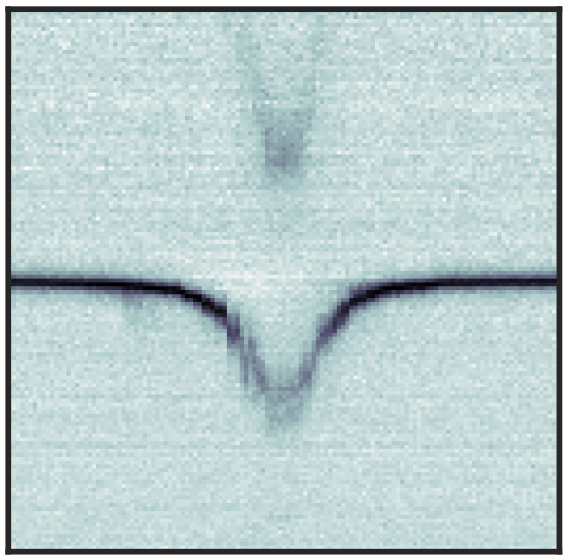

Printed by Media-Tryck, Lund 2023 NORDIC SWAN ECOLABEL 3041 0903

LUND UNIVERSITY

Faculty of Engineering
Department of Physics
Solid State Physics

ISBN 978-91-8039-871-8